Investigating Quasiparticle Interactions in the Far-Infrared

Dissertation

zur
Erlangung des Doktorgrades
der Naturwissenschaften
(Dr. rer. nat)

dem Fachbereich Physik
der Justus-Liebig-Universität Gießen

vorgelegt von

Daniel Anders

aus
Weilburg

Gießen, 2026

Vom Fachbereich 07 Mathematik und Informatik, Physik, Geographie der
Justus-Liebig-Universität Gießen als Dissertation angenommen am: 17.04.2026

Erstgutachter: Prof. Dr. Sangam Chatterjee
Zweitgutachter: Prof. Dr. Andreas Knorr

Tag der mündlichen Prüfung: 17.06.2026

„III/V-Proben sind wie ein guter Wein.“

— Dr. Christian Fuchs

Abstract

This dissertation investigates ultrafast charge-carrier dynamics and quasiparticle interactions in semiconductors using terahertz (THz) spectroscopy. The THz spectral range provides direct access to low-energy excitations such as intraexcitonic transitions and free-carrier dynamics, making it a powerful probe of many-body interactions in photoexcited semiconductor systems. Using optical pump—terahertz probe spectroscopy and broadband THz emission measurements, several aspects of carrier dynamics in bulk and low-dimensional semiconductors are explored. First, broadband and gapless THz radiation is generated in bulk germanium via phase-controlled quantum interference currents driven by two-color optical excitation. This approach enables efficient emission across the entire THz spectral range and provides insight into the underlying photocurrent generation mechanisms. The dissertation further investigates the formation dynamics of excitons in (Ga,In)As multi-quantum wells following nonresonant optical excitation. Time-resolved THz spectroscopy reveals that excitons emerge from an initially created electron–hole plasma on two distinct timescales: a fast component of approximately 10 ps and a slower component of about 250 ps. By introducing a differential probing method based on weak and strong THz fields, the longstanding discrepancy in reported exciton formation times is resolved. In addition, the interaction of incoherent excitons with an additional electron–hole plasma is studied using a double optical pump–THz probe scheme. The results show that elastic and inelastic scattering processes are governed primarily by the excess energy of the additional carriers rather than their density. Despite excitation energies exceeding the exciton binding energy, inelastic scattering occurs only when suitable final states are available, consistent with predictions from Fermi's golden rule. The screening of excitonic states by additional charge carriers is investigated by monitoring the transient shift of the intraexcitonic $1s$–$2p$ transition. The measurements provide direct access to the time-dependent exciton binding energy and reveal that the screening strength scales linearly with carrier density while the screening time is determined by the carrier excess energy. Finally, transient excitonic states induced by intense optical fields are demonstrated. Detuned optical excitation produces short-lived excitonic resonances that exist only during the temporal overlap of pump and probe pulses and manifest as blue-shifted THz absorption features. Together, these results provide new insight into ultrafast exciton formation, many-body interactions, and THz generation mechanisms in semiconductor systems, highlighting the capabilities of terahertz spectroscopy as a powerful tool for probing quasiparticle dynamics in condensed matter.

Zusammenfassung

Diese Dissertation untersucht die ultraschnelle Ladungsträgerdynamik und die Wechselwirkungen von Quasiteilchen in Halbleitern mittels Terahertz (THz)-Spektroskopie. Der THz-Spektralbereich ermöglicht den direkten Zugang zu Niedrigenergie-Anregungen wie intraexzitonischen Übergängen und der Dynamik freier Ladungsträger und ist damit ein leistungsfähiges Instrument zur Untersuchung von Vielteilchenwechselwirkungen in photoangeregten Halbleitersystemen. Mithilfe der optischen Anrege-Terahertz Abfrage Spektroskopie und breitbandiger THz-Emissionsmessungen werden verschiedene Aspekte der Ladungsträgerdynamik in Volumen- und niedrigdimensionalen Halbleitern untersucht. Zunächst wird in Germanium-Volumenmaterial breitbandige und lückenlose THz-Strahlung durch phasengesteuerte Quanteninterferenzströme erzeugt, die durch zweifarbige optische Anregung angetrieben werden. Dieser Ansatz ermöglicht eine effiziente Emission über den gesamten THz-Spektralbereich und liefert Einblicke in die zugrunde liegenden Mechanismen der Photostromerzeugung. Die Dissertation untersucht ferner die Bildungsdynamik von Exzitonen in (Ga,In)As-Mehrfachquantentöpfen nach nichtresonanter optischer Anregung. Zeitaufgelöste THz-Spektroskopie zeigt, dass Exzitonen aus einem anfänglich erzeugten Elektron-Loch-Plasma auf zwei unterschiedlichen Zeitskalen entstehen: einer schnellen Komponente von etwa 10 ps und einer langsameren Komponente von etwa 250 ps. Durch die Einführung einer Differential-Probing-Methode auf der Grundlage schwacher und starker THz-Felder wird die seit langem bestehende Diskrepanz bei den berichteten Exziton-Bildungszeiten aufgelöst. Darüber hinaus wird die Wechselwirkung inkohärenter Exzitonen mit einem zusätzlichen Elektron-Loch-Plasma unter Verwendung eines Schemas mit doppelter optischer Pumpe und THz-Sonde untersucht. Die Ergebnisse zeigen, dass elastische und inelastische Streuprozesse in erster Linie von der überschüssigen Energie der zusätzlichen Ladungsträger und nicht von deren Dichte bestimmt werden. Obwohl die Anregungsenergien die Bindungsenergie der Exzitonen übersteigen, tritt inelastische Streuung nur dann auf, wenn geeignete Endzustände verfügbar sind, was mit den Vorhersagen der goldenen Regel von Fermi übereinstimmt. Die Abschirmung von Exzitonzuständen durch zusätzliche Ladungsträger wird durch die Untersuchung der transienten Verschiebung des intraexzitonischen $1s$–$2p$-Übergangs untersucht. Die Messungen ermöglichen einen direkten Zugriff auf die zeitabhängige Exzitonenbindungsenergie und zeigen, dass die Abschirmungsstärke linear mit der Ladungsträgerdichte skaliert, während die Abschirmungszeit durch die überschüssige Energie der Ladungsträger bestimmt wird. Schließlich werden durch intensive optische Felder induzierte transiente Exzitonzustände demonstriert. Eine verstimmte optische Anregung erzeugt kurzle-

bige Exzitonresonanzen, die nur während der zeitlichen Überlappung von Anrege- und Abfragepulsen bestehen und sich als blauverschobene THz-Absorptionsmerkmale manifestieren. Zusammengenommen liefern diese Ergebnisse neue Einblicke in die ultraschnelle Exzitonbildung, Vielteilchenwechselwirkungen und THz-Erzeugungsmechanismen in Halbleitersystemen und unterstreichen die Eignung der Terahertz-Spektroskopie als leistungsstarkes Werkzeug zur Untersuchung der Quasiteilchendynamik in der kondensierten Materie.

Contents

List of Figures

List of Abbreviations

1D	one-dimensional
2D	two-dimensional
3D	three-dimensional
ABCD	air biased coherent detection
BBO	beta barium borate
BWO	backward wave oscillator
COM	center-of-mass
EOS	electro-optic sampling
EO	electro-optic
FWHM	full width at half maximum
FWM	four-wave mixing
GaAs	gallium arsenide
GaP	gallium phosphide
GaSe	gallium selenide
(Ga,In)As	gallium indium arsenide
Ge	germanium
He	helium
LT-GaAs	low-temperature gallium arsenide
LO-phonons	longitudinal optical phonons
MQW	multiple quantum wells
OPTP	optical pump-terahertz probe
OPOP	optical pump-optical probe
PL	photoluminescence
QW	quantum well
SCMOS	scientific complementary metal-oxide semiconductor

Si	silicon
TBP	time-bandwidth product
THz	terahertz
TDS	time-domain spectroscopy
TMDCs	transition metal dichalcogenides
TRPL	time-resolved photoluminescence
ZnTe	zinc telluride

1 Introduction

The interaction between light and matter is among the most fundamental phenomena in nature [1]. At the heart of modern condensed matter physics lies a conceptual achievement of extraordinary elegance: the quasiparticle. Rather than tracking the overwhelming complexity of interacting many-body systems particle by particle, the quasiparticle formalism [2] recasts collective excitations—phonons, polarons, magnons, and Coulomb-correlated electron–hole pairs—as effective single particles endowed with renormalized mass, charge, and lifetime [3]. This framework has proven not merely convenient but profoundly fruitful, underpinning the theoretical description of superconductivity [4], the fractional quantum Hall effect [5, 6], Bose–Einstein condensation, and an ever-growing catalogue of emergent quantum phases. Yet despite the power of this conceptual apparatus, many fundamental aspects of quasiparticle dynamics remain incompletely understood, particularly in the far-infrared spectral regime where the energy scales of quasiparticle interactions, lattice vibrations, and many-body correlations converge.

Among all quasiparticles in semiconductors, excitons occupy a uniquely central position. Formed through the Coulomb attraction between a conduction-band electron and a valence-band hole, the exciton is a charge-neutral composite particle whose binding energy and spatial extent are governed by the dielectric environment and the effective masses of its constituents [7]. In the Wannier–Mott limit, realized in high-quality inorganic semiconductor nanostructures [8], excitons are weakly bound, spatially delocalized entities that dominate the optical response near the band edge [9]. Their stability, formation dynamics, and interactions with other quasiparticles directly determine the efficiency of photovoltaic devices, the coherence properties of excitonic lasers, the dynamics of optical switches, and the quantum nature of light emitters [10]. The exciton is, in short, both a model system for quantum many-body physics and a performance-critical element of contemporary optoelectronics.

Understanding how excitons form, scatter, and respond to external fields requires experimental access to their internal degrees of freedom—the transitions between excitonic energy levels that reflect their Coulomb character directly. This access is uniquely provided by terahertz (THz) spectroscopy [11]. Because the energy spacing between the hydrogenic eigenstates of Wannier–Mott excitons lies squarely in the THz spectral range (1–10 THz, corresponding to 4–40 meV) [12, 13], THz radiation can directly probe intraexcitonic transitions—most prominently the $1s$–$2p$ resonance—and thereby probe the exciton population irrespective of its center-of-mass momentum [11, 14]. This capability distinguishes THz spectroscopy fundamentally from conventional optical techniques: while photoluminescence and four-wave mixing measure quantities tied to the coherent polarization or the radiative recombination of the entire carrier ensemble [15], THz probing provides a direct, quantitative measure of the bound exciton population [11, 16]. The distinction is not merely technical—it has profound consequences for resolving longstanding controversies in the literature concerning exciton formation timescales and scattering behavior [11, 17, 18].

The terahertz spectral range presents, however, its own formidable challenges. For decades, the so-called "THz gap" impeded experimental progress: lying between the domains of conventional microwave electronics and infrared optics [19, 20], the THz

regime was notoriously difficult to access with sufficient bandwidth, coherence, and field strength [20, 21]. While substantial advances in THz source technology over the past three decades—including photoconductive antennas, optical rectification in nonlinear crystals, spintronic emitters [22], and air-plasma sources [23]—have dramatically narrowed this gap, important limitations persist [24–27]. In particular, the phonon absorption of polar semiconductors creates opaque windows in the 4–12 THz range that obstruct measurements precisely where many excitonic features reside [20]. The development of gapless, broadband THz sources that circumvent these phonon resonances thus remains an active and strategically important research frontier.

The present dissertation addresses this confluence of challenges through a coherent experimental program that advances both the generation and the application of THz radiation in the study of quasiparticle interactions. Three interconnected investigations are reported, each representing a significant contribution at the intersection of ultrafast spectroscopy, semiconductor physics, and many-body theory.

The first study demonstrates broadband, gapless THz generation via quantum interference currents in bulk germanium. By simultaneously driving one-photon and two-photon interband transitions through a two-color optical excitation scheme [28, 29]—combining a femtosecond pulse at 1590 nm with its second harmonic at 795 nm—a polar asymmetry in the photoexcited carrier distribution is induced, giving rise to a directional charge current whose temporal acceleration emits THz radiation. Germanium, a non-polar group-IV semiconductor, is free of the infrared-active phonon modes that restrict conventional polar emitters, enabling a spectrally continuous bandwidth approaching 8 THz [30]. The emitted pulses display a pronounced temporal asymmetry with a peak ratio of 3.34:1 and a temporal duration of 110 fs at full width at half maximum—properties that render the source particularly attractive for THz-driven scanning tunneling microscopy and other near-field applications [31]. Critically, the excitation scheme operates efficiently with low-power fiber-laser systems, opening a pathway toward compact, accessible THz sources that do not require costly chirped-pulse amplifier technology.

The second and third investigations exploit the unique sensitivity of optical pump–terahertz probe (OPTP) spectroscopy [32] to resolve two fundamental problems in semiconductor many-body physics: the dynamics of exciton formation and the nature of exciton–electron scattering. The former has been a subject of enduring controversy. Prior studies employing time-resolved photoluminescence (TRPL) [17, 18] and OPTP spectroscopy reported widely discrepant formation timescales, with values ranging from a few picoseconds to several hundreds of picoseconds depending on excitation density and detection method. The present work resolves this inconsistency by demonstrating that TRPL signals track the dynamics of the electron–hole plasma rather than the excitonic population directly, because radiative recombination of unbound carrier pairs dominates the luminescence yield in the relevant time window [15]. THz spectroscopy, by contrast, is sensitive exclusively to bound states [14]. To overcome the intrinsic limitation of conventional OPTP analysis at elevated carrier densities [33]—where spectral broadening of the intraexcitonic resonance renders the Drude–Lorentz decomposition ambiguous—a differential spectroscopic method is introduced in which intense THz pulses are employed to selectively ionize the exciton population. Subtracting the resulting pure plasma response from the total signal isolates the excitonic contribution with high fidelity. Using this approach, exciton formation is found to proceed on two distinct timescales: a rapid component near 10 ps, attributed to geminate pair recombination in which the initial Coulomb correlation between photoexcited electron–hole pairs is preserved, and a slower component near 250 ps, consistent with acoustic-phonon-assisted formation from an uncorrelated plasma. Importantly, these timescales are found to be largely independent of

excitation density within an intermediate density regime, resolving a further inconsistency in the prior literature.

The third investigation probes the coexistence regime of excitons and electron–hole plasma by introducing a second optical pump pulse to independently control the plasma density and its excess energy. The degree to which an electron–hole plasma can destroy an existing exciton population depends sensitively on whether scattering events are elastic—redistributing momentum while conserving binding energy—or inelastic—transferring sufficient energy to ionize the exciton [34]. By tracking both the linewidth of the intraexcitonic $1s$–$2p$ transition (a measure of total scattering) [35] and the oscillator strength of that transition (a measure of the exciton population), the elastic and inelastic contributions to exciton–electron scattering are disentangled with quantitative precision. A remarkable result emerges: for plasma excess energies only slightly above the exciton binding energy, inelastic scattering is strongly suppressed despite the availability of sufficient energy for ionization. This inhibition is traced to phase-space restrictions arising from Fermi's Golden Rule [36]—the density of final states for the unbound carriers following ionization is insufficient to support efficient energy transfer. The interaction strength between excitons and the electron–hole plasma, quantified by the total scattering cross section, is found to be independent of plasma excess energy, implying that the partitioning between elastic and inelastic channels is governed entirely by phase-space geometry rather than by the interaction potential itself.

Taken in concert, these investigations demonstrate the exceptional versatility of THz spectroscopy as a probe of quasiparticle dynamics. At the same time, the work delineates both the capabilities and the intrinsic limitations of the technique. The theoretical framework employed throughout is rooted in the semiconductor Bloch equations (SBEs) [37] and their solution in the Drude–Lorentz approximation [3], which provides a microscopically motivated description of the THz conductivity in terms of free-carrier (Drude) and bound-exciton (Lorentz) contributions [14]. Where the SBE formalism approaches its limits—as in the high-density broadening of excitonic resonances—novel experimental strategies are developed to extend the accessible parameter space.

The structure of this dissertation reflects the logical progression from theoretical foundations to experimental methods to results. Chapter 2 establishes the microscopic theoretical framework, beginning with the semiconductor Bloch equations and proceeding through the exciton Wannier equation, the THz Elliott formula, and the Drude–Lorentz model for the THz conductivity. Chapter 3 describes the experimental methodology, with particular attention to THz generation, electro-optic detection, and the design and calibration of the optical pump–THz probe setup. Chapters 4 and 5 present the results of all three experimental investigations in turn, followed by a summary and outlook in Chapter 6. The three peer-reviewed publications that form the scientific core of this thesis are reproduced in Chapter 7.

The work reported here contributes to a broader research program aimed at establishing THz spectroscopy as a quantitative, information-rich tool for condensed matter physics—one capable of probing not merely the static properties of quantum materials but the ultrafast, far-from-equilibrium dynamics that govern their function. As semiconductor technologies continue to miniaturize toward quantum confinement regimes, and as quantum information science places ever-greater demands on the coherent control of quantum states in solid-state systems, the ability to monitor and manipulate quasiparticle interactions with femtosecond temporal resolution and meV spectral precision becomes increasingly indispensable. The present dissertation takes steps toward that goal, while opening new experimental and conceptual pathways for the investigations that must follow.

2 Light-matter interaction in semiconductors

This chapter establishes the theoretical framework for analysing the data presented in this thesis. It focuses on the fundamental principles of light–matter interaction in semiconductors, with particular emphasis on near-infrared optical excitation, which generates the carrier populations and excitonic states of interest, and terahertz probing, which forms the experimental basis of the measurements presented here. As light–matter interaction underlies all spectroscopic techniques, it is central to the analysis developed here. The following sections outline the key concepts required for this study without aiming for completeness; for more comprehensive treatments, the reader is referred to the established literature [3, 16, 38, 39].

2.1 Semiconductor Bloch equations

The basis for theoretical descriptions of light–matter action in semiconductors is formed by the semiconductor Bloch equations. SBEs are designated as such due to their structural analogy to the optical Bloch equations, which describe the excitation dynamics of a two-level atomic system interacting with a classical electromagnetic field. More precisely, within the Hartree–Fock approximation—i.e., when all genuine two-particle correlations and Coulomb interactions are neglected—the SBE reduce exactly to the optical Bloch equations in the limit of a single crystal-momentum state $\mathbf{k}$, making the structural analogy between the two frameworks mathematically precise. In contrast to the atomic case, the SBEs must also account for the many-body interactions arising from Coulomb interactions among charge-carriers, as well as the coupling between lattice vibrations (phonons) and electrons. This derivation of the SBEs is based on a simplified description of the electronic band structure, often referred to as the two-band approximation [38]. For simplicity, this model assumes that the excitation laser pulse drives interband transitions in the vicinity of the band-gap energy, so that carrier populations are generated within a narrow range of crystal momenta $\mathbf{k}$ near the band edge. Consequently, only the relevant valence and conduction bands need to be considered. This is well justified when exciting with a finite-bandwidth pulse not far from the fundamental band gap, since the excited $\mathbf{k}$-states are densely spaced and collectively contribute to the optical response. In the formalism of second quantization, the total Hamiltonian of the system can be written as [3]

$$H_{\mathrm{System}} = H_{\mathrm{el}} + H_{\mathrm{I}}, \tag{2.1}$$

where H_{el} represents the electronic subsystem consisting of conduction-band electrons and valence-band holes. This term includes not only the kinetic single-particle energies but also the attractive and repulsive Coulomb interactions between these quasiparticles. The interaction Hamiltonian H_{I} describes the coupling of the semiconductor to the external electric field $E(t)$, which drives dipole-allowed interband transitions between the valence and conduction bands, thereby injecting electrons and holes in the respective states. The total Hamiltonian thus accounts for free-carrier dynamics, Coulomb interac-

tions among electrons and holes, and the coupling to the incident optical field. Together with the Heisenberg equation of motion,

$$i\hbar\frac{d}{dt}O(t) = [O(t), H_{\text{System}}], \tag{2.2}$$

the time evolution of the relevant microscopic quantities such as the interband transitions P_k can be obtained [40]. These include the microscopic interband polarization $P_k(t)$, as well as the electron and hole occupation probabilities $n_{e,k}(t)$ and $n_{h,k}(t)$, which are defined by their quantum-mechanical expectation values:

$$n_{e,k}(t) = \langle a^\dagger_{c,k} a_{c,k}\rangle, \tag{2.3}$$

$$n_{h,k}(t) = 1 - \langle a^\dagger_{v,k} a_{v,k}\rangle, \tag{2.4}$$

$$P_k(t) = \langle a^\dagger_{v,k} a_{c,k}\rangle. \tag{2.5}$$

Here, $a^{(\dagger)}_\lambda$ denotes the annihilation (creation) operator in band $\lambda = v, c$, where v and c refer to the valence and conduction bands, respectively. Evaluating the commutators in Equation 2.2 yields a coupled set of nonlinear differential equations known as the semiconductor Bloch equations, which can be regarded as a generalization of the optical Bloch equations:

$$\frac{\partial P_k}{\partial t} = -i(\varepsilon_{e,k} + \varepsilon_{h,k})P_k + i(1 - n_{e,k} - n_{h,k})\,\omega_{R,k} + \left.\frac{\partial P_k}{\partial t}\right|_{\text{scatt}}, \tag{2.6}$$

$$\frac{\partial n_{e,k}}{\partial t} = -2\,\text{Im}(\omega_{R,k} P^*_k) + \left.\frac{\partial n_{e,k}}{\partial t}\right|_{\text{scatt}}, \tag{2.7}$$

$$\frac{\partial n_{h,k}}{\partial t} = -2\,\text{Im}(\omega_{R,k} P^*_k) + \left.\frac{\partial n_{h,k}}{\partial t}\right|_{\text{scatt}}. \tag{2.8}$$

These equations describe the coupled evolution of the optical polarization and carrier populations (electrons and holes) near the semiconductor band edge. The quantities $\varepsilon_{e,k}$ and $\varepsilon_{h,k}$ represent the renormalized single-particle energies of electrons and holes (including Hartree–Fock Coulomb shifts), and P^*_k is the complex conjugate of the microscopic polarization. The generalized Rabi frequency

$$\omega_{R,k} = \frac{d_{cv}}{\hbar}\,E(t) + \frac{1}{\hbar}\sum_{k'} V_{k-k'}\,P_{k'} \tag{2.9}$$

couples the optical driving field $E(t)$ to the polarization through the interband dipole matrix element d_{cv}, and additionally incorporates the Coulomb-induced many-body renormalization of the optical field via the Hartree–Fock exchange sum $\sum_{k'} V_{k-k'} P_{k'}$, where $V_{k-k'}$ is the Fourier transform of the Coulomb potential. This Coulomb-renormalization term is the key feature that distinguishes the SBEs from the optical Bloch equations of an isolated two-level system: even in the absence of scattering, the collective Coulomb interaction among all k-modes modifies the effective driving field experienced by each individual k-state. The term $(1 - n_{e,k} - n_{h,k})$ corresponds to the phase-space filling effect, while the expression $-2\,\text{Im}(\omega_{R,k} P^*_k)$ describes carrier generation via optical absorption. The scattering contributions, indicated by the subscript "scatt", incorporate many-body effects such as Coulomb interactions and carrier–phonon coupling (two-particle correlations beyond the Hartree–Fock level). These terms account for phenomena including excitation-induced dephasing, carrier-carrier and carrier–phonon scattering, band-gap

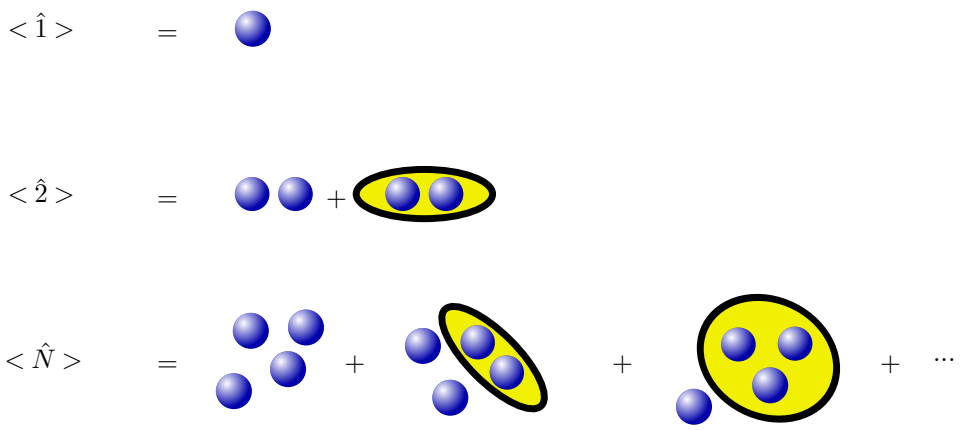

Figure 2.1: Schematic of the hierarchy problem in SBEs and the cluster-expansion approach. The topmost row depicts the singlet contribution, the middle row shows how the doublets are decomposed into their singlet contributions and the correlated part, and the bottom row shows, how this translates to the n-particle solution. Higher order terms are typically treated in a scattering approximation.

renormalization, screening of the Coulomb interaction (e–e, h–h, e–h), excitonic effects, biexciton formation, and carrier-density relaxation [3, 16]. Two of these scattering contributions are particularly noteworthy for the present work: first, the scattering between excitons and a free electron–hole plasma, which is investigated experimentally in Section 5.2; and second, the screening of the Coulomb interaction by a free carrier plasma, which is the subject of Section 5.3. Due to the presence of Coulomb and carrier-phonon interactions, the equations of motion for the single-particle observables do not form a closed set. Instead, their dynamics is coupled to higher-order many-body expectation values, resulting in an infinite hierarchy of coupled equations, commonly referred to as the hierarchy problem. To obtain a tractable description, this hierarchy must be truncated by introducing suitable approximations. To obtain a tractable description, the hierarchy must be truncated at a finite order. A widely used and physically transparent approach is the cluster expansion method [41, 42], in which expectation values are systematically decomposed into uncorrelated (single-particle) contributions and genuine many-body correlations, as shown in Figure 2.1. Within this framework, the scattering contributions indicated by the subscript "scatt" arise from the systematic treatment of the next-higher order beyond the mean field: the two-particle (doublet) correlations are evaluated in a Markovian scattering approximation, yielding phonon- and Coulomb-induced scattering rates in closed form. All genuine three-particle and higher-order correlations are then neglected, an approximation justified under the excitation conditions considered here, where such higher-order clusters play a subdominant role. It is important to emphasize that this procedure does not simply discard higher-order terms—rather, it captures their leading-order influence through the scattering integrals appearing in Equations (2.6) to (2.8). Alternative approaches to truncate the hierarchy include, for example, the Hartree–Fock approximation, which neglects correlation effects beyond mean-field interactions, quantum kinetic approaches based on nonequilibrium Green's functions, or density-matrix renormalization schemes. While these methods differ in their level of approximation and computational complexity, the cluster expansion is better suited to calculate mixed interactions, e.g., mixed optical and Coulomb interactions, while Green's function methods are better suited to capture higher correlation orders without any mixing.

2.2 Excitons

In semiconductors, the Coulomb attraction between negatively charged electrons and positively charged holes can lead to the formation of correlated electron–hole pairs known as excitons. Because excitons consist of an electron and a hole bound together by their mutual electrostatic interaction, they are charge-neutral quasiparticles that represent one of the most fundamental excitations in a semiconductor system. The concept of excitons was first introduced theoretically in the 1930s by Frenkel, Peierls, and Wannier [7, 43]. Depending on the spatial extent and binding energy of the electron–hole pair, two main categories are distinguished: Frenkel excitons and Wannier–Mott excitons [44]. Figure 2.2 illustrates the spatial character of Frenkel and Wannier–Mott excitons as well as the resulting excitonic dispersion with hydrogen-like bound states. Frenkel excitons are typically found in organic or molecular crystals, where the strong Coulomb attraction keeps the electron and hole localized on the same or neighboring atoms. In contrast, Wannier-Mott excitons occur in inorganic semiconductors, where the dielectric screening is strong and the effective carrier masses are small, resulting in weakly bound and spatially extended states. The present section focuses on the latter case. In inorganic semiconductors, the properties of correlated electron–hole pairs can be described by the generalized Wannier equation. Assuming a quasi-equilibrium condition in which carrier scattering has driven the system into a thermal Fermi-Dirac distribution, the two-particle correlation terms in the SBE vanish, and the problem reduces to a homogeneous eigenvalue equation. For an unexcited semiconductor, i.e., $n_{e,k} = n_{h,k} = 0$, this eigenvalue problem becomes mathematically equivalent to the Schrödinger equation of the hydrogen atom when the effective masses of the electron (m_e^*) and hole (m_h^*), as well as the dielectric constant ε_r of the host material, are taken into account. The resulting Wannier equation in real space reads

$$\left[-\frac{\hbar^2\nabla_r^2}{2m_r} + V(r)\right]\Psi_\lambda(r) = E_\lambda\Psi_\lambda(r), \tag{2.10}$$

where the reduced exciton mass m_r is defined through

$$\frac{1}{m_r} = \frac{1}{m_e^*} + \frac{1}{m_h^*}. \tag{2.11}$$

The potential $V(r)$ represents the attractive Coulomb interaction between the oppositely charged quasiparticles. The eigenvalues E_λ describe the binding energies of the bound excitonic states, while $\Psi_\lambda(r)$ denotes the corresponding excitonic wavefunctions. Solving Eq. (2.10) yields a discrete series of bound states analogous to the hydrogenic levels ($1s$, $2s$, $3s$, ...), with binding energies given by

$$E_n = R^*\frac{1}{n^2} \quad \text{in 3D}, \tag{2.12}$$

$$E_n = R^*\frac{1}{(n-\frac{1}{2})^2} \quad \text{in 2D}, \quad n = 1, 2, \ldots \tag{2.13}$$

where R^* is the exciton Rydberg energy defined as

$$R^* = \frac{m_r}{m_e}\frac{13.6\,\text{eV}}{\varepsilon_r^2}. \tag{2.14}$$

In analogy to the hydrogen atom, the binding energy decreases with increasing principal

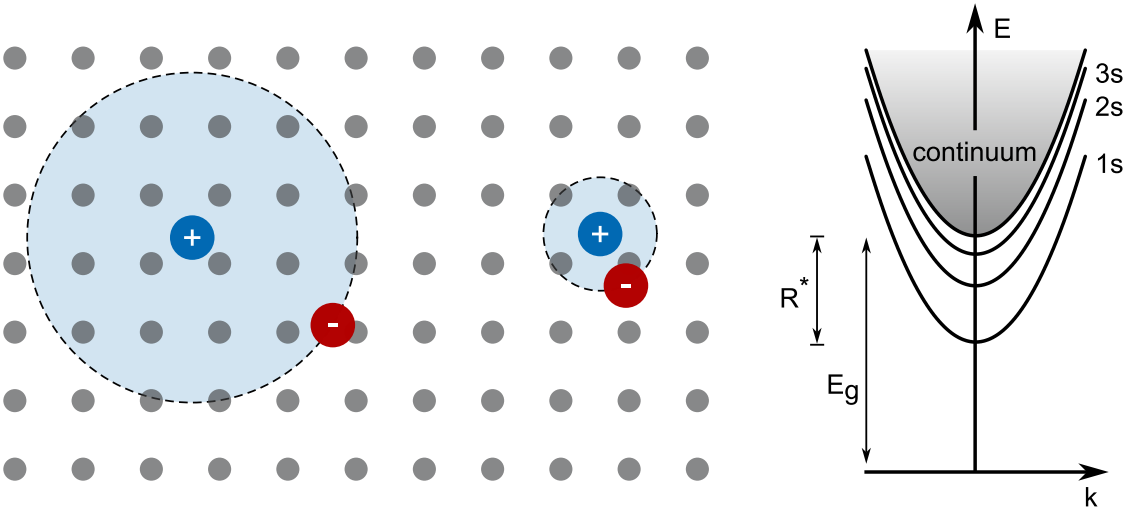

Figure 2.2: Spatial character and dispersion of excitons in semiconductors.
Left panel: Schematic comparison of Wannier-Mott and Frenkel excitons in real space. A Wannier-Mott exciton (left) consists of a positively charged hole (blue, +) at the center and a negatively charged electron (red, −) with a delocalized probability distribution, bound by Coulomb attraction. The spatial extent (dashed circle) is much larger than the lattice constant of the semiconductor crystal (gray spheres). A Frenkel exciton (right) exhibits strong localization with electron and hole confined to the same or neighboring lattice sites due to weak dielectric screening.
Right panel: Excitonic dispersion relation $E(k)$ showing the hydrogen-like Rydberg series of bound states $(1s, 2s, 3s)$ below the band-gap energy E_g. The binding energy of the ground state is given by the effective Rydberg constant R^*. The continuum region (gray shading) represents unbound electron–hole pairs. Each parabolic branch corresponds to the center-of-mass motion of the exciton as a composite quasiparticle.

quantum number n and approaches zero for large n, marking the transition from bound states to the unbound electron–hole continuum at the band-gap energy E_g. This is illustrated in the right panel of Figure 2.2. The magnitude of the exciton binding energy and the spatial extent of the excitonic wavefunction strongly depend on the dielectric screening and effective masses of the host material. The exciton Bohr radius

$$a_{\text{exc}} = \frac{\varepsilon_r \hbar^2}{m_r e^2} \tag{2.15}$$

is typically much larger than the lattice constant of the semiconductor crystal. In materials such as GaAs, where $\varepsilon_r \approx 13$, the large dielectric constant effectively screens the Coulomb attraction. In combination with effective masses much smaller than the electron mass, this leads to small binding energies on the order of a few meV (e.g., $E_B = 4.2$ meV for bulk GaAs) and large exciton radii that extend over several unit cells. Such weakly bound, delocalized excitons are commonly referred to as Wannier–Mott excitons. In contrast, Frenkel excitons exhibit significantly larger binding energies—often by several orders of magnitude—because of the much smaller dielectric screening in organic materials. As a result, electron and hole remain localized within the same molecule, with separations of only a few nanometers. The binding energy of excitons depends sensitively on

the dimensionality of the system. As indicated by Eq. (2.13), the ideal two-dimensional case exhibits a binding energy that is four times larger than in the three-dimensional bulk. In quantum wells or thin semiconductor films, this enhancement arises from spatial confinement of the carriers and a reduced dielectric screening, particularly when the surrounding material has a smaller dielectric constant. The reduced screening strengthens the Coulomb attraction and therefore increases the binding energy while decreasing the exciton Bohr radius perpendicular to the plane of the quantum film. Consequently, for the ground state ($n = 1$), the exciton radius in a two-dimensional system can be approximately half that of the corresponding three-dimensional case. In an optically excited semiconductor, the presence of free carriers alters the Coulomb interaction through the phase-space filling factor $(1 - n_{e,k} - n_{h,k})$ in the SBEs. As the carrier density increases, Pauli-blocking effects reduce the effective Coulomb attraction between electrons and holes. Beyond a critical carrier concentration, this interaction becomes effectively repulsive, and bound excitonic states can no longer exist. The transition from a regime of bound excitons to an unbound electron–hole plasma is known as the Mott transition [45]. This density-dependent transition plays a central role in the nonlinear optical response of semiconductors and defines the boundary between exciton and plasma-like regimes in many-body systems. Beyond single excitons, Coulomb correlations in semiconductors can also give rise to more complex composite quasiparticles, such as biexcitons (bound states of two excitons) [46], trions (charged excitons) [47], dropletons [48], and electron–hole droplets [49]. These higher-order correlated states emerge under specific excitation conditions and contribute to the rich many-body dynamics observed in modern semiconductor optics.

2.3 Terahertz response of semiconductors and conductivity

At this point, a brief overview is given of the microscopic theory that forms the basis for describing the terahertz absorption of electron–hole plasmas and excitons. Comprehensive treatments of absorption dynamics in the THz frequency range can be found in [38, 50, 51]. In general, THz absorption is primarily governed by electron–hole pair correlations [16]. A brief clarification regarding the scope of the theoretical framework is in order. The SBEs presented in Equations (2.6) to (2.8) describe the interband dynamics of the semiconductor driven by a near-infrared optical field. To describe the THz response of the system—including both intraexcitonic absorption and the Drude response of free carriers—these equations must be supplemented with intraband contributions. In particular, a THz electric field $\mathbf{E}_{\mathrm{THz}}(t)$ couples to the intraband motion of carriers and gives rise to additional driving terms of the form $e\,\mathbf{E}_{\mathrm{THz}} \cdot \nabla_{\mathbf{k}}\, n_{\mathbf{k}}$ in the equations of motion for the carrier densities. These $\mathbf{k}$-gradient terms describe the field-induced acceleration of carriers in momentum space and are responsible for both the intraexcitonic transitions and the free-carrier Drude response. A comprehensive microscopic derivation including the full intraband contributions can be found in [16]. The THz Elliott equation, which is derived from the extended SBEs including these intraband terms, provides a microscopic framework for describing the excitonic contribution to THz radiation absorption:

$$\alpha_{\mathrm{THz}}(\omega) = \mathrm{Im}\left[\sum_{\nu,\lambda} \frac{S_{\nu,\lambda}(\omega)\,\Delta N_{\nu,\lambda} - [S_{\nu,\lambda}(-\omega)\,\Delta N_{\nu,\lambda}]^*}{\omega\,(\hbar\omega + i\gamma(\omega))}\right]. \tag{2.16}$$

The quantities $\Delta N_{\nu,\lambda}$ constitute the excitonic population matrix in the basis of excitonic eigenstates. In direct analogy to the carrier occupations $n_{e,\mathbf{k}}$ and $n_{h,\mathbf{k}}$ introduced in

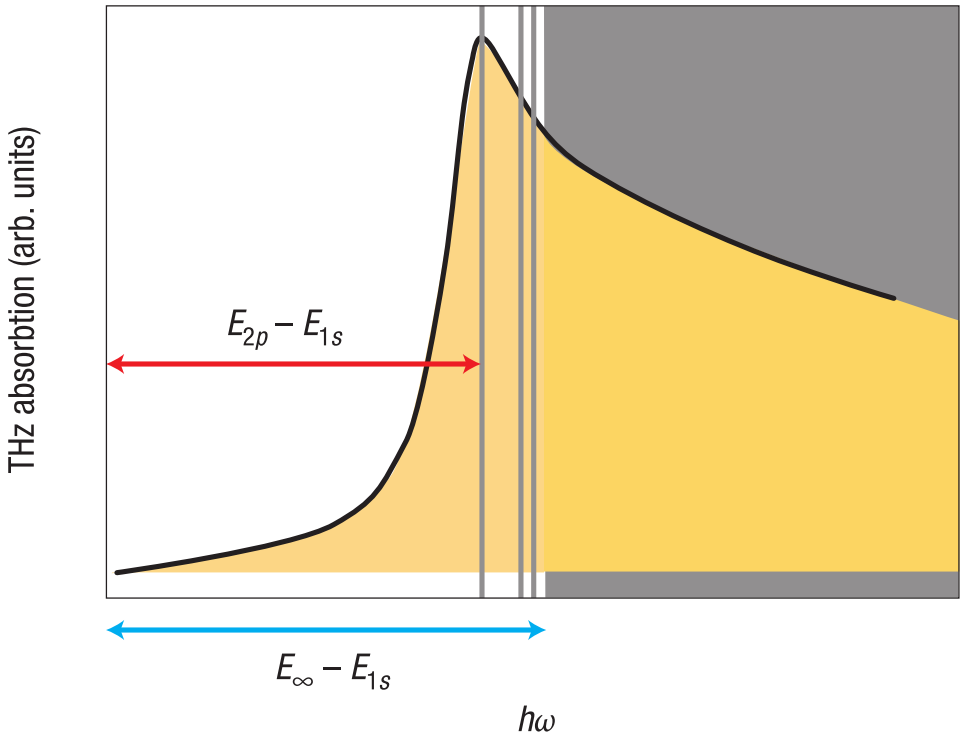

Figure 2.3: Calculated THz absorption using the Elliott-formula from Ref. [50]. The spectrum shown was calculated for a finite exciton population in a GaAs sample. The vertical lines denote the spectral positions of the $1s$–$2p$, $1s$–$3p$, and $1s$–$4p$ transitions. Here, the $1s$–$2p$ transition dominates the spectrum. The $1s$–$3p$ transition is not resolved anymore due to linewidth broadening and merging with higher transitions. The gray shaded area corresponds to the continuum transitions.

Eqs. (2.3) and (2.4) for single-particle states, the diagonal elements $\Delta N_{\lambda,\lambda} \equiv \Delta n_\lambda$ represent the population of excitonic state λ, i.e., the number of excitons occupying that eigenstate [41]. The off-diagonal elements $\Delta N_{\nu,\lambda}$ for $\nu \neq \lambda$ describe quantum-mechanical coherences—transition amplitudes—between different excitonic states ν and λ, which are generated by the optical pump pulse and contribute to the coherent part of the THz response. Unlike in optical spectroscopy, where typically only a few resonant transitions dominate, THz spectroscopy of excitons involves contributions from a continuum of excitonic states. This becomes evident in the spectral response function:

$$S_{\nu,\lambda}(\omega) = \sum_\beta \frac{(E_\beta - E_\nu)\, J_{\nu\beta}\, J_{\beta\lambda}}{E_\beta - E_\nu - \hbar\omega - i\gamma_{\lambda,\nu}(\omega)}. \tag{2.17}$$

Here, $J_{\nu\beta} \propto \sum_{\mathbf{k}} \phi^*_\nu(\mathbf{k})\,(\mathbf{k}\cdot\mathbf{k}_{\mathrm{THz}})\,\phi_\beta(\mathbf{k})$ denotes the current matrix element between the excitonic states ν and β. The unit vector $\mathbf{k}_{\mathrm{THz}}$ defines the propagation direction of the incident THz field. Analogous to atomic selection rules in optical spectroscopy, transition probabilities are governed by angular momentum conservation and symmetry constraints. Each transition allowed by these rules gives rise to a resonance in the spectral response function $S_{\nu,\lambda}(\omega)$, whose linewidth is determined by the dephasing rate $\gamma_{\lambda,\nu}(\omega)$. Additionally, the decay of macroscopic THz currents is characterized by the damping term $\gamma(\omega)$. An important distinction between THz and optical spectroscopy lies in the role of the ex-

citon center-of-mass (COM) momentum $\mathbf{Q}$. In optical spectroscopy, photon momentum conservation restricts interband transitions to excitons with $\mathbf{Q} \approx 0$, since optical photons carry negligible crystal momentum. By contrast, THz photons drive intraexcitonic transitions between internal states of the same exciton, which are allowed for excitons at all COM momenta $\mathbf{Q}$. The full THz absorption therefore involves contributions from the entire distribution of exciton COM momenta, and the excitonic population matrix element in Equation (2.16) must more completely be written as

$$\Delta N_{\nu,\lambda} = \sum_{\mathbf{Q}} \Delta N_{\nu,\lambda}(\mathbf{Q}), \tag{2.18}$$

where the sum runs over all occupied $\mathbf{Q}$ states. This makes THz spectroscopy a particularly direct probe of the total exciton density, irrespective of the momentum distribution of the excitonic population. A key advantage of THz spectroscopy lies in its ability to directly identify exciton populations through intraexcitonic transitions. In solid-state systems, however, these spectral lines are significantly broadened due to strong dephasing, scattering processes, and disorder in the sample. Consequently, in most experimental situations, only the fundamental $1s$—$2p$ transition can be clearly resolved, whereas higher-order intraexcitonic transitions overlap and merge into a continuous spectral feature. This is shown exemplarily in Figure 2.3. It illustrates the asymmetry of the THz absorption towards higher energies due to the closer spacing of transitions from $1s$ to higher p-states.

Drude model for free carriers

The Drude model describes the response of unbound charge-carriers, i.e., an electron–hole plasma to an applied oscillating electric field. Electrons are treated as classical particles with an effective mass m^* that undergo collisions characterized by an average momentum-relaxation time τ (or damping rate $\gamma_D = 1/\tau$). The model neglects band-structure details except through m^* and assumes linear response to a weak field. Consider an electron (charge $-e$) subject to an electric field $\mathbf{E}(t) = \mathbf{E}_0 e^{-i\omega t}$. In the Drude approximation the single-particle equation of motion with a phenomenological damping term is

$$m^*\ddot{\mathbf{x}}(t) + m^*\gamma_D\dot{\mathbf{x}}(t) = -e\mathbf{E}(t). \tag{2.19}$$

Assuming a time-harmonic response $\mathbf{x}(t) = \mathbf{x}(\omega)e^{-i\omega t}$ gives $\dot{\mathbf{x}} = -i\omega\mathbf{x}$ and $\ddot{\mathbf{x}} = -\omega^2\mathbf{x}$. Substituting into (2.19) leads to

$$\left(-m^*\omega^2 - im^*\gamma_D\omega\right)\mathbf{x}(\omega) = -e\mathbf{E}(\omega). \tag{2.20}$$

Solving for $\mathbf{x}(\omega)$ results in

$$\mathbf{x}(\omega) = \frac{e}{m^*}\frac{1}{\omega^2 + i\gamma_D\omega}\mathbf{E}(\omega). \tag{2.21}$$

With the charge-carrier velocity $\mathbf{v} = -i\omega\mathbf{x}$ and a carrier density n the current density can be expressed as $\mathbf{J} = -ne\mathbf{v}$. Inserting Equation (2.21) results in

$$\mathbf{J}(\omega) = -ne(-i\omega)\mathbf{x}(\omega) = ne^2\frac{i\omega}{m^*}\frac{1}{\omega^2 + i\gamma_D\omega}\mathbf{E}(\omega). \tag{2.22}$$

By using the linear-response relation $\mathbf{J}(\omega) = \sigma(\omega)\mathbf{E}(\omega)$, one can identify the complex conductivity as

$$\sigma(\omega) = \frac{ne^2}{m^*} \frac{i\omega}{\omega^2 + i\gamma_D \omega}. \tag{2.23}$$

It is conventional to rewrite (2.23) in forms that highlight the low-frequency limit:

$$\sigma(\omega) = \frac{ne^2}{m^*} \frac{1}{\gamma_D - i\omega} = \frac{\varepsilon_0 \omega_p^2}{\gamma_D - i\omega}, \tag{2.24}$$

where the plasma frequency is introduced by

$$\omega_p^2 \equiv \frac{ne^2}{\varepsilon_0 m^*}. \tag{2.25}$$

The current $\mathbf{J}$ modifies the displacement field $\mathbf{D} = \varepsilon_0 \mathbf{E} + \mathbf{P}$ in linear response with $\mathbf{J} = -i\omega\mathbf{P}$ one has $\mathbf{P} = \frac{\mathbf{J}}{-i\omega}$. The relative permittivity is

$$\varepsilon(\omega) = 1 + \frac{P(\omega)}{\varepsilon_0 E(\omega)} = 1 - \frac{\sigma(\omega)}{i\varepsilon_0 \omega}. \tag{2.26}$$

Using (2.24) gives the Drude dielectric function

$$\varepsilon_D(\omega) = \varepsilon_\infty - \frac{\omega_p^2}{\omega(\omega + i\gamma_D)} \tag{2.27}$$

where I have included an optional high-frequency background ε_∞ to account for contributions from core electrons and higher-energy interband transitions that are not explicitly modeled by Drude free carriers. Expanding the denominator yields the equivalent form

$$\varepsilon_D(\omega) = \varepsilon_\infty - \frac{\omega_p^2}{\omega^2 + i\gamma_D \omega}. \tag{2.28}$$

Low- and high-frequency limits

The Drude model exhibits distinct behavior in the low- and high-frequency limits. At low frequencies, $\omega \ll \gamma_D$, the conductivity reduces to its DC-value,

$$\sigma_{\mathrm{dc}} \approx \frac{ne^2\tau}{m^*} = \frac{\varepsilon_0 \omega_p^2}{\gamma_D}, \tag{2.29}$$

which is purely real and corresponds to ohmic conduction. In this limit, the imaginary part of the conductivity is negligible, and the dielectric function

$$\varepsilon_D(\omega) \approx \varepsilon_\infty - \frac{\omega_p^2}{i\gamma_D \omega} \approx \varepsilon_\infty - i\frac{\omega_p^2}{\gamma_D \omega}, \tag{2.30}$$

is dominated by a large imaginary component, indicating strong absorption of low-frequency fields by free carriers.

At high frequencies, $\omega \gg \gamma_D$, the damping becomes negligible, and the dielectric response approaches

$$\varepsilon_D(\omega) \approx \varepsilon_\infty - \frac{\omega_p^2}{\omega^2}. \tag{2.31}$$

In this regime, the real part of the dielectric function decreases and can even become

negative for $\omega < \omega_p$, signaling metallic-like behavior where the material reflects incident radiation rather than absorbing it. This behavior is typical for frequencies far below the visible spectrum. The imaginary part becomes small, indicating reduced absorption. For $\omega \gg \omega_p$, the dielectric function approaches the background value ε_∞, as the free carriers can no longer follow the rapid oscillations of the electric field. Thus, the Drude model captures both the low-frequency conductivity-dominated regime and the high-frequency regime where the material exhibits metallic reflectivity or becomes transparent, depending on the relation between ω and ω_p. In typical doped semiconductors, the low-frequency regime (sub-THz to few-THz) is dominated by Drude absorption, while at higher THz or mid-infrared frequencies, the response transitions toward the high-frequency limit described above.

Lorentz model for bound or resonant contributions

Bound carriers (e.g., electrons bound in excitons, intraexcitonic transitions, optical phonons, or localized resonances) respond like driven damped harmonic oscillators having a restoring force. The Lorentz oscillator captures a resonant absorption at a finite eigenfrequency ω_0 with damping γ_L. For a bound charge q (we take $q = -e$ for electrons) with resonance frequency ω_0 and damping γ_L:

$$m^*\ddot{\mathbf{x}}(t) + m^*\gamma_L\dot{\mathbf{x}}(t) + m^*\omega_0^2\mathbf{x}(t) = -e\mathbf{E}(t). \tag{2.32}$$

Assuming $\mathbf{x}(t) = \mathbf{x}(\omega)e^{-i\omega t}$ yields

$$\mathbf{x}(\omega) = \frac{e}{m^*}\frac{1}{\omega_0^2 - \omega^2 - i\gamma_L\omega}\,\mathbf{E}(\omega). \tag{2.33}$$

The polarization per unit volume for N such oscillators is

$$\mathbf{P}(\omega) = -Ne\mathbf{x}(\omega) = \frac{Ne^2}{m^*}\frac{1}{\omega_0^2 - \omega^2 - i\gamma_L\omega}\,\mathbf{E}(\omega). \tag{2.34}$$

Thus the susceptibility $\chi(\omega)$ and dielectric function contribution are

$$\chi_L(\omega) = \frac{Ne^2}{\varepsilon_0 m^*}\frac{1}{\omega_0^2 - \omega^2 - i\gamma_L\omega} \quad \Rightarrow \quad \varepsilon_L(\omega) = 1 + \chi_L(\omega). \tag{2.35}$$

It is common to define an oscillator strength or resonance plasma frequency $\Omega^2 \equiv \frac{Ne^2}{\varepsilon_0 m^*}$, giving

$$\varepsilon_L(\omega) = \varepsilon_\infty + \frac{\Omega^2}{\omega_0^2 - \omega^2 - i\gamma_L\omega}. \tag{2.36}$$

Here ε_∞ again captures higher-frequency background contributions.

Combined Drude–Lorentz dielectric function

The response of semiconductors can be described by a macroscopic approximation using a linear combination of free carrier contributions (Drude) and bound contributions (Lorentz). By superposition (linear response) the total dielectric function is

$$\varepsilon(\omega) = \varepsilon_\infty - \frac{\omega_p^2}{\omega(\omega + i\gamma_D)} + \sum_j \frac{\Omega_j^2}{\omega_{0,j}^2 - \omega^2 - i\gamma_j\omega}, \tag{2.37}$$

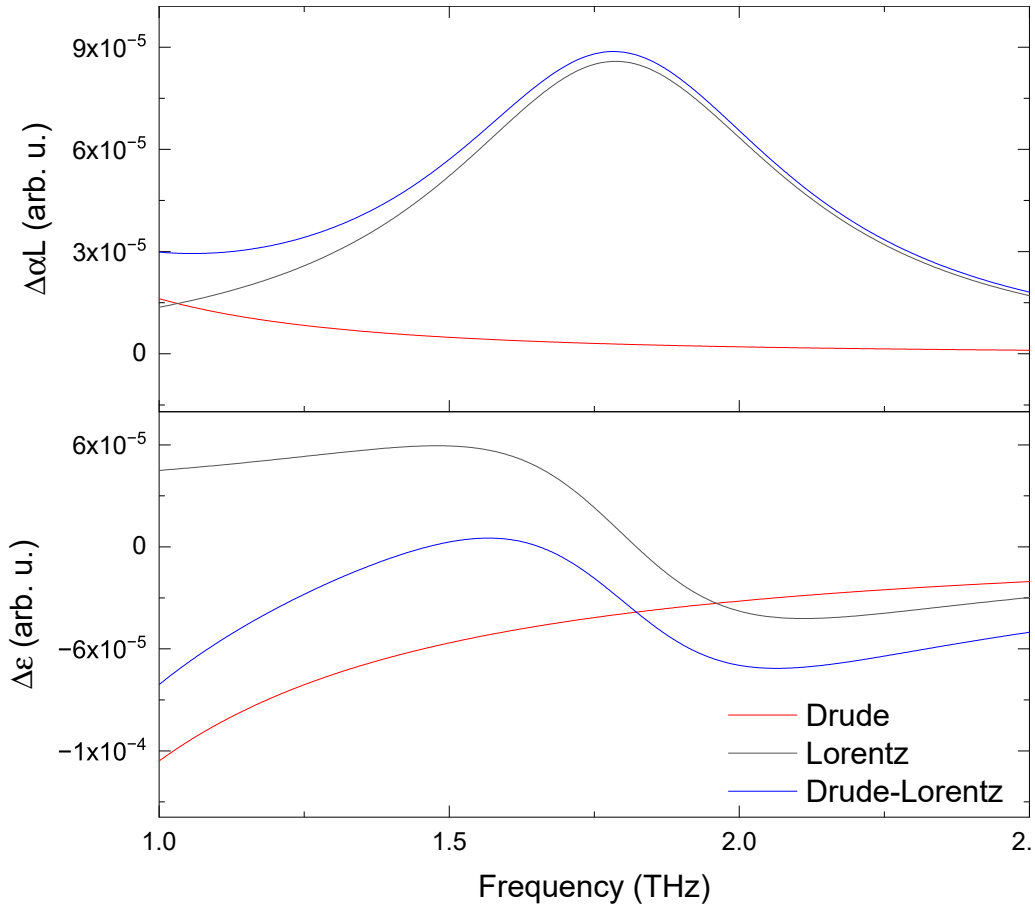

Figure 2.4: Schematic illustration of the Drude and Lorentz contributions to the THz response of semiconductors, shown as the change in absorption (top) and the change in the real part of the dielectric function (bottom). The Drude response (red), representing free-carrier absorption, exhibits a smooth and monotonic behavior. In contrast, the Lorentz contribution (gray), associated with resonant bound excitations, displays a pronounced peak at the resonance frequency. The combined Drude–Lorentz response (blue) highlights the interplay between free-carrier and resonant contributions to the overall THz response.

where the index j enumerates Lorentz oscillators (intraband resonances, excitonic transitions, optical phonons, etc.).

From dielectric function to THz absorption

Define the complex refractive index $\tilde{n}(\omega) = n(\omega) + i\kappa(\omega)$ by

$$\tilde{n}(\omega) = \sqrt{\varepsilon(\omega)}.$$

The absorption coefficient $\alpha(\omega)$ (intensity decay per length) is related to the imaginary part κ by

$$\alpha(\omega) = \frac{2\omega}{c}\,\kappa(\omega) = \frac{2\omega}{c}\,\mathrm{Im}\,\sqrt{\varepsilon(\omega)}. \tag{2.38}$$

In many THz contexts, the imaginary part of the dielectric function is much smaller than the real part, $\mathrm{Im}\,\varepsilon(\omega) \ll \mathrm{Re}\,\varepsilon(\omega)$. This allows one to use the small-loss approximation,

which simplifies the treatment of complex refractive indices and absorption. The physical motivation for this approximation is that in typical THz experiments the absorption is weak, so the imaginary part of the refractive index is small compared to its real part, and the phase velocity is dominated by $\mathrm{Re}\,\varepsilon$. This also makes analytical expressions more transparent and avoids cumbersome computations of the exact complex square root, introducing only negligible error $\sim (\mathrm{Im}\,\varepsilon/\mathrm{Re}\,\varepsilon)^3$. Under this approximation, the extinction coefficient is given by

$$\kappa(\omega) \approx \frac{\mathrm{Im}\,\varepsilon(\omega)}{2\sqrt{\mathrm{Re}\,\varepsilon(\omega)}}, \tag{2.39}$$

and the corresponding absorption coefficient becomes

$$\alpha(\omega) \approx \frac{\omega}{c}\frac{\mathrm{Im}\,\varepsilon(\omega)}{\sqrt{\mathrm{Re}\,\varepsilon(\omega)}}. \tag{2.40}$$

This linear dependence on $\mathrm{Im}\,\varepsilon$ provides a clear physical interpretation: the absorption is directly proportional to the material losses, while the propagation is primarily determined by the real part of the dielectric function. Figure 2.4 displays the frequency-dependent behavior of Drude and Lorentz response. The Drude term ($\propto \omega_p^2$) produces a broadband, monotonically increasing absorption at low frequencies (for finite γ_D) characteristic of free-carrier intraband absorption. In THz experiments this term often dominates the low-frequency (sub-THz to few-THz) conductivity and absorption of doped or photo-excited semiconductors. The Drude conductivity yields a peak in $\mathrm{Re}\,\sigma(\omega)$ at $\omega \approx 0$ with width set by γ_D. The Lorentz term ($\omega_{0,j}$ finite) produces a resonant absorption peak at frequency $\omega \approx \omega_0$ with Lorentzian lineshapes determined by γ_L. Intraband excitonic transitions (e.g., $1s \to 2p$) and optical phonons appear as Lorentz oscillators in the THz spectral window. Excitonic intra-level transitions typically appear at distinct THz frequencies and can be used to identify exciton populations; however, strong dephasing broadens these resonances. In photo-excited semiconductors both contributions can coexist; the Drude background can obscure weak Lorentz resonances and the presence of free carriers can screen Coulomb interaction, reduce oscillator strengths, and broaden excitonic resonances.

Explicit forms often used in fits

Typically, the excitation induced change in response of semiconductors in the THz range is dominated by the $1s$–$2p$ absorption resonance although s-np transitions are in principle also allowed [11, 35]. Contributions from higher-lying p-states can usually be neglected as the corresponding transition probability decreases rapidly with increasing principle quantum number n [52–54]. Since one can neglect the contributions from p-states other than $2p$, one can get a practical form for fitting experimental THz data. In an optical pump–THz probe experiment, the relevant quantity is the pump-induced change in the dielectric function, $\Delta\varepsilon(\omega) = \varepsilon_{\mathrm{pumped}}(\omega) - \varepsilon_{\mathrm{unpumped}}(\omega)$, obtained by subtracting the unexcited-sample reference from the pumped response. Applying the Drude–Lorentz model (2.37) to this differential signal, and retaining only the dominant $1s$–$2p$ intraexci-

tonic resonance (see discussion above), yields the practical fitting form

$$\Delta\varepsilon(\omega) = \frac{e^2}{L\,\varepsilon_0\,\mu}\left(\underbrace{\frac{f_{1s\text{-}2p}\,n_x}{\omega_{\mathrm{res}}^2 - \omega^2 - i\omega\,\Delta_{\mathrm{hom}}}}_{\text{I: intraexcitonic absorption}} - \underbrace{\frac{n_{fc}}{\omega^2 + i\omega\,\Gamma}}_{\text{II: Drude response}}\right), \tag{2.41}$$

where L is the active-layer thickness (width of all quantum wells), $\mu = {}^{m_e^* m_h^*}/_{m_e^* + m_h^*}$ is the electron–hole reduced mass, $f_{1s\text{-}2p}$ is the dimensionless oscillator strength of the $1s$–$2p$ transition (proportional to the squared current matrix element $|J_{1s,2p}|^2$ of Equation (2.17)), n_x is the $1s$ exciton sheet density, ω_{res} is the $1s$–$2p$ resonance frequency, Δ_{hom} is the homogeneous linewidth (dephasing rate) of that transition, n_{fc} is the free-carrier sheet density, and Γ is the free-carrier scattering rate. This form is used throughout this thesis. It is comprised of two parts and offers direct access to the relevant parameters. The first part (I) corresponds to intraexcitonic absorption. It allows to extract the exciton density n_x, the resonance frequency ω_{res} and the homogeneous linewidth of the investigated intraexcitonic transition Δ_{hom}. The exciton density is used in Section 5.2 for calculating the inelastic scattering contribution to the total scattering of excitons, which in turn is extracted from the change in homogeneous linewidth Δ_{hom}. The resonance frequency ω_{res} becomes important when investigating the screening of an exciton population by additional charge-carriers in Section 5.3. The second part (II) of the formula corresponds to Drude contributions from an electron–hole plasma. These contributions were not further analyzed in the course of this thesis since its focus lies on the investigation of excitons. However, they were relevant for the investigation of electron-densities in a radio-frequency ion thruster (c.f. [55])

3 Experimental Details

This chapter outlines the relevant experimental concepts used in this thesis. The discussion focuses on THz generation, the employment of THz radiation in optical pump–terahertz probe spectroscopy as well as data analysis in the coherent regime.

3.1 THz generation

Radiation in the terahertz range (0.1–10 THz) sits between the fields of electronics and photonics. This region has historically been referred to as the "THz gap" [56, 57]. The challenge of generating efficient sources has led to a variety of approaches, which can be broadly categorized as coherent or non-coherent techniques. This distinction is important because coherent sources enable phase-resolved spectroscopy and precise emission control, whereas non-coherent sources typically provide broadband power for imaging and thermal applications. Typical sources of incoherent THz radiations are thermal emitters [58], backward wave oscillators (BWO) [59] and vacuum electronics [60]. Thermal emitters are simple and inexpensive sources of broadband THz radiation. However, this comes with a lack of coherence and low brightness, limiting the use of these sources to basic imaging or calibration applications. BWOs in contrast, offer a narrow bandwidth, highly tunable output of THz radiation with output power in the low mW regime [61]. Although they achieve more coherence than thermal or black-body sources, they still fall short of the capabilities of modern phase-locked solutions. This leads to the second type of THz generation, coherent sources. With the advent of ultrafast laser systems, new pathways for THz generation have emerged. One focus of this dissertation is the development of broadband and coherent THz sources. Coherent THz radiation can be generated, for example, via optical rectification [62, 63], laser-induced plasmas [64, 65], spintronic emitters [22, 66], and photoconductive antennas [24, 67]. In general, the emission of a Hertzian dipole in the far-field is directly proportional to the change of current given by:

$$E(t) \propto \frac{d}{dt} I(t). \tag{3.1}$$

If the change of current is on a ps time scale, the resulting emission of Bremsstrahlung is in the THz range. For this thesis, there are two relevant mechanisms to create THz radiation. The first one is quantum interference currents and the second one is the use of a photoconductive antenna. Quantum interference currents, also referred to as coherent control currents, are electrical currents that arise from the coherent superposition of different quantum excitation pathways in a solid-state system. In simple terms, they emerge when electrons are excited, for example, by two laser fields of different frequencies, typically ω and 2ω. In this scenario, an electron can reach a conduction band state through at least two distinct pathways: one by absorbing two ω photons, and another by absorbing a single 2ω photon. Both pathways terminate in the same final state and possess a well-defined relative phase. The associated probability amplitudes interfere either constructively or destructively. By carefully controlling the relative phase of the two optical fields, the interference can be made asymmetric, resulting in more electrons being

generated with momentum $+k$ than with $-k$. This produces an asymmetric momentum distribution, which corresponds to a macroscopically measurable current pulse, either by electrically contacting the sample or measuring the emitted radiation [68].

After excitation, the total state of the system can be written as

$$|\psi\rangle = c_1|\text{Path 1}\rangle + c_2|\text{Path 2}\rangle, \tag{3.2}$$

where the complex coefficients c_1 and c_2 depend on the amplitudes and phases of the optical fields. Adjusting the relative phase between the ω and 2ω fields changes the interference of the pathways, and consequently, the direction and magnitude of the generated current. In the absence of interference, a symmetric crystal would yield equal transition probabilities to states $+k$ and $-k$, resulting in zero net current. Quantum interference breaks this symmetry, so that

$$\rho(k) \neq \rho(-k), \tag{3.3}$$

and the time derivative of the expectation value of momentum or velocity gives rise to a net charge current. Because the currents are tied to the coherence of the excitation, they are ultrashort (femtosecond timescale) and their direction can be controlled via the optical phase. This property makes them particularly interesting for phase-controlled electronics [69], THz emission [68], and coherent control experiments [70].

Quantum interference currents are often described using a simple $\omega/2\omega$ model, in which a current injection term is proportional to the field amplitudes and their relative phase. Consider two coherent fields with frequencies ω and 2ω, and complex field amplitudes

$$E_\omega = |E_\omega|e^{i\phi_\omega}, \quad E_{2\omega} = |E_{2\omega}|e^{i\phi_{2\omega}}. \tag{3.4}$$

In the simplest model, the time derivative of the injected current can be written as

$$\frac{dJ_i}{dt} = \eta_{ijk} E_{\omega,j} E_{\omega,k} E^*_{2\omega} + \text{c.c.}, \tag{3.5}$$

where η_{ijk} is a third-rank current injection tensor determined by the band structure and transition dipoles, e.g., from a $k \cdot p$ model [71]. By substituting

$$E^2_\omega E^*_{2\omega} \propto |E_\omega|^2 |E_{2\omega}| e^{i(2\phi_\omega - \phi_{2\omega})}, \tag{3.6}$$

one obtains the scalar current which is typically given by

$$\frac{dJ}{dt} \propto |E_\omega|^2 |E_{2\omega}| \cos\left(2\phi_\omega - \phi_{2\omega} + \phi_0\right), \tag{3.7}$$

where ϕ_0 depends on material properties and geometry [72]. The essential features of this model are:

- The current is proportional to the product of the field amplitudes, e.g., $E^2_\omega E_{2\omega}$.
- It depends sinusoidally on the relative phase $2\phi_\omega - \phi_{2\omega}$; adjusting this phase reverses the current direction.
- In k-space, this corresponds to an interference term between one-photon and two-photon excitation pathways, yielding $\rho(k) - \rho(-k) \neq 0$.

Quantum interference currents in Paper II and the results are explained in detail in Chapter 4. Since this emission scheme is still under active investigation, the other ex-

periments in this thesis were conducted using a more established method, namely the use of a photoconductive antenna. Here, a semiconductor material gets processed with an antenna structure. An optical laser pulse excites the semiconductor material while a bias is applied to the electrodes of the antenna structure. The generated charge-carriers then get accelerated by the electric field between the electrodes. This leads to a transient electric current perpendicular to the direction of incidence. Similar to the aforementioned quantum interference currents, the emission can be modeled by Equation (3.1). In order to obtain THz emission, the optical excitation needs to be on a (sub-)picosecond timescale followed by a rapid recapture of the charge-carriers. The semiconductor material of the THz antennas used in this thesis is GaAs grown at low temperatures. Due to the low growth temperature, the substrate material is full of defects which work as trapping and recombination centers for the charge-carriers. However, these defects decrease the conductivity of the substrate material, resulting in a decrease in output power. More detailed descriptions of photoconductive antennas can be found in the literature [24, 73, 74].

3.2 THz detection/electro-optical sampling

Similar to THz generation, THz detection can be divided into coherent and incoherent detection schemes. Examples for incoherent detectors are Golay cells [75], bolometer [76], or pyroelectric detectors [77]. They convert the incoming THz radiation into an electrical signal proportional to its intensity, not to the time-varying electric field. They provide simple, inexpensive methods to measure radiation from visible/UV to THz wavelengths [78]. Their main advantage lies in their small footprint and their ability to detect THz radiation over wide spectral ranges [79]. This makes them suitable for imaging and power monitoring applications. In contrast, coherent detection captures both the amplitude and the phase, enabling time-domain (or frequency-resolved) measurement of the electromagnetic field. Prominent examples for coherent detection schemes are air biased coherent detection (ABCD), photoconductive sampling, or electro-optic sampling (EOS). The latter will be explained more in detail since it will be the detection method used in this thesis. A schematic of this method is shown in Figure 3.1. The fundamental

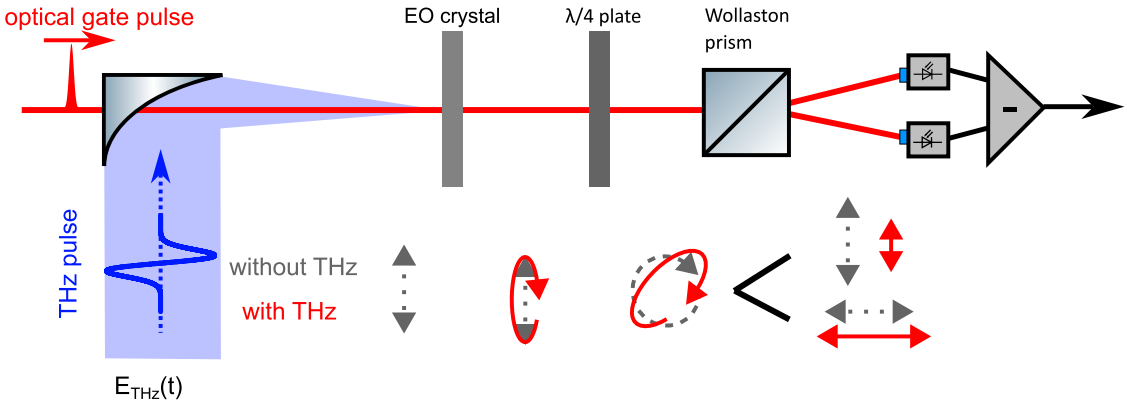

Figure 3.1: Schematic of EOS detection. An optical gate pulse and a THz pulse are focused onto the electro-optic detection crystal. A delay line allows to temporally delay the optical and the THz pulse. The electric field of the THz pulse changes the refractive index of the crystal, resulting in a change of the optical pulse's polarization. The polarization of the optical pulse with and without THz are depicted by the red and gray arrows respectively.

effect used in EOS is the Pockels effect or linear electro-optic effect [80]. Applying an electric field to a non-centrosymmetric crystal results in induced birefringence [81–83]. The induced change in the crystal's refractive index is described by the linear relation [84]:

$$\Delta n = n_0^3 r_{ij} E_{\mathrm{THz}} \tag{3.8}$$

where n_0 is the unperturbed refractive index, r_{ij} is the relevant electro-optic tensor component, and E_{THz} is the applied THz electric field. The relevant electric field does not have to be static; it can also be time-varying, for example in the form of an optical or other electromagnetic wave. When considering electromagnetic waves with sufficiently long wavelengths, the field can be considered uniform across significant regions of the crystal at any given moment. Within these regions, the applied field induces a modulation of the refractive index via the electro-optic effect. This modulation is monitored using a probe beam, enabling direct measurement of the long-wavelength field. The probe beam is an optical pulse which is much shorter in time than the THz wave inducing the change in refractive index. During temporal overlap of probe pulse (gate pulse) and THz in the EO crystal the birefringence leads to a phase shift $\Delta\phi$ between ordinary and extraordinary contributions of

$$\Delta\phi = 2\pi \frac{d}{\lambda} \Delta n. \tag{3.9}$$

Typical crystals used for EOS of THz waves are ZnTe <110>, GaP <110>, and z-cut GaSe. The first two are zinc-blende structure crystals. This means that all electro-optic coefficients apart from $r_{41} = r_{52} = r_{63}$ are zero [85]. Consequently, if the optical probing pulse is polarized by 45° with respect to the optical axis, it experiences a phase shift of [84]:

$$\Delta\phi = \pi \frac{d}{\lambda} n_0^3 r_{41} E_{\mathrm{THz}}(t). \tag{3.10}$$

Without a THz field applied to the electro-optical crystal, the linearly polarized gate pulse is transformed into circularly polarized light by a $\lambda/4$ plate. A Wollaston prism then separates the horizontal and vertical polarization contributions. A pair of photodiodes then detects the resulting orthogonally polarized beams. In the case of circularly polarized light both beams have the same intensity, resulting in the same signal for each photodiode. This leads to the signals canceling out. When a THz field is applied to the EO crystal, the gate pulse gets elliptically polarized. This results in different signals of the photodiodes. The difference in signals is directly proportional to the electric field of the THz pulse. Changing the delay between THz and gate pulse allows to sample the entire THz pulse in the time domain. One crucial consideration for choosing the electro-optical crystal is the wavelength of the gate pulse and the bandwidth of the THz pulse [86–88]. The mismatch between the optical group and THz phase velocity dictates the response for different frequency contributions of the THz pulse while the absorption of the nonlinear crystal limits the detectable bandwidth. In practice, choosing a thinner detection crystal allows to circumvent the phase mismatch to a certain degree, however, this comes at the cost of signal strength.

3.3 Optical pump-terahertz probe spectroscopy

Optical pump-terahertz probe spectroscopy is a proven tool to study quasiparticles in semiconductors [9, 11, 89]. The energy range of THz photons allows to uniquely address intraexcitonic transitions, thus circumventing the limitations of optical spectroscopy [90, 91]. The experimental setup underwent several changes, depending on the requirements

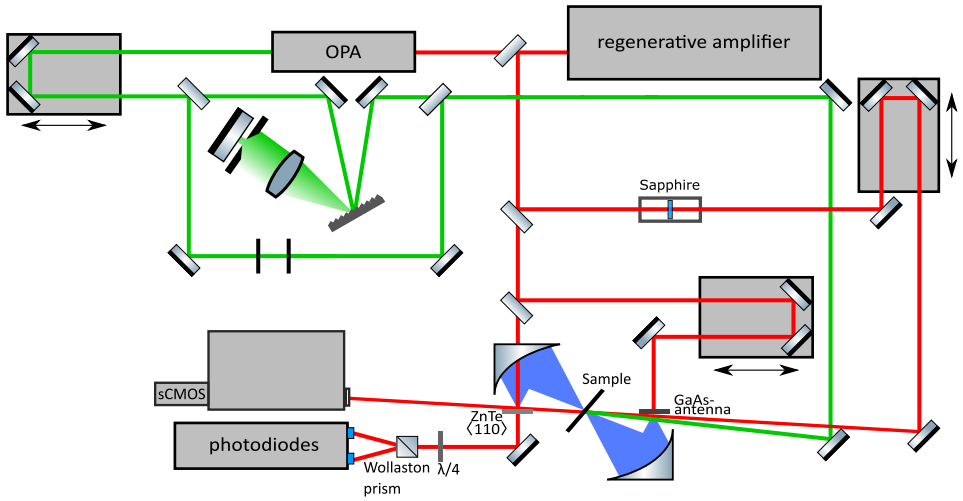

Figure 3.2: Schematic illustration of the experimental pump–probe setup. The experiment is based on a regenerative laser amplifier system, whose output is split into two beams. One beam pumps an optical parametric amplifier, which provides the optical pump for the sample. The wavelength can be fine-tuned using a subsequent pulse shaper and a combination of long- and short-pass filters. The second beam from the regenerative amplifier is used for probe generation. One fraction is focused onto a sapphire crystal to generate a white-light supercontinuum for optical probing. The remaining fraction is used for THz generation via an LT-GaAs antenna, with detection performed by EOS.

for the task at hand. However, the basic concept remains the same. A schematic drawing is found in Figure 3.2. The starting point is a regenerative amplifier system (Spectra Physics Solstice Ace) which delivers 50 fs pulses with a central wavelength of 800 nm and a pulse repetition rate of 5 kHz. The amplifier's output is split into three parts. The first part is focused in a sapphire crystal to generate a white-light supercontinuum. The crystal can be water-cooled to prevent thermal damage while also allowing to interchange different crystals. Changing the thickness of the crystal allows to adjust the spectrum of the white-light. The white-light then passes over a delay line for temporal adjustment. Afterwards it is focused onto the sample. During the measurement, the sample is held at a constant 6 K in a continuous flow liquid Helium (He) cryostat. After passing through the sample, the transmitted white-light is analyzed using an imaging spectrometer (Andor Shamrock 500i). Dispersion in the spectrometer is provided by various reflective aluminum gratings. For most of the data in this work a grating with 600 $^{\text{lines}}/_{\text{mm}}$ and a blaze of 800 nm was used. The dispersed white-light is then analyzed by a scientific complementary metal-oxide semiconductor (sCMOS) camera (Andor Zyla 5.5). The second part of the amplifier's output is directed onto the a large-aperture low temperature grown GaAs antenna to generate the THz pulses. The THz pulse is focused onto the sample by an ellipsoidal mirror. After probing the sample, the divergent THz pulse is re-focused onto a 500 µm thick ZnTe crystal, again using an ellipsoidal mirror. The probe pulse then coincides with the third part of the amplifier's output. This beam is focused onto the ZnTe and serves as the gate pulse for the electro-optical sampling. The last part of the amplifier's output is fed into an optical parametric amplifier (TOPAS Twins). This allows to tune the wavelength from 240 nm to 2400 nm. The output then gets routed over another delay into a pulse shaper. The pulse shaper allows to finetune

the excitation wavelength as well as its linewidth. After the pulse shaper, the optical pulse gets directed unto the sample to excite the sample.

Interpolation of data for the coherent regime

Scanning a THz pulse with EOS can be done in two ways. Since gate pulse and THz pulse need to be delayed with respect to one another, one can either delay the gate pulse or the THz pulse. Both scenarios will result in the same outcome. For OPTP this becomes more difficult. Here, the introduction of a third pulse means that two pulses need to be delayed to obtain the full 2D data set. This results in three times that can be defined:

- $T_{\text{Pump-Gate}}$ which corresponds to the time difference between optical pump and gate pulse. This is the time measured in the setup used in this dissertation.
- T_{EOS} which is the time difference between gate and THz pulse. This is the time for sampling the THz pulse.
- T_{PP} which is the time between optical excitation and THz probe pulse.

Generally, if the delay between the optical pump and the THz probe pulse exceeds the duration of the probe pulse, delaying either the THz pulse or the gate pulse yields equivalent results. However, when the pump–probe delay approaches the probe pulse duration—or becomes even shorter—the method of data acquisition becomes crucial.
For early pump arrival times, the THz probe pulse experiences significantly different excitation conditions within its temporal envelope. In the most extreme case, the leading edge of the THz pulse interacts with an unexcited sample, while the trailing edge probes a partially or fully excited one. Furthermore, the excitation of the sample is itself time-dependent, meaning that even for THz pulses arriving after the excitation, different portions of the pulse encounter distinct excitation conditions [92, 93].
To accurately represent coherent effects, the experimental timing must reflect the actual physical scenario—specifically, it should correspond to a fixed delay between the optical pump and a chosen reference point within the THz probe pulse. In the setup shown

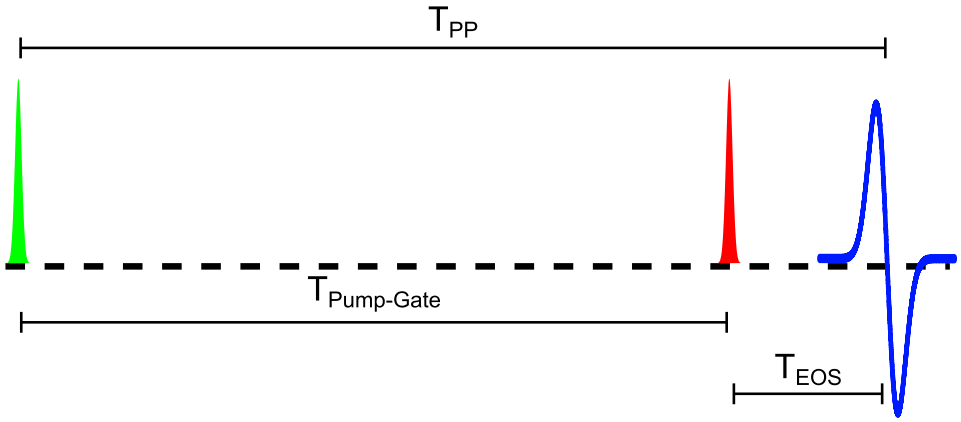

Figure 3.3: Definition of the different times measured in the OPTP experiment. $T_{\text{Pump-Gate}}$ is defined as the time delay between optical excitation and optical gate pulse, T_{EOS} is the time for sampling the THz pulse, T_{PP} is the physical time between optical pump and THz probe pulse. In the setup used for this thesis, $T_{\text{Pump-Gate}}$ and T_{EOS} are measured. T_{PP} needs to be extracted by interpolation and taking the diagonal of the 2D data set.

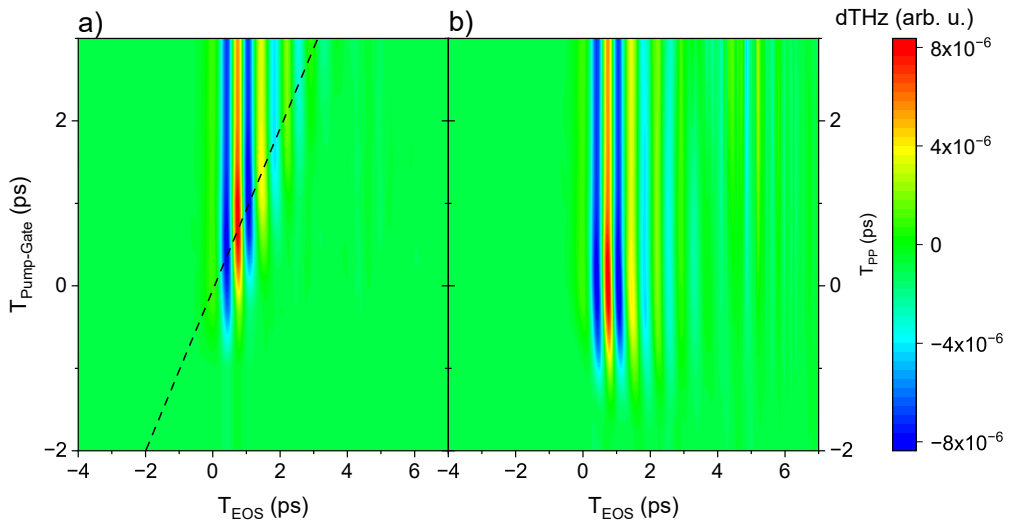

Figure 3.4: Exemplary 2D TDS scans for resonant excitation. a) Measured dTHz traces from the setup. Below and to the right of the dashed line is the unexcited sample. b) Corrected dTHz traces. The y-axis now corresponds to the physical pump probe delay T_{PP} between optical pump and THz probe.

in Figure 3.2, the pump and THz delay stages are scanned while the EOS gate pulse remains fixed. Consequently, the recorded data depend on $T_{\text{Pump-Gate}}$ and T_{EOS}. For a fixed position of the pump delay line, one can acquire a one-dimensional probe scan. Likewise, fixing the THz delay line at the peak of the THz pulse and scanning the pump delay line yields a one-dimensional pump scan. To analyze the data in a physically consistent way—especially when investigating coherent effects—it must be transformed into a representation using T_{PP}. A comparison between the raw dTHz signal and its T_{PP}-transformed representation is shown in Figure 3.4. In Figure 3.4 a) the data is shown measured with the setup. The dashed black line corresponds to time zero, which is defined at the half-maximum of the signal following resonant excitation. This definition is justified by assuming that, at this point, approximately half of the optical pump pulse has interacted with the sample, corresponding to the temporal maximum of the pulse envelope. Every data point below and to the right of the dashed line corresponds to the unexcited sample. To get from one representation to the other, a Python script is executed. This interpolates the data and extracts the diagonals for each pump delay. These are then plotted accordingly. The original T_{EOS} corresponds to the new one. The obtained representation is shown in Figure 3.4 b). This procedure is particularly important for investigations in the coherent regime. An example where this is needed is presented in Section 5.4.

Estimation of THz field strength

For many applications, an estimation of the THz probe's field strength is needed. Here, the EOS technique is helpful, as it directly measures the electric field of the THz pulse. For small enough E-fields the polarization modulation is linearly proportional to the E-field [94]. The phase shift φ due to the induced birefringence in an electro-optic crystal can be described by [95]:

$$\varphi = \frac{2\pi}{\lambda} L n_0^3 r E_{\text{THz}} T_{\text{Fr}}, \tag{3.11}$$

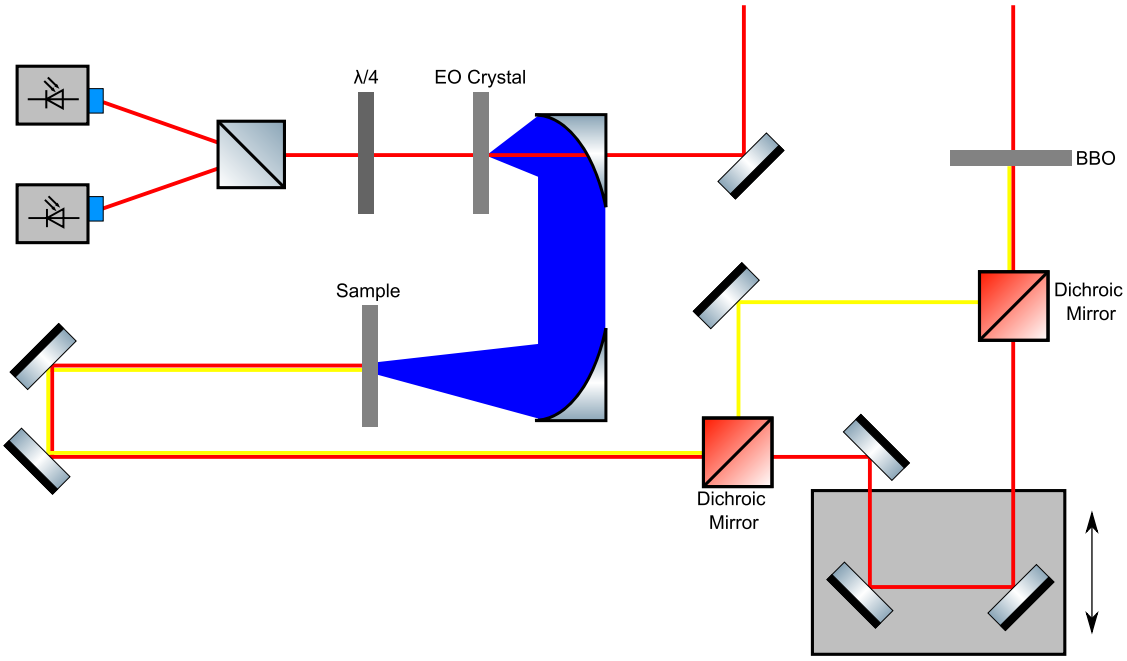

Figure 3.5: Schematic of THz emission setup. The fundamental gets focused on the BBO to generate the second harmonic. Fundamental and second harmonic get separated by a dichroic mirror. The fundamental laser beam gets routed via a delay line. This delay line allows to change the temporal overlap between fundamental and second harmonic. Both laser beams get recombined by another dichroic mirror. The emitted THz radiation of the sample gets collected by one parabolic mirror and detected via electro-optical sampling.

where λ is the wavelength of the gate pulse, L is the thickness of the EO crystal, n_0 is the refractive index, r is the electro-optic coefficient of the detection crystal, and T_{Fr} the Fresnel transmission coefficient. For ZnTe typical values in our experiments are $\lambda = 800\,\mathrm{nm}$, $\mathrm{r} = 3.9\,\mathrm{pm/V}$, $n_0 = 2.8$, $T_{\mathrm{Fr}} = 0.52$. The detected signals of the photodiodes is directly proportional to the phase shift φ:

$$\varphi = \arcsin\left(\frac{I_{\mathrm{a}} - I_{\mathrm{b}}}{I_{\mathrm{a}} + I_{\mathrm{b}}}\right). \tag{3.12}$$

Here, I_{a} and I_{b} denote the signal of the individual photodiodes. Subsequently, the E-field of the THz pulse can be calculated by

$$E_{\mathrm{THz}} = \frac{\arcsin\left(\frac{I_{\mathrm{a}} - I_{\mathrm{b}}}{I_{\mathrm{a}} + I_{\mathrm{b}}}\right)\lambda}{2\pi L n_0^3 r T_{\mathrm{Fr}}}. \tag{3.13}$$

3.4 THz emission

The optical setup employed in this experiment is schematically illustrated in Figure 3.5. A Ti:Sapphire laser-based amplifier (Solstice Ace) with a pulse duration of 50 fs, a central wavelength of 800 nm, and a repetition rate of 5 kHz provides the primary light source. The output is split into two paths: a small fraction serves as the gate pulse for electro-optic sampling, while the remaining portion pumps an optical parametric amplifier (TOPAS Twins). The OPA converts the 800 nm radiation into the desired signal

wavelength centered around 1590 nm (0.78 eV). The OPA output is directed through a delay line and focused onto a BBO crystal to generate the second harmonic at 795 nm (1.56 eV). Pulse energies of 480 nJ and 280 nJ are used for the fundamental and second harmonic, respectively. Both beams are incident on a dichroic mirror that reflects wavelengths below 900 nm (i.e., the second harmonic) while transmitting the fundamental. To precisely control the relative phase between the two beams, a secondary delay stage is introduced. Although the manufacturer specifies a bidirectional positioning accuracy of 1 µm—corresponding to a temporal resolution of approximately 6.7 fs—the stage is operated uni-directionally during phase scans, significantly improving its effective precision. Based on the manufacturer's specifications and our own interferometric calibration, the practical unidirectional timing accuracy is estimated to be approximately 0.2 fs. The polarization of the fundamental beam is adjusted using a half-wave plate and, together with a polarization filter, ensures collinear polarization with its second harmonic. Both beams are then recombined using another dichroic mirror, and the superimposed beams are focused onto the Ge samples using a 20 cm focal length lens. The generated THz pulse is collimated by a parabolic mirror with a focal length of 101.6 mm and subsequently focused onto a 500 µm-thick ZnTe or a 100 µm-thick GaP detection crystal by another parabolic mirror with a focal length of 50.8 mm. At the detection crystal, the THz pulse is spatially and temporally overlapped with the gate pulse for electro-optic sampling. By introducing a variable delay between the OPA output (and thus the THz pulse) and the gate pulse, the complete THz waveform is sampled in the time domain.

4 THz generation by coherent currents in Germanium

For many decades the spectral range of THz waves remained elusive, since it lies between the optically or electronically accessible ranges of electro-magnetic radiation. In recent years, this gap was closed more and more. However, the quest for new THz sources remains unbroken. As described in Section 3.1, multiple mechanisms an techniques have been developed. One of the most commonly used devices for coherent THz generation are GaAs-based antennas [96–98]. They offer ease of use, commercial availability and stable output up to 6 THz [99]. Another widespread method is optical rectification in III-V or II-VI semiconductors like ZnTe, GaP, or GaSe [100–102]. However, their spectral range is limited due to the infrared-active phonon modes of these polar semiconductors. They are constrained to below 4-7 THz or above 12-15 THz. Alternative approaches to generate THz radiation in the spectral region unattainable by the aforementioned methods is by spintronics [22, 103] or two-color air plasma [64, 104–106]. These methods either lack the output power or require costly laser amplifier systems. Another solution to achieve gap-less THz radiation would be the use of non-polar semiconductors as they lack the hindering phonon modes. Prominent examples are Silicon and Germanium, the latter featuring higher electron mobility. Germanium has already been demonstrated to be a suitable material for broadband THz emission in a photoconductive antenna [30, 107]. While they do not suffer the phonon absorption of their GaAs-based counterparts, these antennas still need complex processing and contacting [24, 74]. Ideally, one would want to combine the promising material properties of Germanium with a less complex and cumbersome way to generate currents. Typically, charge-carriers get injected optically into a semiconductor material. So why not accelerate these charge-carriers with light and create an optically driven current? One way would be via so-called quantum interference currents [28, 29]. In this case, the simultaneous coherent excitation of one-photon and two-photon transitions in a semiconductor can be induced using the fundamental frequency and its second harmonic of a below-bandgap femtosecond laser pulse. This excitation facilitates coupling between electronic transitions in the valence and conduction bands. The relative phase between the two optical fields governs the interference of the interband transition amplitudes, thereby generating a polar asymmetry in the momentum-space distribution of the photoexcited charge-carriers. This asymmetry gives rise to an optically injected quantum interference current density, which can be directly characterized through the emitted THz radiation [108–113].

In this publication, I make use of the setup described in Section 3.4. To show a proof of principle, two things need to be present. One, exciting the sample with two optical pump beams needs to emit THz radiation. Two, the emitted THz radiation should depend strongly on the phase delay between the two optical pulses. There should be a periodicity of 2π and the polarity of the THz pulse should be changeable. For this, I excited the sample with 1590 nm as fundamental and 795 nm as the second harmonic. By changing the delay of the two optical pulses I am able to change the relative phase of the two pulses. Results are shown in Figure 4.1. Here, one can see that the sample indeed does emit THz radiation. Additionally, the polarity of the THz radiation cor-

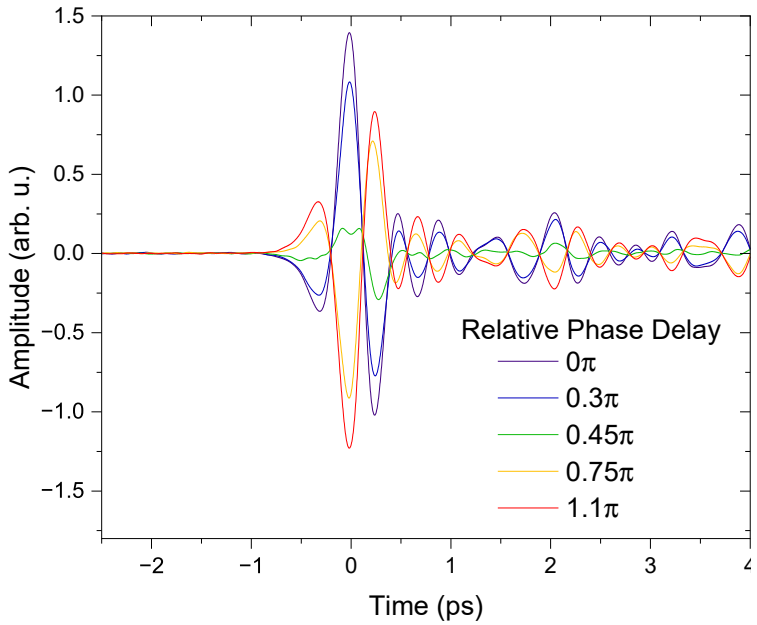

Figure 4.1: THz emission depending on the phase of fundamental and second harmonic optical pulse. Delaying the two optical beams against each other results in a change of polarity of the emitted THz radiation. The change of polarity follows a 2π-periodicity which is characteristic for THz emission from quantum interference currents.

relates strongly with the relative phase between the two optical pulses. Changing the phase by half the wavelength of the second harmonic allows to invert the polarity of the emitted THz pulse. This is equal to a phase shift of π. Furthermore, for a delay of a quarter wavelength of the second harmonic (relative phase shift of $\pi/2$) almost completely suppresses the THz emission. This is due to symmetric k-space injection conditions. The emitted THz radiation now needs to be characterized. For applications, the bandwidth, field strength, and asymmetry ratio are of interest. For many applications like sub-cycle THz scanning tunneling microscopy the asymmetry ratio between the two largest half-cylces of opposite sign are of interest [31, 114–116]. In the top of Figure 4.2 it is shown, that I obtain an asymmetry ratio of 3.34:1 and a FWHM of the emitted THz pulse of 110 fs. This asymmetry ratio is greater than spintronic emitters and comparable to pulses emitted from type-II MQW structures [114]. In the case of type-II MQW as well as quantum interference currents the origin is a redistribution of an induced current into an equilibrium, which explains the similar shape of the emitted THz pulse. The bandwidth of the emitted pulses is shown in the bottom of Figure 4.2. The emission spans several octaves, reaching up close to the reststrahlen band of GaP at 8 THz [27]. The spectrum is flat from 1–3.5 THz with a maximum at around 2 THz. Although the reststrahlen band of GaP prohibits measurements around 8 THz, one can see that the signal significantly drops already at 7 THz. Here, the limiting factor is the bandwidth of the optical pulses. The pulse-bandwidth product TBP for a transform limited pulse is defined as

$$\mathrm{TBP} = \Delta\tau\Delta\nu, \tag{4.1}$$

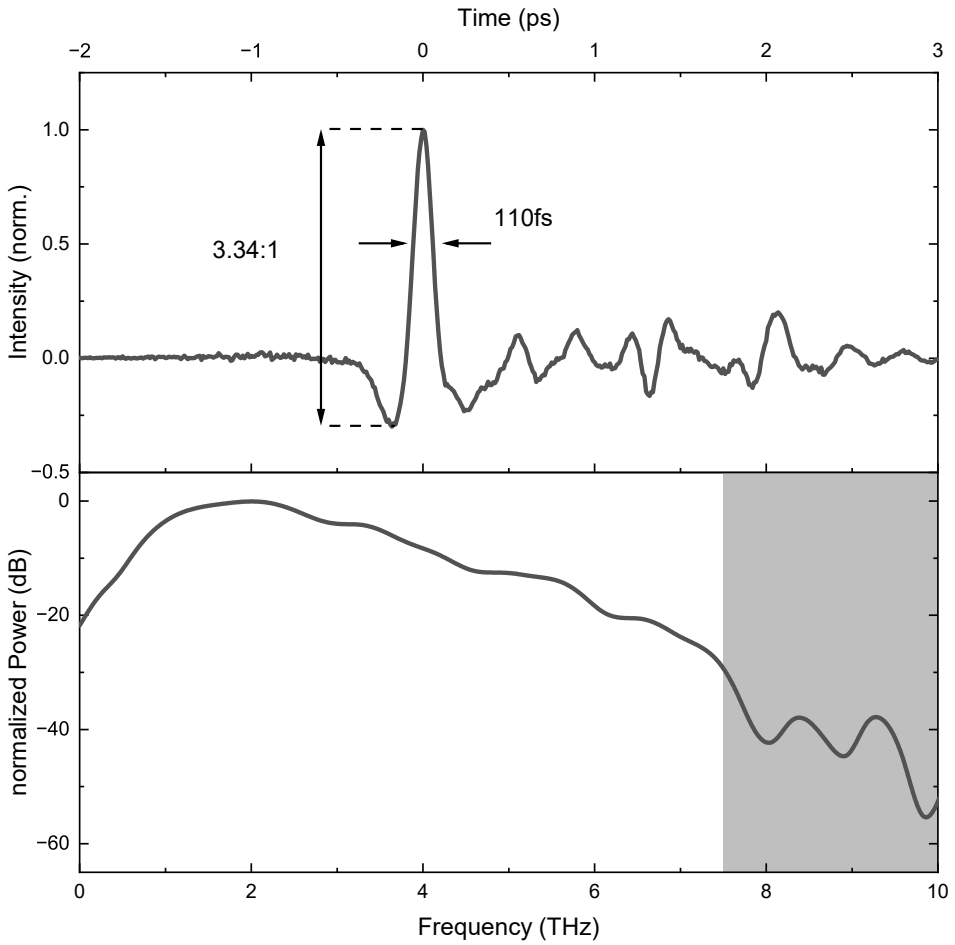

Figure 4.2: Top: Time trace of the THz emission using 1590 nm and 795 nm pulses. The emitted THz time trace shows a high asymmetry with a ratio of 3.34:1 for the main positive and negative peaks. The FWHM of 110 fs is marked by two arrows.
Bottom: Corresponding spectrum of the emitted THz radiation. The gray-shaded area indicates the spectral region, where the signal-to-noise ratio is not sufficient anymore. Measurements were taken using a 100 µm GaP crystal for detection.

where $\Delta\tau$ is the pulse length of the optical pulse and $\Delta\nu$ is the corresponding bandwidth. To calculate the bandwidth of the optical pulse, one needs to consider the pulse shape of the optical pulse. For a gaussian pulse the following holds true:

$$\mathrm{TBP}_{\mathrm{Gaussian}} = \frac{2\log 2}{\pi} \approx 0.441. \tag{4.2}$$

The pulse duration of the optical pulse can be measured via autocorrelation measurements. I find a pulse length of 63 fs for the second harmonic. This value is in good agreement with scans of the emitted THz pulse for a wider range of delays between fundamental and second harmonic pulses (c.f. Fig. 3 from Paper II). Fitting an envelope to these measurements provides a pulse length of 68 fs. Considering the 63 fs pulse duration,

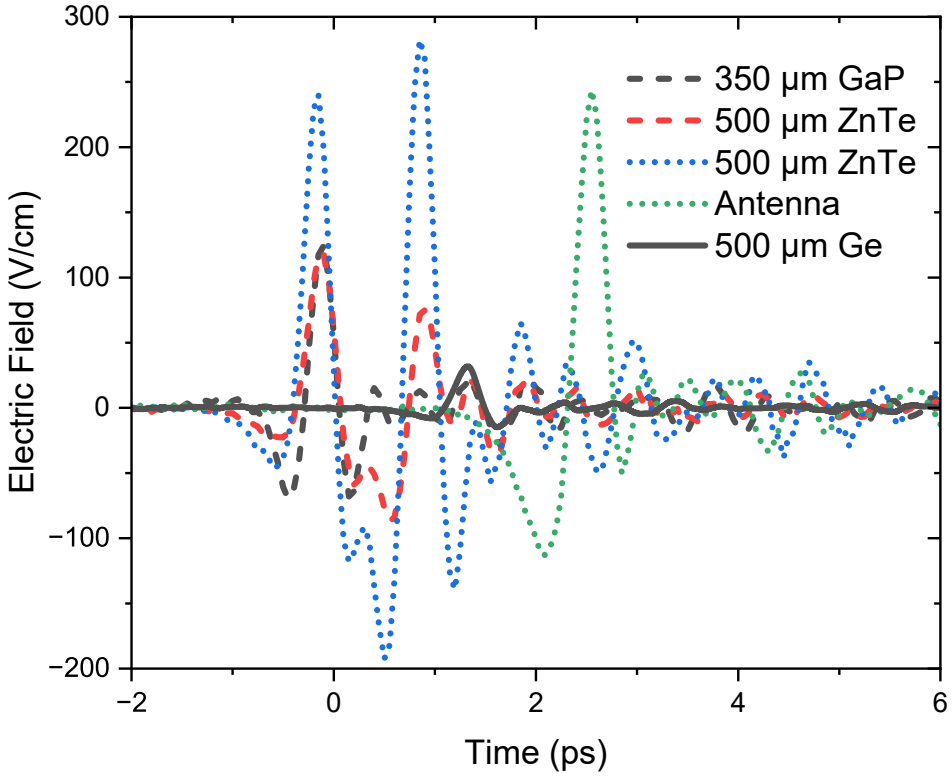

Figure 4.3: Time traces of different THz emitters for identical excitation conditions. The dashed lines correspond to excitations with 1590 nm and the dotted lines to excitations with 795 nm laser pulses. The solid line for Ge represents the two-color excitation scheme. In comparison to more established emitters bulk Ge does emit the weakest electric field.

I subsequently calculate the bandwidth as

$$\Delta\nu = \frac{0.441}{63\,\mathrm{fs}} = 7\,\mathrm{THz}. \tag{4.3}$$

Newly-developed methods always need to be compared to established methods to show their benefits. In Figure 4.3 time traces of typical emitters are shown. It becomes apparent, that the field strength from the Ge emitter (33 V/cm) is significantly lower than the emission from a GaAs-based photoconductive antenna (240 V/cm) or from optical rectification from ZnTe (280 V/cm or 125 V/cm) or GaP (125 V/cm). However, the emission from the Ge-based emitter is much more broadband, free from phase-matching constraints, and does not require external bias. This is an important advantage for applications requiring a broad and gapless THz spectrum. Especially fiber lasers can benefit from this type of THz generation. They often output ultrashort pulses for fundamental and second harmonic beams. Another mechanism using two-color excitation for broadband THz generation is air plasma-based THz generation. However, this method requires high field strengths of the optical pulses to ionize air. This facilitates the need for laser amplifier system. Since fiber lasers are inexpensive compared to laser amplifier systems, quantum interference currents in germanium can enable a broader availability of THz experiments in the scientific community.

In summary, this publication shows that bulk Germanium can be used as an inexpensive source for broadband THz generation. It can enable more laboratories to establish

THz experiments by using a two-color excitation scheme using a small-footprint fiber laser. The high asymmetry of the emitted THz radiation as well as the higher bandwidth compared to established THz emitters allows for numerous applications.

5 Exciton interactions in semiconductors

5.1 Exciton formation

The availability of laser systems with ps and fs pulse durations opened the door to new realms of experiments. This lead to the field of ultrafast spectroscopy [32, 117, 118]. The interest in ultrafast phenomena remains unbroken up to this day [119]. It is not limited to physics but is also employed in biology [120] or chemistry [121, 122]. In condensed matter systems, one focus lies on the dynamics of charge-carriers in semiconductors. Here, the formation dynamics of excitons as fundamental quasi particles of optical excitations are one of the key areas. Starting in the 1990s, time-resolved photoluminescence emerged as the method of choice [17, 123–128]. Here, the luminescence arising at the $1s$ exciton resonance is monitored and subsequently analyzed for its temporal behavior. One major limitation of TRPL as an all-optical approach is the limitation to excitons with a center-of-mass momentum close to $K = 0$. Only these so-called "bright" excitons can recombine radiatively and subsequently be detected. This fact complicates the analysis of entire exciton populations [50, 129]. Therefore, results vary from around 20 ps [17, 123, 124, 126, 127] to 200 ps [129, 130] in GaAs MQW. An additional shortcoming become apparent when theoretical approaches using a stringent microscopic many-body theory revealed that the luminescence from the excitonic transition does not have to stem from an exciton population but can rather also be due to radiative recombinations of an electron–hole plasma [15]. These calculations were swiftly verified experimentally [131, 132]. Optical pump-terahertz probe spectroscopy provides an alternative and more direct approach. Since the intraexcitonic transitions in GaAs-based MQW are in the low meV range, THz can unambiguously reveal the existence of an exciton population [50, 133, 134]. THz does not suffer the drawbacks of TRPL since it can probe excitons independently of their center-of-mass momenta while also distinguishing between excitons and electron–hole plasmas [11, 135]. However, THz is not the holy grail of exciton detection if taken without a grain of salt. This becomes obvious when looking at the formation times reported in the literature. They range from a quasi-instantaneous formation of up to 40% exciton fraction [11, 14] to a formation on a timescale of a couple hundred ps [132, 136]. Paper III addresses this decade-long debate on exciton formation times and the associated methodologies. In this study, I resolve the prevailing discrepancies by employing a novel approach based on exciton ionization induced by intense THz radiation. The start of this investigation is by building the baseline with established methods. Since THz spectroscopy should be the main method of choice to investigate exciton dynamics, I start by employing the OPTP setup described in Section 3.3 to two comparable (Ga,In)As MWQ samples. Comparing samples makes the results of our findings more robust, since I can rule out any sample related quirks. Exciting the samples nonresonantly, i.e., above the single-particle band gap, results in the Drude-like response of unbound charge-carriers at low THz frequencies. This response is characteristic for an electron–hole plasma. This electron–hole plasma starts to get converted into an exciton population immediately, which can be observed by the rise of a lorentzian absorption line. Figure 5.1 shows this transition from unbound to bound electron–hole pairs. As mentioned earlier, TRPL has some methodological weaknesses. Nevertheless, for many

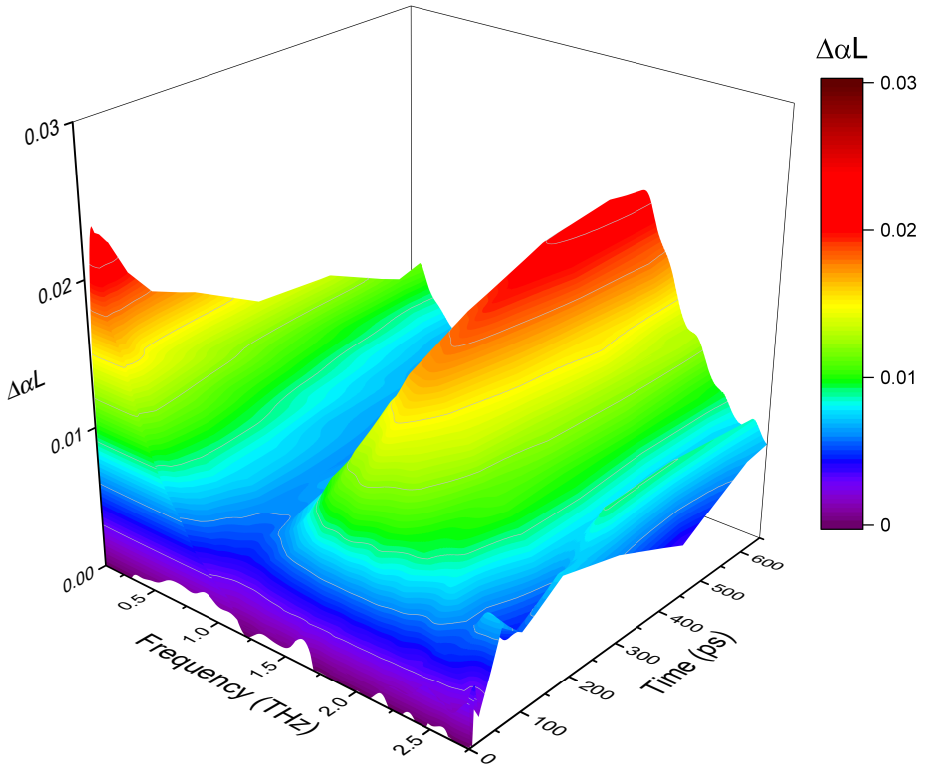

Figure 5.1: Surface plot of the pump-induced change of absorption $\Delta\alpha L$ for a photon density of $4 \cdot 10^{12}\,\mathrm{cm}^{-2}$. The optical excitation pulse is detuned 37 meV above the $1s$ exciton resonance and has a bandwidth of 2.5 meV. At low frequencies, the characteristic Drude-like response of an electron–hole plasma emerges almost instantly after photoexcitation. In contrast, the Lorentzian response of the intraexcitonic $1s$–$2p$ transition at around 1.5 THz starts to build up later while taking 600 ps to reach it's maximum.

it remains the method of choice for investigating exciton dynamics [137–139]. For completeness, I chose to employ TRPL and compare it side by side with THz spectroscopy. The TRPL data shows a quasi-instantaneous luminescence directly after nonresonant excitation at the energy of the $1s$ exciton resonance. This luminescence is commonly attributed to the existence of a finite $1s$ exciton population. However, as already reported in the literature, this conclusion is not necessarily correct [15, 131]. Indeed, the dynamics of the photoluminescence better matches the dynamics of charge-carrier decay obtained from THz spectroscopy (see Fig. 3 c) from Paper III). This comparison shows clearly that the PL dynamics mainly reflect the radiative recombinations of the entire carrier ensemble while THz spectroscopy distinguishes between Coulomb-bound and unbound electron–hole pairs. This shows the advantages of THz spectroscopy once more.
However, THz spectroscopy is not without flaws when investigating quasiparticle dynamics. One major issue arises in the high-density regime. Here, the application of the Drude-Lorentz model gets obscured by the broadening of the intraexcitonic resonance. As shown in Figure 5.2, similar fits can lead to drastically different exciton densities. This insight is nothing new, albeit not really resolved in the literature. In 2009, T. Suzuki and R. Shimano stated, that for high excitation densities they could explain the emergence of an offset in the absorption by a broad excitonic resonance [134]. This broad exciton resonance can lead to the assumption of a quasi-instantaneous exciton formation

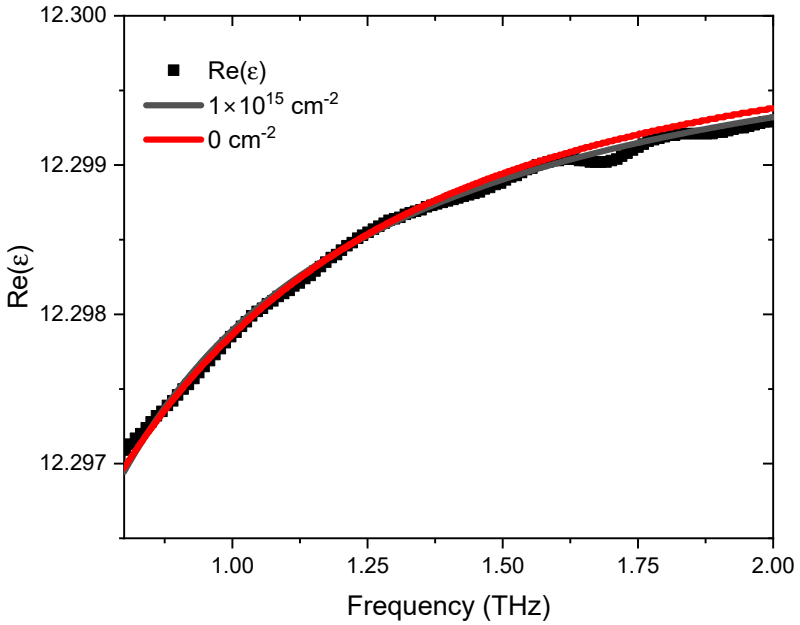

Figure 5.2: Comparison of high and zero exciton density for an excitation density of $1.08 \cdot {}^{\text{photons}}/_{\text{cm}^2}$. It becomes clear, that one has to be cautious when applying a Drude-Lorentz model to extract exciton densities. The fits look rather similar, although they have many orders of magnitude of exciton density between them. This shows, why the application of the Drude-Lorentz model to extract exciton densities fails at higher densities.

since the formation times decrease with increasing excitation density. This observation is in rather good agreement with previous experiments on GaAs MQW samples [11, 14]. There, they report up to 40% exciton fraction right after the excitation of their sample. A value, I can only achieve for the highest excitation conditions in my experimental setup. For lower excitation densities, it can take up to 30 ps to achieve similar values. Although THz spectroscopy can distinguish between bound and unbound electron–hole pairs, this ability is not universal. To achieve better separation of different quasi-particle contributions, one would need the isolate the individual responses. In the experiment present, I only have two contributions, one from the excitons and one from the electron–hole plasma. If one were able to switch off one of these contributions, one could extract the pure contribution of the other species. Switching off the response of the electron–hole plasma is not possible. However, this is not the case for the excitonic response. Since excitons possess a finite binding energy, they can be ionized by strong enough THz fields [140–142].

This leads to the new methodology developed for this publication. I employed two different field strengths for the probing THz pulse. The weaker of the two pulses is a true probing pulse as it does not alter the samples response and it is within the linear regime. The stronger THz pulse however, is strong enough to completely ionize the finite exciton population present in the sample, leaving only an unbound electron–hole plasma. Subtracting the now obtained pure plasma response from the total response isolates the excitonic response. Having now isolated the pure excitonic contributions,

one can obtain the oscillator strength of the intraexcitonic transition by integrating over the corresponding spectral region. This then gets plotted against the pump probe delay and subsequently fitted by a triexponential fit. Now a different picture gets painted for the exciton formation dynamics. While it still takes three distinct times to model the exciton formation dynamics, the density dependence is not present anymore for the density regime investigated here. For higher densities approaching the Mott density, a density dependence is to be expected [135]. Surprisingly, in the density regime under investigation, no acceleration of exciton formation can be observed when the excitation density is increased. The formation times acquired with the new differential method closely match those obtained with conventional OPTP spectroscopy in the low density regime. This implies the existence of an intermediate density regime as investigated here where the exciton formation is largely independent of excitation density. For low excitation densities exciton formation is governed by the lack of carrier-carrier and carrier-phonon scattering [135]. On the other hand, the exciton population approaches the Mott density for high excitation densities, suppressing additional exciton formation [45, 134, 143]. The existence of two distinct formation times raises the question of the individual formation mechanisms involved. Previously, the literature discussed the involvement of phonons in the exciton formation dynamics intensively with theoretical and experimental methods alike [16, 133, 144–147]. Here, the interaction of acoustic phonons and the incoherent electron–hole plasma leads to the formation of an incoherent $1s$ exciton population. Their findings explain the slower, roughly 250 ps formation time. Similarly, the influence of LO-phonons on the formation of excitons has been discussed [144, 145, 148–150]. The interaction with LO-phonons could theoretically explain the fast formation time. However, no influence of the excitation excess energy on the fast formation time can be observed. Additionally, for excitations close to the band gap, i.e., with excess energy smaller than the LO-phonon energy, a contribution of LO-phonons is suppressed. Nevertheless, the fast formation time holds true for all excitation conditions investigated for this publication. Therefore, another explanation is needed. One possible reason for the fast formation time can be a geminate-like exciton formation. Here, the initial Coulomb correlation between the photo-excited electron–hole pairs is preserved. This leads to the coexistence of correlated and uncorrelated charge-carriers [144, 151]. Two distinct formation processes take place within this mixture. The correlated electron–hole pairs can form excitons on a picosecond timescale due to Coulomb-mediated scattering, while the uncorrelated electron–hole pairs still need to build up correlations following the slower phonon-assisted process. This explains the two distinct timescales observed in the experiment. The same explanation applies to indirect semiconductors, where no fast formation time is observed [134, 135]. In these systems intervalley phonon scattering destroys the initial Coulomb-correlation leading to the phonon-assisted exciton formation remaining the only formation channel as the geminate process needs an intact Coulomb-correlation. In summary, the method developed for this publication allows to resolve the ambiguity of exciton formation times reported in the literature. It explains, why the literature shows different formation times for excitons formation. This can be traced back to two distinct formation processes which can be obscured by traditional experimental approaches. The newly-developed method is not limited to exciton formation dynamics in (Ga,In)As quantum wells but applicable to a wide variety of material systems as well as quasi-particle species.

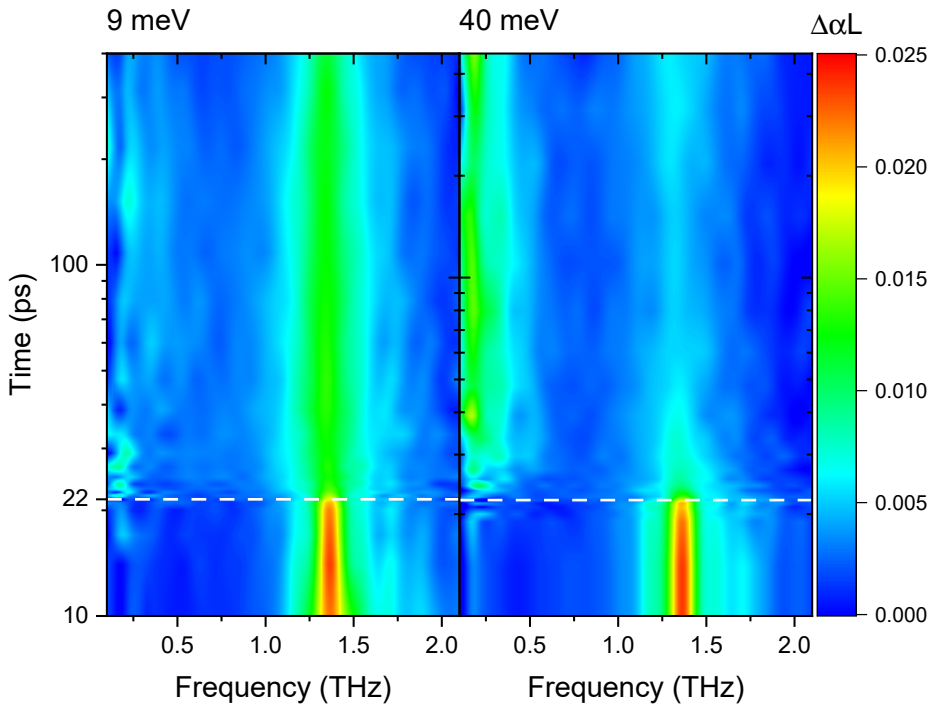

Figure 5.3: Excitation-induced change of the absorption for 9 meV and 40 meV excess energy of the electron–hole plasma. The charge-carrier density is kept similar. The white dashed line a 22 ps denotes the arrival of the second optical pulse, injecting the additional electron–hole plasma. Before the second optical pulse impinges on the sample, both images show a clear intraexcitonic $1s$–$2p$ transition at 1.36 THz. However, after the second optical pulse injects additional charge carriers, the response changes. For an excess energy of 9 meV, the intraexcitonic resonance broadens but remains largely intact, whereas at 40 meV the intraexcitonic resonance is strongly suppressed.

5.2 Exciton-electron scattering

In the previous sections I dealt with ways of how to generate excitons in semiconductors. As it becomes clear from non-resonant exciton formation in Paper III there is a time, when bound and unbound excitons coexist. As such, they can interact. One of the most basics forms of interaction is scattering. Said interaction can be found in many disciplines of physics. Ranging from the vast distances in astrophysics, over classical mechanics and nuclear physics to quantum mechanics and solid-state physics. In the latter, scattering is used to describe the many-body interactions in condensed matter systems, i.e., semiconductors. Given the pivotal role that excitons play in semiconductors, it is consequent to investigate their scattering behavior. First theoretical descriptions of excitonic-electron scattering were started in the 1970s [152, 153]. Subsequently, experimentalists caught on and over the next decades plenty of publications bore witness to the increasing research interest in exciton-electron scattering. These were mainly conducted using all-optical experiments like PL [154] or FWM [155–157]. Although these experiments provide information on the total scattering rate, they are unable to distinguish between elastic and inelastic scattering events. For this distinction, an experiment would need to provide a measure of the size of the exciton population. Although possible, it is quite hard to access this data with all-optical means [131]. Herein lies the intrinsic advantage of THz

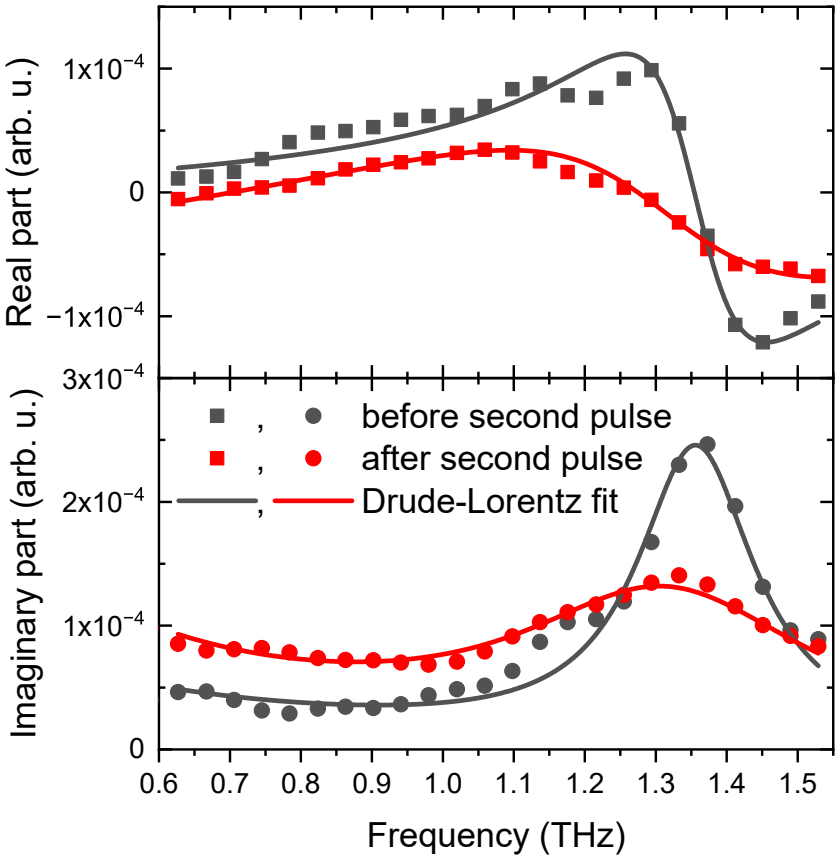

Figure 5.4: Drude–Lorentz fits to experimental data before and after excitation by a second optical pulse. The real (top) and imaginary (bottom) parts of the dielectric function are shown. Both components are fitted simultaneously to improve robustness. Before the second pulse arrives at the sample, the sample's response is dominated by the Lorentzian absorption feature of a very narrow intraexcitonic $1s$–$2p$ transition. No unbound electron–hole plasma can be observed. After the second pulse excites additional charge-carries, the intraexcitonic resonance broadens and decreases while also the Drude-like response of an electron–hole plasma emerges at lower frequencies.

spectroscopy. Since THz spectroscopy probes the intraexcitonic transitions of all excitons regardless of their center of mass momentum it enables direct conclusions about the size of the exciton population [11, 50]. This lead to the development of an OPTP setup, where to optical pulses with a fixed temporal delay inject excitons and an electron–hole plasma to monitor the change of the intraexcitonic absorption of THz radiation [158]. In this proof-of-concept a first optical pulse above the fundamental bandgap of Germanium excited an electron–hole plasma, subsequently converts into an incoherent exciton population. A second optical pulse is delayed by 6.7 ns to ensure that the conversion converted nearly all unbound to bound excitons. The second optical pulse then injects an additional electron–hole plasma. A THz pulse monitors the intraexcitonic $1s$–$2p$ transition of the excitons generated by the first optical pulse. Thus, this allows to probe the decay of the incoherent exciton population due to scattering with the unbound electron–hole plasma. I use this method to investigate the elastic and inelastic contributions for a (Ga,In)As MQW sample (DBR13). The main advantage of this particular sample is its exceptionally narrow linewidth of 0.2 THz (0.8 meV) for the intraexcitonic $1s$–$2p$ transition.

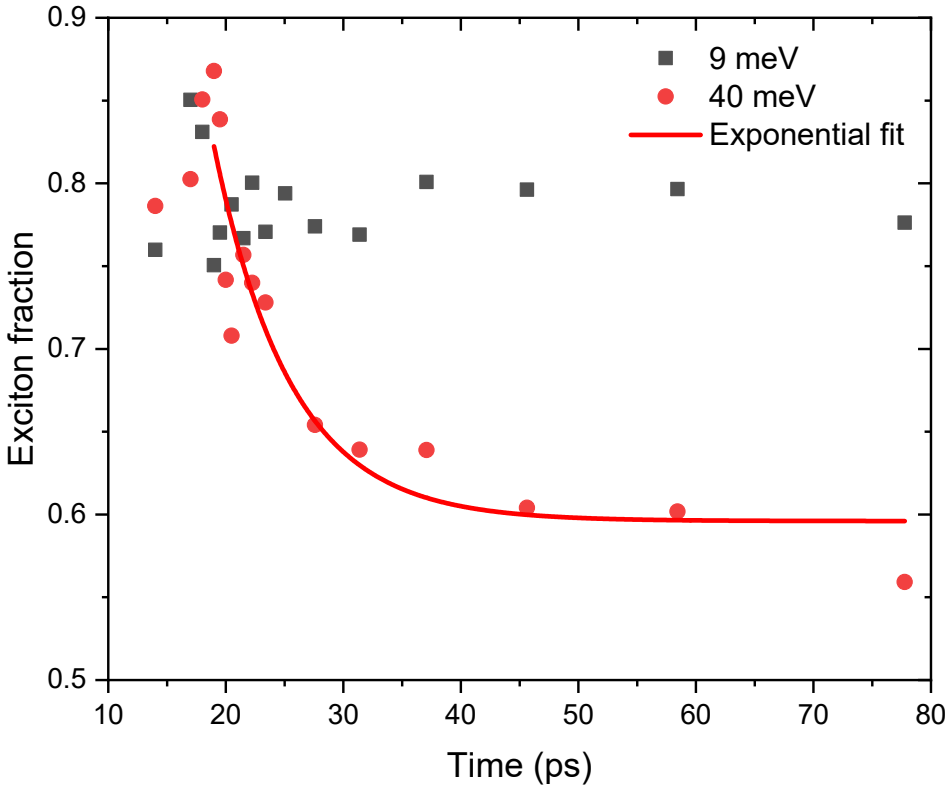

Figure 5.5: Exciton fractions extracted by the Drude-Lorentz model from the data shown in Figure 5.3. For 9 meV excess energy (gray squares), the exciton fraction remains constant at 0.8 apart from some noise during the second optical pulse. For 40 meV excess energy (red circles) the exciton fraction decreases from 0.8 to 0.6 for the given photon density. The exponential fit from which the inelastic scattering time is extracted is shown as a solid red line.

Induced changes in linewidth are, thus, much easier to resolve. Additionally, it allows me to resonantly excite an exciton population without having to delay the pulses by a couple of nanoseconds but merely tens of picoseconds, since this sample is a direct semiconductor. Furthermore, I cannot only change the charge-carrier density of the electron–hole plasma but also the excess energy with regard to the $1s$ exciton resonance. The first optical pulse is tuned by the pulse shaper, while the second optical pulse is tuned by a pair of short- and longpass filters. This allows to investigate the influence of excess energy on the scattering contributions. One main question is whether the interaction strength between excitons and electrons changes depending on the kinetic energy of the electrons. The setup for this publication is described in Section 3.3. The total scattering of excitons and electrons can be divided into two contributions—elastic and inelastic. In elastic scattering events, exciton and electron exchange kinetic energy and the exciton remains intact [159]. In this case, the exciton population does not decrease in size, i.e., the exciton density remains roughly the same, but due to the dephasing of an exciton state, the intraexcitonic resonance broadens. Here, the main advantage of THz spectroscopy comes into play. Since THz spectroscopy probes the intraexcitonic transitions regardless of the exciton's center of mass momentum, this broadening can be observed. In contrast, changing the exciton's momentum in an all-optical experiment would lead to a pseudo inelastic contribution since optical methods only detect excitons with a center of mass

momentum close to K=0. In contrast to elastic scattering events, inelastic scattering dissociates the exciton population leading to a decrease in exciton density [159]. First, I want to compare the response for 9 meV and 40 meV excess energy qualitatively. As seen in Figure 5.3, I observe a sharp resonance at around 1.36 THz associated with an intraexcitonic $1s$–$2p$ transition for both excess energies. The second optical pulse impinges on the sample after ~ 22 ps. This is marked by a white dashed line. After this, the responses for the individual excess energies changes drastically. The intraexcitonic resonance broadens but mainly remains intact for an excess energy of 9 meV. This broadening bears witness to the overall scattering between excitons and electrons. In contrast, for 40 meV excess energy the resonance broadens but also decreases significantly. In addition, a Drude-like response for frequencies below 0.5 THz arises. This is characteristic for an unbound electron–hole plasma [89]. This qualitative difference already shows, that the excess energy of the electron–hole plasma plays a crucial role to determine the ratio of elastic and inelastic scattering processes. While a qualitative picture is a good step to first get an overview, the quantitative evaluation and description is the ultimate goal. To analyze the behavior of the exciton population, I once more turn to the Drude-Lorentz model (cf. Section 2.3). Fitting this model simultaneously to the real and imaginary dielectric function obtained from the OPTP measurements allows us to rigorously extract the key parameters for determining elastic and inelastic scattering contributions. In this case, the main focus lies on the exciton density n_x and the homogeneous linewidth Δ_{hom}. The change of linewidth is directly proportional to the total scattering events [155, 156, 160, 161] while the change in exciton density corresponds to the dissipation of excitons, in this case due to inelastic scattering. However, inelastic scattering itself also leads to a broadening of the excitonic linewidth. It is important to emphasize at this point, that I always measure the intraexcitonic $1s$–$2p$ transition, meaning that both scattering of $1s$ as well as $2p$ states change the linewidth of the transition. As such, the experiment does not resolve the scattering contributions of the individual states but is instead sensitive to both simultaneously. It remains a matter of debate whether the $1s$ and $2p$ states scatter differently due to their difference in spatial extent [35]. This means, I cannot assign scattering events to an individual state and need to make an assumption. Going forward, I assume that $1s$ and $2p$ states are influenced equally. This in turn allows to deduce that the homogeneous broadening of the $1s$ exciton state Δ_{hom} can be expressed as:

$$\Delta_{\mathrm{hom}} = {}^{\Delta_{\mathrm{intra}}}\!/\!_{\sqrt{2}}. \tag{5.1}$$

Correcting for this superposition allows to extract the excitation-induced intraexcitonic line broadening Δ_{intra} which is a measurement for the total scattering. It is determined by comparing the intraexcitonic linewidth before $\Gamma_{\mathrm{hom}}(0)$ and after $\Gamma_{\mathrm{hom}}(n)$ the second optical pulse injects additional charge-carriers as scattering partners :

$$\Delta_{\mathrm{intra}} = \Gamma_{\mathrm{hom}}(n) - \Gamma_{\mathrm{hom}}(0). \tag{5.2}$$

Here, n denotes the density of additional charge-carriers. Naturally, one would analyze the homogeneous linewidth broadening depending on the amount of additional charge-carriers. Following this intuitive thought, I find that the total scattering is linearly proportional to the charge-carrier density. This is what is to be expected from literature [162] for the low-density regime. While elastic contributions to the total scattering are not directly accessible, their inelastic counterparts can readily be extracted. To do so, I fit an exponential function to the transient evolution of the exciton density. As already mentioned before, the change in exciton density directly reflects the number of excitons

persisting after the introduction of additional charge-carriers. Thus, the exponential fit directly extracts the excitonic decay time τ_1. This decay time in turn contributes to the change of homogeneous linewidth via [155]

$$\Delta_{\mathrm{hom}} = 2/\tau_1. \tag{5.3}$$

The elastic scattering can subsequently extracted by

$$\Delta_{\mathrm{hom,el}} = \Delta_{\mathrm{hom,tot}} - \Delta_{\mathrm{hom,inel}}. \tag{5.4}$$

In the low density regimes the excitation induced linewidth change can be expressed as [162]

$$\Delta_{\mathrm{hom}} = \gamma a_{\mathrm{B}}^2 E_{\mathrm{B}} n, \tag{5.5}$$

where a_{B} is the exciton Bohr radius, E_{B} the exciton binding energy, n the charge-carrier density, and γ is a dimensionless parameter representing the interaction strength of excitons with the free electron–hole plasma. The dimensionless parameter γ is a good measure how efficiently excitons scatter with additional charge-carriers. By defining

$$m := \Delta_{\mathrm{hom}}/n \tag{5.6}$$

one can express γ as follows

$$\gamma = \frac{m}{a_{\mathrm{B}}^2 E_{\mathrm{B}}}. \tag{5.7}$$

m can be directly derived from the slope of the excitation induced linewidth change. The missing two parameters are a_{B} and E_{B}. E_{B} can be derived from multiplying the $1s$–$2p$ transition by $9/8$ [163]. The exciton Bohr radius can derived from similar samples as the product of $E_{\mathrm{B}} \cdot a_{\mathrm{B}}$ is constant for a given material system [136, 164]. Comparing γ for both excess energies reveals an intriguing feature. Both excess energies show similar total scattering efficiencies with γ amounting to 8.8 and 9.34 for 9 meV and 40 meV respectively. They are within the range of values reported in the literature for FWM experiments on similar structures [155, 157]. As mentioned previously, the change in exciton fraction can be converted into an excitation induced linewidth change and, thus, subsequently a scattering parameter γ_{in} for the inelastic scattering efficiency can be derived. For 40 meV excess energy, a scattering parameter amounts to ~ 2.54. However, for 9 meV excess energy, no inelastic scattering parameter can be derived as the exciton fraction does not change significantly when the second optical pulse injects an additional electron–hole plasma (cf. Figure 5.5). The important conclusion at this point is, that the overall scattering efficiency is independent of charge-carrier density as well as independent of excess energy for excess energies not exceeding 40 meV. In contrast, the individual contributions of elastic and inelastic scattering processes solely depend on the excess energy. Increasing the excess energy leads to an increase in inelastic scattering while elastic scattering diminishes. This behavior can be understood as an analogy of classical mechanics in the quantum realm. In classical mechanics, elastic and inelastic scattering processes can be illustrated by car accidents. Here, the excess energy comes in the form of kinetic energy, similarly to the electron–hole plasma where excess energy is converted to additional momentum. For reasonably small velocities, car crashes result in elastic deformation. Increasing the speed of the cars leads to an increase in plastic deformation. The same holds true for excitons scattering with and electron–hole plasma. Increasing the excess energy of the electron–hole plasma appears to enhance exciton dissociation rather than momentum transfer, while elastic scattering remains dominant. However,

both excess energies chosen in the experiment are well above the exciton binding energy of 6.33 meV. Theoretically, even the lowest excess energy of 9 meV should, thus, be able to dissociate some of the exciton population. This apparent contradiction gets lifted, if one considers the quantum mechanic nature of the many-body interactions taking place. Here, the transition between different states can be expressed by Fermi's Golden Rule. Simply put, it states that in order to transition between two states, an initial state needs to be populated while the final state is unoccupied. In the case of inelastic scattering, both scattering partners occupy their respective initial states. However, if electrons (or holes) were to transfer 6.33 meV of excess energy to dissociate excitons, they would have 2.67 meV left with respect to the $1s$ exciton resonance. The linear absorption spectrum of the sample shows that no state is available at this energy, rendering the transition energetically forbidden. Therefore, this transition cannot occur, and excitons cannot be dissociated by the electron–hole plasma. In summary, Paper I establishes a powerful framework for probing quasiparticle interactions. By combining two optical pump pulses with a time-resolved THz probe, it introduces a versatile experimental scheme for accessing exciton dynamics and, at the same time, resolves the longstanding question of how excitons interact with an electron–hole plasma. Moreover, the results highlight the decisive role of excess energy in governing quasiparticle scattering processes.

5.3 Screening

In the previous section, I dealt with the scattering of excitons with an electron–hole plasma. Analyzing the broadening of the intraexcitonic resonance allowed to extract the total scattering of excitons with additional charge-carriers while the decrease in exciton density allowed to extract the inelastic scattering parameter. However, one can also analyze the shift of the intraexcitonic transition's resonance frequency. This is a direct measure of screening of the exciton binding. Typically, this shift has been investigated in all-optical experiments [165]. However, these experiments are susceptible to energy shifts of the exciton transition due to band edge renormalization [90, 91]. In contrast, THz spectroscopy enables a direct measurement of the intraexcitonic $1s$–$2p$ transition, which directly correlates with the exciton binding energy [11, 12, 133]. Therefore, terahertz spectroscopy is a crucial tool for the analysis of spectral shifts of the intraexcitonic resonance, which is a measure for the screening of said resonance [35, 166]. Previous works focused on the screening directly after the excitation of an electron–hole plasma [167] or the exciton screening in the high-density regime [35]. More recently, the screening of excitons in TMDCs was investigated using TRPL measurements in conjunction with microscopic theory to disentangle different contributions to the excitonic screening [168]. However, these works employ a single optical pulse for excitation. The main advantage of my method is the ability to monitor the exciton population in a pool of independently injected charge-carriers. As the first optical pump pulse is modulated, the additional charge-carriers generated by the second pump pulse are not directly detected in the THz response, since they are introduced at a different modulation frequency and are therefore filtered out in the detection scheme. Instead, I see the originally generated excitons in an environment of free electrons and holes and observe how this affects their intraexcitonic transition energy with temporal resolution. Figure 5.6 shows the normalized differential THz absorption for additional electron–hole plasmas with 9 meV and 40 meV respectively. Once the second optical pulse injects additional charge-carriers, the intraexcitonic $1s$–$2p$ transition broadens and shifts towards lower frequencies. The resonance frequency of the intraexcitonic transition is marked by the white dashed line. In a 2D case, this

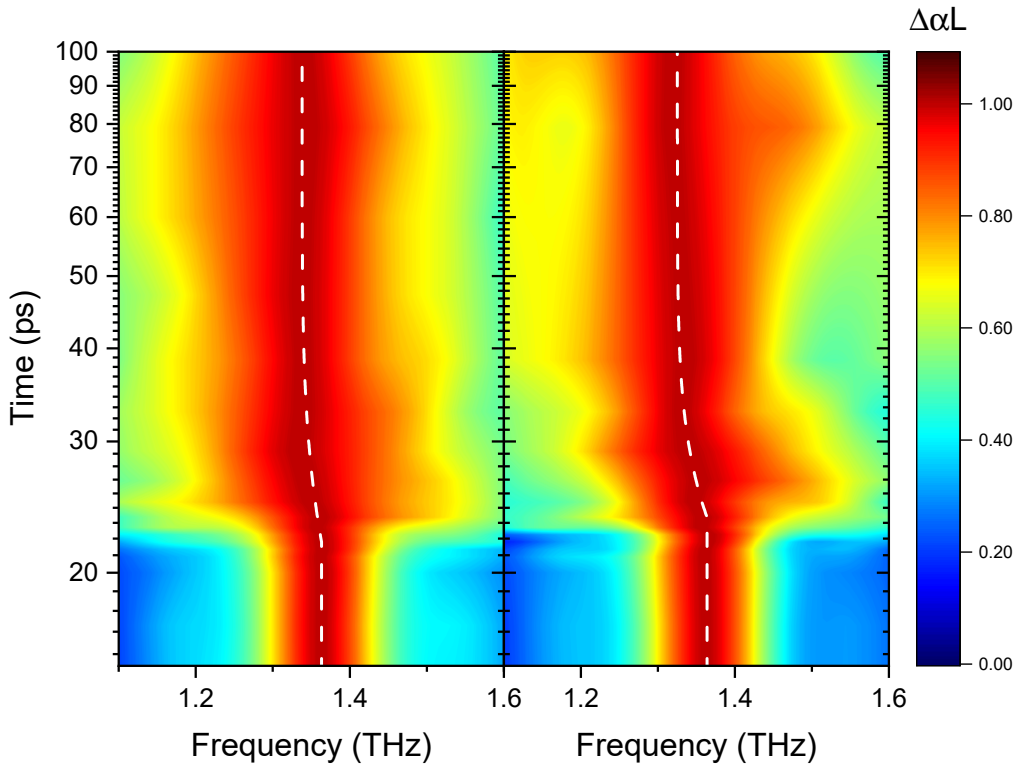

Figure 5.6: Normalized THz absorption for 9 meV excess energy (left) and 40 meV excess energy (right). Charge-carrier densities are kept similar in both cases. The second optical pulse injecting the electron–hole plasma arrives at 22 ps. The maximum of the THz absorption is marked with a dashed white line. After the additional electron–hole plasma gets injected the intraexcitonic $1s$–$2p$ transition shifts to lower frequencies which is a direct sign of screening. The screening time gets extracted by fitting an exponential function to the resonance frequency

resonance frequency directly correlates with the exciton binding energy by a factor of 9/8 [163]. Therefore, the shift in resonance frequency is a direct observation of the exciton binding energy getting screened by the additional charge-carriers. Figure 5.7 a) displays the shift of the intraexcitonic resonance energy as a function of the charge-carrier density injected by the second optical pulse. As more unbound charge-carriers get injected into the sample, the intraexcitonic resonance energy shifts to lower energies, i.e., the Coulomb interaction between electron and hole is screened by the injected electron–hole plasma [166]. Here, an almost linear increase of the resonance energy shift with increasing carrier density is observed, demonstrating that the Coulomb interaction is better screened as the density of the electron–hole plasma increases. This is in conjunction with previous OPTP experiments only employing a single optical pump pulse [35]. Furthermore, a higher excess energy results in a more pronounced shift of the intraexcitonic resonance. Evidently, more excess energy of the free charge-carriers facilitates more effective screening of the Coulomb interaction. Additionally, in this case, some excitons break down following inelastic scattering, thereby more free charge carries contribute to the screening than originally injected by the second optical pulse. To extract these additional charge-carriers, one needs to turn back to the scattering described in Section 5.2. The additional charge-carrier density is obtained from the difference between the initial ex-

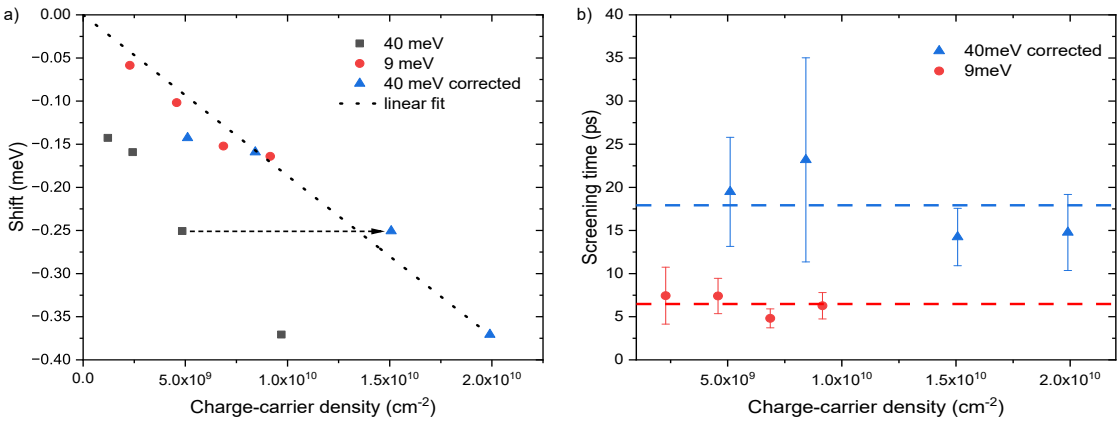

Figure 5.7: a) Shift of the $1s$–$2p$ resonance energy. In all cases, the resonance energy shifts towards lower binding energies. More excess energy enforces a stronger shift. b) Screening times derived from an exponential fit on the resonance energy. The mean screening times are marked by the horizontal lines. The buildup of screening remains constant for different charge-carrier densities and depends solely on the excess energy.

citon density and the exciton density measured after excitation with the second optical pulse, which generates the electron–hole plasma. However, the temporal evolution of screening has yet to be experimentally investigated. Previous studies have focused on PL measurements of the $1s$ resonance and have relied heavily on theoretical interpretations [168]. In the present experimental approach, the time-dependent screening of the intraexcitonic resonance induced by excess free carriers is analyzed by fitting an exponential function to the transient shift of the $1s$–$2p$ transition energy. Figure 5.7 b) displays the screening times derived from these exponential fits. The buildup of screening takes around 6 ps for 9 meV excess energy and about 18 ps for 40 meV and remains constant over the range of charge-carrier density investigated. The difference in screening times can be attributed to the additional charge-carriers generated by the destruction of excitons. These now unbound charge-carriers in turn need additional time to screen the exciton dipole moment.

5.4 Light-field driven exciton states

The nonlinear optical response of semiconductors under excitations detuned below the fundamental transition has attracted considerable attention, primarily due to the manifestation of the optical Stark effect [169–173]. This effect induces a shift of the excitonic resonance, which can appear either as a blue- or redshift depending on the polarization configuration of the pump and probe pulses [174]. Beyond its fundamental relevance, the optical Stark effect provides a versatile platform for technological applications such as electro-optic modulators [175], optical switches [176, 177], and optoelectronic logic devices [178]. In recent years, the concept of manipulating condensed matter systems using intense light fields has given rise to new paradigms in solid-state physics [179–181]. The central idea is to engineer transient, non-equilibrium states in materials through the use of precisely tailored electromagnetic fields. In many cases, these light fields act as time-periodic drivers of the quantum system, resulting in the formation of characteristic (quasi)stationary states known as Floquet states [182]. Such states often correspond

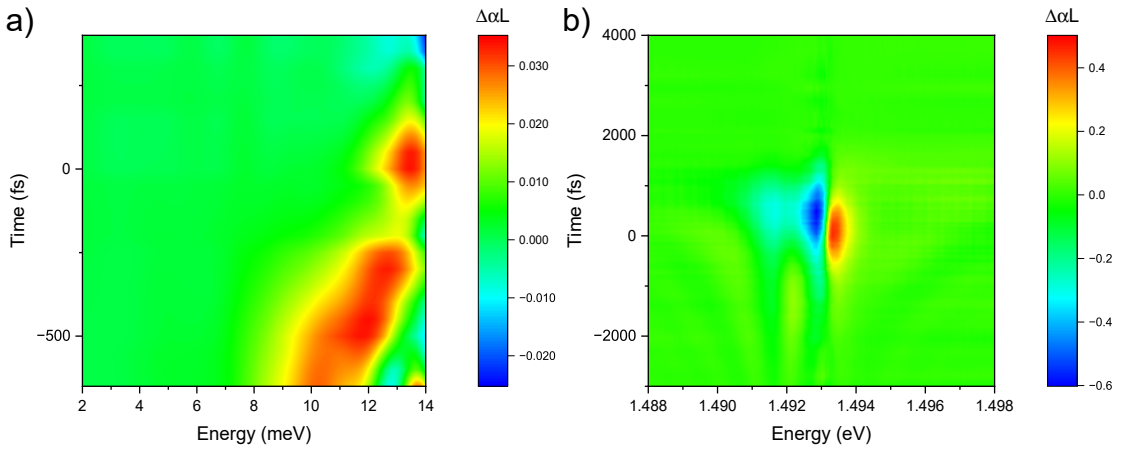

Figure 5.8: Comparison of a) the excitation-induced THz absorption and b) the corresponding optical pump-optical probe data for identical optical excitation conditions. Here, the optical pump pulse was detuned 3.6 meV below the 1s exciton resonance. The optical pump and probe pulses are polarized collinearly. In both probing ranges, the resonance experiences a blue-shift.

to photon-dressed quasiparticles and lead to the emergence of distinctive features in the electronic structure. One of the most prominent examples of this phenomenon is the formation of Floquet–Bloch bands [183–186]. Here, a time-periodic electromagnetic potential—typically generated by a coherent laser field—modifies the motion of Bloch electrons, effectively replicating their original band structure into additional Floquet sidebands [186]. The energies of these sidebands are shifted by integer multiples of the photon energy of the driving field. The overarching goal of this research direction is to dynamically impart tailored functionalities to materials and, more intriguingly, to uncover emergent quantum phenomena arising from light–matter hybridization [187, 188]. Building upon these developments, I detune the optical excitation pulse in an OPTP experiment below the 1s exciton resonance. This configuration is similar to experiments to investigate the ac-Stark shift in OPOP experiments [165, 189]. Whereas OPOP experiments primarily probe energy shifts of excitonic resonances, OPTP measurements access the occupation of these states via intraexcitonic transitions. In addition, OPTP is sensitive to the coherent polarization of the 1s exciton. Subsequently, one would expect a signal in OPOP measurements but no signal in OPTP experiments, since an optical pulse detuned below the resonance does not lead to an exciton population. Importantly, one has to be careful when investigating coherent phenomena during temporal overlap of optical pump and THz probe pulses. As discussed in Section 3.3, to obtain the physical pump-probe time in OPTP spectroscopy, the measured data from our setup needs to be interpolated and then the diagonal of the 2D spectra drawn. In Figure 5.8 the results of OPTP and OPOP are compared side-by-side. In the OPOP measurement depicted in Figure 5.8 b), the characteristic optical Stark shift emerges for an optical pump pulse detuned by 3.6 meV below the 1s exciton resonance. Here, one can see a blueshift of the 1s exciton resonance for a collinear configuration. Intriguingly, the OPTP data in Figure 5.8 a) also shows a clear excitation-induced absorption feature during temporal overlap of optical pump and THz probe. This induced absorption is shifted towards higher energies compared to the intraexcitonic 1s–2p transition arising after resonant excitation which lies around 6 meV. In contrast to the pronounced energy shift observed in OPOP experiments, the OPTP data suggest that the intraexcitonic resonance itself

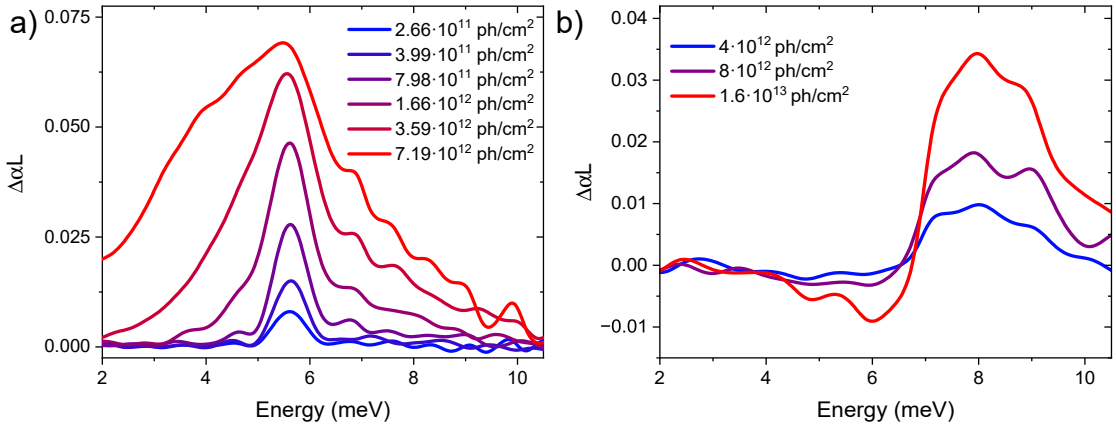

Figure 5.9: Pump density dependence for a pump pulse tuned a) resonantly to and b) 3.6 meV below the 1s exciton resonance. There is a regime for both pump configurations where the sample's response in the THz range depends linearly on the excitation density. However, for resonant excitation one can pump the sample strong enough to approach the exciton–Mott transition. This can be seen by the broadening of the intraexcitonic 1s–2p transition as well as the emergence of a Drude-like response at low energies.

does not shift. Rather, a transition-like feature emerges at higher energies. Compared to resonant excitation, this may be interpreted as an apparent shift. However, this transition is only present during temporal overlap of pump and probe and does not result in the occupation of a finite exciton population. This conclusion can be drawn from the fact that there is no signal in either the OPOP or the OPTP data for greater time delays. To further manifest the hypothesis that this induced absorption feature is of excitonic nature, I compare it to resonantly excited 1s excitons. Therefore, I tune the optical pulse so that the 1s exciton is resonantly excited resulting in the formation of a 1s exciton population. The time delay between the optical excitation pulse and the THz probing pulse is set to 8 ps. In Figure 5.9 a) the photon density of the resonant excitation pulse is varied over 1.5 orders of magnitude. For the three lowest photon densities the differential absorption of the 1s–2p transition scales linearly with excitation density. Increasing the photon density above $7.98{\cdot}10^{11}$ photons/cm^2 results in a broadening of the transition. At the highest photon density of $7.19 \cdot 10^{12}$ photons/cm^2 first signs of a Drude-like signature typically associated with an electron–hole plasma appear [89]. This behavior is common in semiconductors when approaching the Mott density [35, 142]. I tune the optical pulse 3.6 meV below the 1s exciton resonance while probing the intraexcitonic 1s–2p transition. In this configuration, the differential absorption signature is only observed when the optical excitation and the THz probing pulses overlap in time. Therefore, I set the time delay between the optical pump pulse and the EOS gate pulse to 1 ps to investigate the dependence on the pump fluence. Similar to resonant excitation conditions, an increase in pump fluence leads to a linear increase of the intraexcitonic resonance. In addition, the spectral shape of the THz response does not change with the excitation density. These are clear indications that the observed phenomenon is of linear dependence on the excitation pulse, ruling out nonlinear processes like for example a two-photon absorption process involving one optical and one THz photon. It has to be noted, that the pump density for the nonresonantly driven signal is already much higher than for the resonantly driven excitons. This is due to the fact that it gets more an more inefficient, the more the optical pulse is detuned from the resonance. Additionally, one can see a gain-like fea-

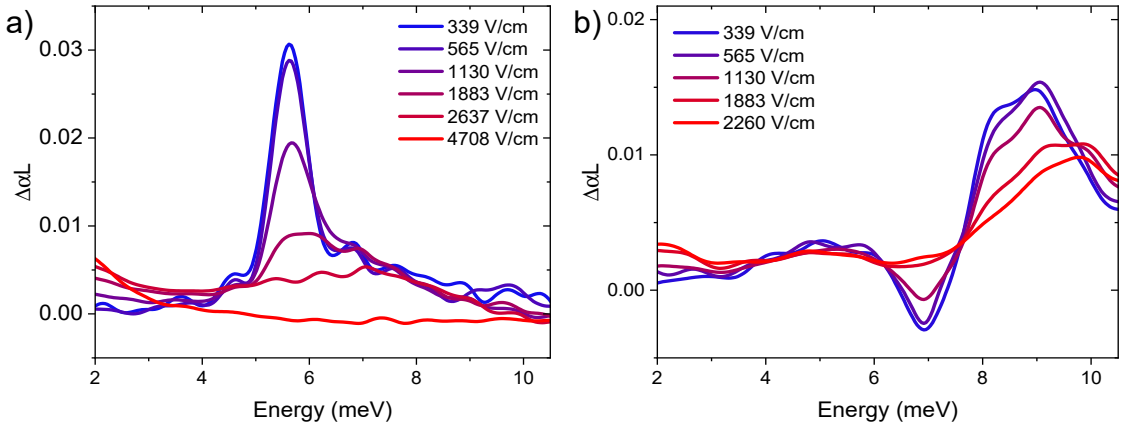

Figure 5.10: Field strength dependence for the pump-induced change of absorption for a) resonant pump conditions and b) detuning of the pump below the 1s exciton resonance. Under resonant excitation the characteristic feature of a 1s–2p transition can be observed for low field strengths. Increasing the field strength ultimately leads to a broadening of the intraexcitonic resonance and the rise of a Drude-like response at low energies, bearing witness to the ionization of the exciton population. For an optical pulse detuned by 3.3 meV below the 1s resonance the pump-induced absorption shows a similar behavior.

ture, i.e., negative absorption at the resonant intraexcitonic 1s–2p transition at around 6 meV. This feature must not be considered a real physical amplification of THz radiation but more an artifact due to the 1D nature of the measurement data. Since I measured only for one fixed delay, there is no possibility to interpolate and take a diagonal from a 2D data set. Here it becomes obvious why one must carefully process the extracted timetraces for effects during temporal overlap. To verify that the THz pulse is weak and can therefore be used as a probe pulse, I vary the THz field strength and monitor the intraexcitonic 1s–2p transition for resonant excitation of the 1s exciton resonance. Figure 5.10 a) shows the dependence of the intraexcitonic 1s–2p signal on various THz field strengths. At low field strengths, the differential absorption does not change and is independent of the THz field strength. Increasing the field strength further leads to a decrease and broadening of the intraexcitonic resonance. Additionally, a Drude response occurs at lower frequencies. This behavior is typical for the ionization of excitons due to high field strengths [140, 190]. To elucidate the origin of the newly observed signal, the dependence of the differential THz absorption on the THz field strength is systematically examined. Therefore, I tune the optical pulse 3.3 meV below the 1s exciton resonance. Under these excitation conditions and a time delay of 1 ps, I observe a resonance around 9 meV and a negative differential absorption at 7 meV. For low field strengths, the differential absorption remains unaffected by the field strength of the probing THz pulse as shown in Figure 5.10 b). This is exactly the same behavior that I observe under resonant excitation conditions cf. Figure 5.10 a). Only above a certain THz field strength is a broadening observed, which leads to a corresponding weakening of the resonances in the differential absorption. Notably, the effects of resonant and below-resonant optical excitation occur under comparable carrier densities and THz field strengths. This behavior can again be explained by exciton ionization induced by the THz field [140]. This leads to the conclusion that I create a 1s polarization at an energy below the 1s resonance. The field-strength dependence of the observed resonance in the differential

absorption therefore indicates a purely linear response. In contrast, in a nonlinear process such as two-photon absorption, the resonance peak in the differential absorption would be expected to increase with increasing THz field strength. The absence of nonlinear dependencies of the differential THz absorption on the optical photon density as well as on the THz field strength eliminates nonlinear effects as an explanation for the observed intraexcitonic resonance for optical excitation below resonance.

In summary, detuning the optical pump in an OPTP experiment below the lowest exciton resonance provides a novel route to probing the excitonic system. Remarkably, this pathway enables the generation of an excitonic polarization at an energy where no excitonic state is expected. Harnessing this mechanism may open a route toward THz gain, arising from the population of $2p$ states, which subsequently relax to $1s$ excitons while emitting THz radiation.

6 Summary and Outlook

Understanding the dynamics of quasiparticles in semiconductors is central to modern condensed matter physics and underpins a wide range of optoelectronic technologies. In particular, excitons—bound electron–hole pairs arising from Coulomb interactions—play a fundamental role in light–matter interaction and energy transport in semiconductor systems. THz spectroscopy provides a uniquely powerful probe of these quasiparticles, as THz radiation directly addresses their internal degrees of freedom and many-body interactions. At the same time, advances in THz generation techniques continue to expand the experimental capabilities available for investigating ultrafast carrier dynamics.

This thesis explores several aspects of THz radiation and semiconductor many-body physics by combining the development of broadband THz sources with spectroscopic investigations of excitons in semiconductor nanostructures. By integrating advances in THz generation with optical pump–THz probe spectroscopy, the presented work introduces new experimental approaches for probing quasiparticle dynamics and light–matter interactions in semiconductors.

Chapter 2 introduces the theoretical framework underlying this thesis. In particular, the semiconductor Bloch equations are presented as the central description of the microscopic dynamics of charge carriers and excitons. Furthermore, different approaches for modeling the THz conductivity of semiconductors are discussed, providing the basis for interpreting the spectroscopic signatures observed throughout this work.

The experimental techniques are described in Chapter 3. A particular focus lies on the coherent generation and detection of THz radiation, including electro-optic sampling for time-resolved detection. In addition, the principles and practical considerations of optical pump–THz probe spectroscopy are discussed, highlighting both the capabilities and limitations of THz spectroscopy for investigating ultrafast quasiparticle dynamics in semiconductor systems.

The experimental results are presented in Chapter 4 and Chapter 5. The first study, described in Chapter 4, demonstrates the broadband and gapless generation of THz radiation through quantum interference currents in bulk germanium. Using a two-color excitation scheme, transform-limited THz emission constrained by the optical pulse duration is achieved, reaching a bandwidth of nearly 8 THz. The emitted pulses exhibit a pronounced temporal asymmetry with a ratio of 3.34:1 and a full width at half maximum of 110 fs. These properties make the source particularly attractive for applications such as THz-driven scanning tunneling microscopy. Although the achievable field strengths are lower than those of conventional THz emitters, the generation scheme operates efficiently with low-power fiber lasers, enabling compact and accessible THz systems.

The formation dynamics of excitons in (Ga,In)As multiple quantum wells are investigated in Section 5.1. Prior to this work, significant discrepancies existed in the literature regarding the timescales of exciton formation following nonresonant excitation. These discrepancies were partly caused by the use of different experimental techniques probing different observables. By comparing time-resolved photoluminescence with optical pump–THz probe spectroscopy, it is shown that the TRPL signal closely follows the dynamics of the underlying electron–hole plasma rather than directly reflecting the exciton population. This finding highlights the considerable challenges involved in disentangling

excitonic and plasma contributions in luminescence measurements.
While THz spectroscopy provides direct sensitivity to the internal excitonic structure, it also exhibits intrinsic limitations at higher excitation densities. As the carrier density increases, the excitonic resonance broadens and the distinction between excitonic and plasma responses becomes increasingly ambiguous. To overcome this limitation, a differential spectroscopic method was developed in which intense THz pulses are used to selectively ionize excitons. This procedure effectively suppresses the excitonic contribution to the THz response, allowing the pure plasma response to be isolated. By subtracting this contribution from the total signal, the excitonic response can be reconstructed and the unperturbed exciton formation dynamics can be analyzed. Using this approach, exciton formation is found to occur on two distinct timescales. A rapid component on the order of 10 ps is followed by a slower process occurring on a timescale of approximately 250 ps. Within the investigated intermediate excitation regime, these formation times are found to be largely independent of the excitation energy.
During the formation process, a regime exists in which excitons and the electron–hole plasma coexist. This regime forms the basis for the investigation of exciton–electron scattering presented in Section 5.2. For this purpose, the OPTP setup was extended by introducing a second optical pump pulse, enabling independent control over exciton and plasma populations. Excitons are injected by resonant excitation of the $1s$ exciton transition, while the second pump pulse generates an electron–hole plasma with a tunable excess energy relative to the exciton population. The THz probe pulse monitors the exciton population before and after plasma injection.
The resulting THz spectra are analyzed using a Drude–Lorentz model, allowing the linewidth of the intraexcitonic $1s$–$2p$ transition and the exciton density to be extracted. From these quantities, elastic and inelastic contributions to the total scattering process can be determined. Interestingly, for the lowest investigated excess energy, inelastic scattering is strongly suppressed despite the excess energy exceeding the exciton binding energy. This behavior can be explained by phase-space restrictions arising from Fermi's Golden Rule: the available final states for the electrons are limited, preventing efficient inelastic scattering. Furthermore, the overall scattering efficiency is found to be largely independent of the excess energy, while the relative contributions of elastic and inelastic processes vary with the plasma energy. The transient screening of excitonic states by an independently injected electron–hole plasma is investigated in Section 5.3. Monitoring the resonance frequency of the intraexcitonic 1s–2p transition as a function of the injected carrier density provides a direct, time-resolved measurement of the reduction in exciton binding energy due to Coulomb screening. The magnitude of this shift is found to scale approximately linearly with carrier density. The buildup time of the screening is found to be independent of carrier density but depends on the excess energy of the injected carriers: approximately 6 ps for 9 meV and approximately 18 ps for 40 meV excess energy. This counterintuitive ordering is attributed to the additional hot carriers generated by inelastic exciton dissociation at 40 meV, which must first thermalise before contributing efficiently to screening.
Transient excitonic states induced by a below-resonance optical pump pulse are demonstrated in Section 5.4. Although no real exciton population is created under these conditions, a distinct blue-shifted intraexcitonic absorption feature emerges during the temporal overlap of pump and probe pulses. The signal scales linearly with pump fluence and is independent of THz probe field strength, ruling out nonlinear processes and establishing a first-order optical response. The observations are consistent with a coherent, optically dressed excitonic polarisation in direct analogy to the optical Stark effect.
Taken together, the results presented in this thesis demonstrate the versatility of THz

spectroscopy for studying quasiparticle dynamics in semiconductors. From the development of broadband THz sources to the investigation of exciton formation and scattering processes, the presented work highlights both the strengths and intrinsic limitations of THz techniques for probing many-body interactions in semiconductor systems.
The main contributions of this thesis can be summarized as follows. First, a broadband method for generating gapless THz radiation based on quantum interference currents in germanium is demonstrated, enabling compact THz sources compatible with low-power fiber lasers. Second, a differential THz spectroscopy technique is developed that allows excitonic and plasma contributions to be separated even in regimes where their spectral signatures strongly overlap. Third, the controlled injection of excitons and electron–hole plasmas provides direct insight into exciton–electron scattering processes and reveals the role of phase-space restrictions in determining the relative importance of elastic and inelastic scattering channels.

Outlook

Despite decades of research on excitons, many aspects of their formation and interaction dynamics remain incompletely understood. The experimental approaches developed in this thesis open several promising directions for future investigations.
One natural extension would combine the techniques used in Paper III and Paper I to study exciton formation in the presence of a pre-existing exciton population. In such an experiment, excitons could first be injected resonantly, followed by a second optical pulse that creates an electron–hole plasma via nonresonant excitation. Monitoring the subsequent formation dynamics would allow the influence of an incoherent exciton population on the formation process to be investigated. Depending on the underlying many-body interactions, the presence of excitons may either accelerate formation through stimulated scattering processes or inhibit it through phase-space filling effects. Experimentally, this scenario could be realized by modifying the modulation scheme of the dual-pump setup, for example by chopping the second optical pump instead of the first.
Another promising direction concerns exciton–exciton scattering processes. Such experiments could be implemented using a similar dual-pump scheme, with both optical pulses tuned resonantly to the $1s$ exciton transition. By independently controlling two exciton populations, the influence of exciton density on intraexcitonic linewidths and scattering rates could be systematically investigated, providing further insight into many-body interactions within dense excitonic systems.
Finally, the experimental platform could be extended by replacing one of the optical pump pulses with an intense THz pump pulse. In this configuration, the optical pulse would first create a population of $1s$ excitons, which could then be coherently driven into higher excitonic states by resonant THz excitation. A subsequent THz probe pulse would allow the occupation and decay dynamics of excited states such as the $2p$ exciton to be monitored directly. Such experiments would provide direct access to the lifetimes and relaxation pathways of higher excitonic states and could shed light on the role of many-body interactions in excitonic relaxation dynamics. This experiment would work well in conjunction with investigating transient excitonic states shown in section 5.4. Here, the additional THz pulse could convert the transient excitonic polarization into an incoherent exciton population by converting the $1s$-like polarization into a $2p$ occupation. More broadly, the ability to selectively manipulate and probe excitonic populations with intense THz fields may open new opportunities for investigating nonequilibrium many-body dynamics in semiconductors and other strongly interacting quantum materials.

7 Relevant Publications

I - Inhibited inelastic scattering for near-band edge excitations in two-dimensional charge-carrier systems, Ref. [191]

D. Anders, F. Dobener, F. Schäfer, S. Chatterjee, M. Stein

Abstract

A multiple pump-terahertz probe experiment enables the clear distinction between elastic and inelastic scattering of excitons with a free electron-hole plasma in (Ga,In)As multi-quantum wells. Low plasma energies dictate the prevalence of elastic scattering by inhibiting inelastic processes due to the absence of final states for quasiparticles. Yet, an increased plasma energy results in a progressive destruction of excitons. Notably, despite plasma energy variations, the interaction strength between excitons and the electron-hole plasma remains unaltered.

Conclusion

In conclusion, our study underscores the pivotal roles of charge carrier excess energies and final state availability in controlling the inelastic scattering behavior of excitons with near-band edge charge carriers. While there is enough excess energy to overcome the exciton binding energy, a lack of final states for the unbound charge carriers prevents the break-up of excitons and allows only elastic scattering. Moreover, we find that the interaction strength between excitons and an electron-hole plasma remains unaltered regardless of the excess energy involved. Intriguingly, increased energy transfer primarily drives the destruction of excitons via inelastic scattering rather than elastic scattering mechanisms that only increase their kinetic energy.

Contribution

The experimental setup was designed by me in collaboration with S.C. and M.S., and subsequently constructed together with M.S. M.S. and I specified the technical requirements for the measurement software, which was developed by F.D. All measurements were carried out by me with support by M.S., while the linear absorption data were provided by F.S. I analyzed the experimental data, wrote the first draft of the manuscript, and designed all corresponding figures. The final manuscript was revised in close collaboration with M.S. and S.C.

https://doi.org/10.1103/PhysRevLett.132.106901

Inhibited inelastic scattering for near-band edge excitations in two-dimensional charge-carrier systems

D. Anders, F. Dobener, F. Schäfer, S. Chatterjee, and M. Stein*
Institute of Experimental Physics I and Center for Materials Research (LaMa), Justus-Liebig-University Giessen, Heinrich-Buff-Ring 16, D-35392 Giessen, Germany
(Dated: August 30, 2023)

A multiple pump-terahertz probe experiment enables the clear distinction between elastic and inelastic scattering of excitons with a free electron-hole plasma in (Ga,In)As multi-quantum wells. Low plasma energies dictate the prevalence of elastic scattering by inhibiting inelastic processes due to the absence of final states for quasiparticles. Yet, an increased plasma energy results in a progressive destruction of excitons. Notably, despite plasma energy variations, the interaction strength between excitons and the electron-hole plasma remains unaltered.

Scattering is a fundamental concept native to many branches of physics, spanning astrophysics, classical mechanics, quantum mechanics, nuclear physics, and solid-state physics. The latter commonly describes complex interacting many-body systems where scattering processes naturally play a pivotal role. Prominent examples in semiconductors are phonons, associated with lattice vibrations, or holes, which are the positively charged counterparts of electrons. To simplify the mathematical description of these systems, the concept of quasiparticles emerges, treating these collective excitations as new particles with unique properties instead of individual interactions between a vast number of (elementary) particles [1, 2]. As such they exhibit a dispersion relation and are capable of scattering with each other, exchanging energy and momentum.

The interaction of quasiparticles plays a crucial role in determining the performance of many semiconductor-based devices in our modern technological age, including lasers, solar cells, and transistors [3–6]. Moreover, scattering processes are fundamental in investigating phenomena like Bose-Einstein condensates of excitons, bound electron hole pairs [7], superconductivity [8], dynamical Bloch oscillations [9] or Floquet-Bloch bands [10]. Accordingly, extensive research has been dedicated to investigate scattering processes between quasiparticles, particularly excitons and electrons in semiconductors [11–19].

The coherent lifetime and optical linewidths of excitons have been widely utilized to study these processes, both of which are significantly affected by scattering. Four-wave-mixing spectroscopy (FWM) quantifies such processes as scattering leads to dephasing of exciton polarizations [20–22]. Here, the dephasing time associated with the $1s$ exciton polarization can be analyzed in the presence of either an electron-hole plasma or incoherent excitons that can be injected by an additional prepulse [11, 12, 23]. Furthermore, the broadening of exciton transitions offer insights into electron-exciton scattering dynamics, as dephasing times inversely correlate with homogeneous linewidths [12, 21]. This is effectively utilized in time-resolved photoluminescence (TRPL) spectroscopy and optical transmission experiments, monitoring the respective linewidths [24–29]. Again, additional excitation pulses can tailor the desired scattering environment [23, 26]. However, such experimental investigations only provide information on the rate at which scattering events occur, yet, they are unable to distinguish between inelastic and elastic scattering, i.e., they cannot identify if energy is dissipated or if both the energy and the translational momentum are rigorously conserved. This requires an additional measure, namely quantitative information on the size of the exciton population. These data are hard to access by purely optical means [30] while terahertz (THz) spectroscopy more conveniently provides a measure for the exciton population [31, 32].

THz pulses probe transitions between excitonic energy levels, irrespective of the exciton's center-of-mass momentum [32]. Specifically, the transition between the exciton ground state and an excited state, such as the $1s$ to $2p$ transition (commonly termed intraexcitonic transition), is directly proportional to the population of the $1s$ exciton ground state according to Fermi's Golden Rule [31]. Therefore, THz probe spectroscopy becomes an ideal tool to detect inelastic scattering processes that result in the destruction of $1s$ exciton populations [33].

In this Letter, we elucidate the robustness of bound quasiparticles, here specifically incoherent excitons, to ionization due to energy transfer by inelastic scattering for energies up to several times their binding energy. We examine excess energies slightly above the binding energy of excitons and demonstrate that, despite sufficient energy for ionization, final state considerations render these surplus energies insufficient for efficient exciton ionization via inelastic scattering. To explore this phenomenon, we study the scattering of a pre-injected incoherent exciton population with a free electron-hole plasma, varying the excess energy of the excitation and the charge-carrier density. By analyzing the exciton-population decay-dynamics following the injection of an electron-hole plasma, we determine the inelastic scattering parameter for different excess energies of the injected plasma. The presence of the electron-hole plasma manifests through spectral broadening of the intraexcitonic

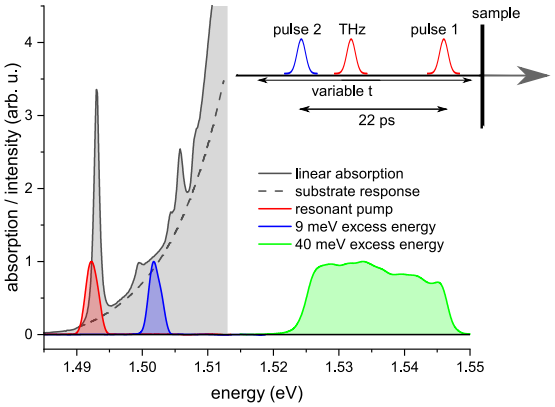

FIG. 1. Absorption (grey) of the (Ga,In)As quantum wells. The absorption of the GaAs substrate is shown as a dashed line. The first optical pulse (red) resonantly excites a 1s exciton population. The blue and green pulses correspond to the second optical pulse with excess energies of 9 meV and 40 meV with respect to the 1s exciton resonance, respectively. The inset illustrates the pulse sequence of the experiment.

$1s$-$2p$ absorption line, allowing us to directly monitor the total scattering.

We employ a multiple optical pump - terahertz probe setup featuring two independently tunable optical pulses to study a high-quality multiple quantum well structure which provides the quasi two-dimensional electronic system. Details of the sample structure as well as the experimental setup are available in the Supplementary Material at Ref. 34. Figure 1 displays the linear absorption spectrum of the sample, revealing a pronounced $1s$ exciton resonance at 1.493 eV. The first pulse resonantly excites the sample at this exciton transition; its spectrum is shown in red. Subsequently, this excitation turns into an incoherent quasi-steady-state exciton population. The second pulse injects the scattering partners 22 ps after the initial pulse. Its spectral position determines the excess energy of the additional electron-hole plasma. The representative excitation spectra corresponding to 9 and 40 meV excess energy relative to the $1s$ exciton resonance are given in blue and green, respectively. Scanning the ps-long THz pulse in time probes the quasiparticle response as illustrated in the inset.

A phenomenological Drude-Lorentz model describes the pump-induced changes of the frequency-dependent dielectric function $\Delta\epsilon(\omega) = \Delta\epsilon_1(\omega) + i\Delta\epsilon_2(\omega)$ which is monitored by the THz-response. Its quantitative analysis disentangles the individual quasipartiple dynamics [35]. The Drude response is typical for a free electron-hole plasma [36], while an $1s$ exciton population manifests itself in an intraexcitonic transition described by a Lorentzian oscillator [32]. The simultaneous fit to both, the real and the imaginary part of $\Delta\epsilon(\omega)$ yields robust results for the homogeneous linewidth Δ_{hom} and the exciton sheet-density n_x. Further details are provided in the supplemental material [34].

Figure 2 **a)** shows contour plots of the THz-absorption for 9 meV (left) and 40 meV (right) excess energy of the respective second excitation pulses. The charge-carrier density of the additionally injected carriers is kept comparable at $4.6 \cdot 10^9$ cm^{-2} and $4.8 \cdot 10^9$ cm^{-2} for 9 and 40 meV surplus energy, respectively. The pronounced absorption peak at 1.36 THz observed at early times indicates that the first optical pulse creates a pure $1s$ exciton population. After a 22 ps delay, the second pulse interacts with the sample. The data distinctly reveal varying THz absorption depending on the excess energy of the second pulse. For 9 meV excess energy, the intraexcitonic transition at 1.36 THz broadens significantly and slightly shifts towards lower frequencies. Similarly, with 40 meV excess energy, the intraexcitonic transition also broadens shortly after the second pulse. In this case, however, the intraexcitonic oscillator strength additionally decreases and simultaneously gives rise to a Drude-like response at frequencies below 0.5 THz. This Drude response is typical for a free electron-hole plasma [36]. Thus, the breakup of a $1s$ exciton population into a free electron-hole plasma due to inelastic scattering of excitons with a hot electron-hole plasma is caught red-handed. This is vividly illustrated in Figure 2 **b)**, which shows the intraexcitonic linewidth against excitation density for both excess energies, and the intraexcitonic oscillator strength relative to its value prior to the injection of the electron-hole plasma by the second pulse. It is apparent that both excitation conditions result in a comparable broadening of the intraexcitonic resonance, which increases with charge carrier density. However, the oscillator strength notably decreases with rising density for the 40 meV excess energy excitation, dropping to a mere one-third of its original strength at the highest excitation density. In contrast, for the low excess energy excitation, despite a similar broadening of the intraexcitonic resonance, there is only a marginal reduction in oscillator strength, partly attributable to radiative recombination processes. The distinct difference in oscillator strength between the two excess energies unequivocally stems from the significantly more frequent occurrence of inelastic scattering processes at 40 meV excess energy.

For a quantitative interpretation of these differences, one has to consider that elastic and inelastic scattering interactions between excitons and electrons yield significantly different outcomes and consequently leave different signatures in their terahertz responses. Elastic scattering on the one hand exchanges momentum and kinetic energy between the two scattering partners. Here, excitons and electrons persist, however, now featuring modified center-of-mass momenta. Consequently, elastic scattering processes preserve the $1s$ exciton population and do not affect the oscillator strength associated with the intraexciton transitions [37]. On the other hand, inelastic

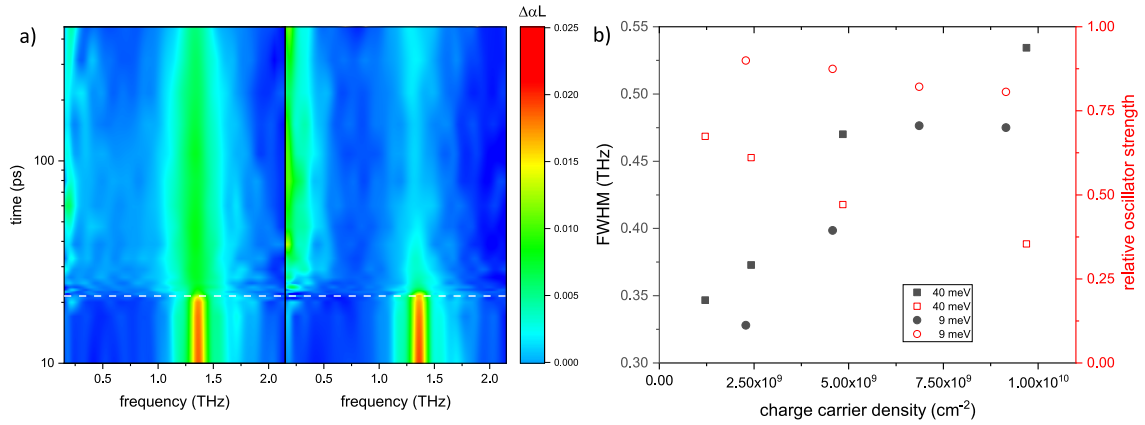

FIG. 2. **a)** THz absorption for 9 meV (left) and 40 meV (right) excess energy but nearly identical charge-carrier densities of the injected electron-hole plasma. The time-of-arrival of the second pulse on the sample is marked by the dashed white line. **b)** FWHM (grey symbols) and oscillator strength (red symbols) of the $1s$-$2p$ transition. For both excess energies, the FWHM is directly proportional to the charge-carrier density injected by the second optical pulse. The relative oscillator strength is derived by dividing the oscillator strength after the arrival of the second pulse by the oscillator strength before the second pulse.

scattering dissipates parts of the kinetic energy into another form of energy. In this case, the electron and exciton exchange enough energy to excite the exciton into a higher-energy (bound) state or even overcome its binding energy and ionize the exciton. In other words, some of the kinetic energy reduces or even completely dissipates the binding energy between the bound electron-hole pair. Consequently, this either results in one electron and one exciton in an higher-energy excited state or two free electrons and a hole due to inelastic scattering.

To quantify these inelastic scattering processes, we examine the exciton component n_x of the Drude-Lorentz model for each timestep. Fitting an exponential function to the decreasing exciton fraction after the arrival of the second optical pulse yields the decay time τ_1 of the exciton population caused solely by the inelastic scattering with the electron-hole plasma. The inelastic scattering induces a homogeneous broadening of the $1s$ state according to $\Delta_{\mathrm{hom}} = {}^{2}/_{\tau_1}$ [11].

All scattering processes contribute to the broadening of the intraexcitonic transition while only inelastic scattering processes contribute to the destruction of the exciton population. In analogy to optical transmission, FWM or TRPL experiments, we correlate the change of the intraexcitonic linewidth with the total scattering rate [11, 38–40]. The excitation-induced intraexcitonic line broadening Δ_{intra} is determined by comparing the intraexcitonic linewidth before $[\Gamma_{\mathrm{hom}}(0)]$ and after the second optical pulse interacts with the sample $[\Gamma_{\mathrm{hom}}(n)]$:

$$\Delta_{\mathrm{intra}} = \Gamma_{\mathrm{hom}}(n) - \Gamma_{\mathrm{hom}}(0). \tag{1}$$

Since the intraexcitonic linewidth of the $1s$-$2p$ transition is influenced by scattering processes in both the $1s$ and $2p$ states, we assume equal contributions from both states. Consequently, the broadening of the $1s$ exciton state (Δ_{hom}) can be expressed as $\Delta_{\mathrm{hom}} = {}^{\Delta_{\mathrm{intra}}}/\sqrt{2}$. To enhance accuracy, we average the linewidth of the $1s-2p$ transition from 14 ps to 17 ps after the initial resonant excitation, i.e., 5-8 ps before the second pulse and from 27-33 ps which is 5-11 ps after the second pulse.

In Figure 3a) the excitation-induced broadening of the $1s$ exciton state Δ_{hom} is plotted against the charge-carrier density induced by the second pulse. This figure also illustrates the broadening of the $1s$ exciton state caused by inelastic scattering for an excess energy of the optically induced electron-hole plasma of 40 meV. In the low-density regime, the broadening of the homogeneous linewidth of the $1s$ state exhibits a linear density dependence [41]. Therefore, we fit the experimental data in Figure 3a) using:

$$\Delta_{\mathrm{hom}} = \gamma a_{\mathrm{B}}^2 E_{\mathrm{B}} n, \tag{2}$$

where a_{B} is the exciton Bohr radius, E_{B} the exciton binding energy, n the charge-carrier density, and γ is a dimensionless parameter representing the interaction strength of excitons with the free electron-hole plasma. The exciton binding energy in quantum well systems is well approximated by multiplying the resonance energy of the intraexcitonic $1s$-$2p$ transition by ${}^{9}/_{8}$ [42]. For our case, this yields an exciton binding energy of $E_{\mathrm{B}} = E_{1s-2p} \cdot {}^{9}/_{8} = 5.625\,\mathrm{meV} \cdot {}^{9}/_{8} = 6.33\,\mathrm{meV}$. Since the product of $E_{\mathrm{B}} \cdot a_{\mathrm{B}}$ is constant for a material system [43], we can use the exciton binding energy and the Bohr radius of a very similar quantum well structure [44] to derive an exciton Bohr radius of 11 nm for our sample. This allows us to determine the scattering parameter γ

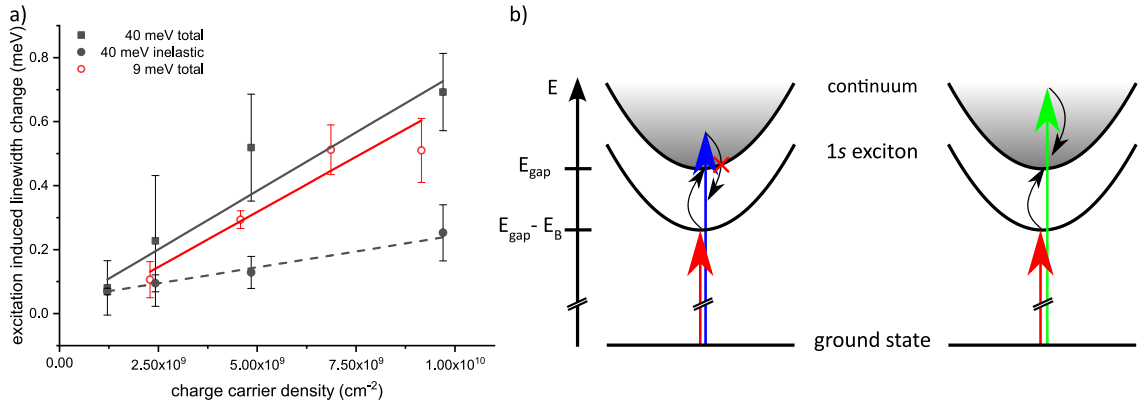

FIG. 3. a) Change of the 1s exciton linewidth induced by the additional charge carriers with an excess energy of 40 meV (grey) and 9 meV (red), respectively. The scattering parameters are derived from the linear fits to the density-dependent 1s exciton line broadening. b) Schematic drawing of the inelastic scattering processes for 9 meV (left) and 40 meV (right) excess energy. The short black arrows indicate the energy transfer between the 1s excitons and the free charge carriers.

from the slope m of the fits in Figure 3a) according to:

$$\gamma = \frac{m}{a_{\mathrm{B}}^2 E_{\mathrm{B}}}. \tag{3}$$

The elastic contribution (γ_{el}) to the total scattering parameter is then deduced by subtracting the inelastic scattering parameter from the total scattering parameter.

Table I shows the extracted total scattering parameters as well as their elastic and inelastic contributions for both excess energies. The total scattering parameters $\gamma_{\mathrm{tot,9\,meV}} = 8.8$ and $\gamma_{\mathrm{tot,40\,meV}} = 9.32$ are similar. They are withing the margin of error of the scattering parameters determined in Ref. 11 for a 12 nm GaAs single quantum well and about a factor of 2 bigger than the one found for similar (Ga,In)As quantum well structures [22]. For 9 meV excess energy, determining the inelastic scattering parameter is challenging due to the negligible change in exciton density n_x after electron-hole pair injection by the second optical pulse. However, given the minimal change in n_x, it is reasonable to assume that the contribution of inelastic scattering is negligible. In contrast, the inelastic scattering parameter amounts to 2.54 for 40 meV excess energy which results in an elastic scattering parameter of 6.78.

TABLE I. Scattering parameters obtained for the two different excess energies. The experimental data do not warrant the evaluation of an inelastic scattering parameter for 9 meV excess energy.

	γ_{tot}	γ_{in}	γ_{el}
9 meV	8.8±1.8	-	8.8±1.8
40 meV	9.34±1.53	2.54±0.23	6.78±1.76

Interestingly, virtually no inelastic scattering is observed at 9 meV excess energy, regardless of the carrier density injected by the second pulse. Notably, charge carriers injected with a surplus energy of 9 meV above the 1s exciton should have enough excess energy to overcome the 6.33 meV binding energy and thus annihilate excitons in scattering events. To explain the lack of inelastic scattering, we have to revisit the linear absorption spectrum given as grey-shaded area in Figure 1 and consider Fermi's Golden Rule. The latter states in simple terms that scattering processes require both occupied initial states and unoccupied final states in addition to an interaction strength. From Figure 1 it is apparent that there are no final states between the 1s exciton resonance and the conduction band edge that the electrons can occupy after an inelastic scattering event with an exciton, i.e., an energy exchange of at least 5.6 meV necessary to bring it into an excited state. Consequently, inelastic scattering of excitons with charge carriers close to the band edge is strongly suppressed as there are no states available for electrons to occupy after the scattering event. This phenomenon is visually depicted in Figure 3b). Here, the energy transfer linked to an inelastic scattering process involving an 1s exciton would propel the excited electron-hole plasma (indicated by the blue arrow), carrying an excess energy of 9 meV, into a restricted energy region within the semiconductor structure. Only for higher excitation energies, represented by the green arrow in Figure 3b), the electron-hole plasma finds states in the continuum that can be occupied after the energy transfer required for an inelastic scattering process.

Intriguingly, the total scattering parameters remain remarkably consistent despite the contrasting ionization behaviors exhibited at different excess energies. This sug-

gests that the interaction strength between excitons and an electron-hole plasma remains unaffected by changes in excess energy. Higher excess energies naturally open pathways for scattering processes involving greater energy transfer. These processes can manifest themselves in two distinct forms: inelastic scattering causing exciton destruction, or elastic scattering which transfers kinetic energy without perturbing the Coulomb bond between electron and hole. Considering the conservation laws for energy and momentum in classical mechanics, both possibilities are viable. Intuitively, one might anticipate an increase in elastic scattering alongside increased inelastic scattering. However, a classical analogy holds true: in the macroscopic world, inelastic scattering inevitably occurs for sufficient energy exchange causing mechanical deformation. For instance, in a car crash, inelastic scattering prevails despite mechanical conservation laws allowing for elastic scattering resulting in undamaged vehicles. Our experimental results suggest the extension of this classical observation to the quantum realm, specifically to scattering processes involving quasiparticles. Notably, increased excess energy exclusively amplifies the efficiency of inelastic scattering. This result implies that scattering processes that transfer energies sufficient to break the exciton bond primarily promote the destruction of excitons via inelastic scattering, rather than the increase in their kinetic energy characteristic for elastic scattering processes.

In conclusion, our study underscores the pivotal roles of charge carrier excess energies and final state availability in controlling the inelastic scattering behavior of excitons with near-band edge charge carriers. While there is enough excess energy to overcome the exciton binding energy, a lack of final states for the unbound charge carriers prevents the break-up of excitons and allows only elastic scattering. Moreover, we find that the interaction strength between excitons and an electron-hole plasma remains unaltered regardless of the excess energy involved. Intriguingly, increased energy transfer primarily drives the destruction of excitons via inelastic scattering rather than elastic scattering mechanisms that only increase their kinetic energy.

ACKNOWLEDGEMENT

Financial support by the European Regional Development fund through the Innovation Laboratory High-Performance Materials is acknowledged.

* markus.stein@exp1.physik.uni-giessen.de

[1] L. Keldysh and A. Kozlov, Sov. Phys. JETP **27**, 521 (1968).
[2] H. Haug and S. Schmitt-Rink, Progress in Quantum Electronics **9**, 3 (1984).
[3] J. Xiang, W. Lu, Y. Hu, Y. Wu, H. Yan, and C. M. Lieber, Nature **441**, 489 (2006).
[4] R. Köhler, A. Tredicucci, F. Beltram, H. E. Beere, E. H. Linfield, A. G. Davies, D. A. Ritchie, R. C. Iotti, and F. Rossi, Nature **417**, 156 (2002).
[5] V. Gantmakher and Y. Levinson, *Carrier scattering in metals and semiconductors* (Elsevier, 2012).
[6] A. Svizhenko and M. Anantram, IEEE Transactions on Electron Devices **50**, 1459 (2003).
[7] Y. Morita, K. Yoshioka, and M. Kuwata-Gonokami, Nature Communications **13**, 5388 (2022).
[8] B. Keimer, S. A. Kivelson, M. R. Norman, S. Uchida, and J. Zaanen, Nature **518**, 179 (2015).
[9] O. Schubert, M. Hohenleutner, F. Langer, B. Urbanek, C. Lange, U. Huttner, D. Golde, T. Meier, M. Kira, S. W. Koch, *et al.*, Nature photonics **8**, 119 (2014).
[10] S. Ito, M. Schüler, M. Meierhofer, S. Schlauderer, J. Freudenstein, J. Reimann, D. Afanasiev, K. Kokh, O. Tereshchenko, J. Güdde, *et al.*, Nature , 1 (2023).
[11] A. Honold, L. Schultheis, J. Kuhl, and C. W. Tu, Physical Review B **40**, 6442 (1989).
[12] L. Schultheis, J. Kuhl, A. Honold, and C. W. Tu, Physical Review Letters **57**, 1635 (1986).
[13] S. Elkomoss and G. Munschy, Journal of Physics and Chemistry of Solids **38**, 557 (1977).
[14] S. Elkomoss and G. Munschy, Journal of Physics and Chemistry of Solids **40**, 431 (1979).
[15] Y.-P. Feng and H. N. Spector, Journal of Physics and Chemistry of Solids **48**, 593 (1987).
[16] B. Deveaud, F. Clérot, N. Roy, K. Satzke, B. Sermage, and D. Katzer, Physical review letters **67**, 2355 (1991).
[17] C. Ciuti, V. Savona, C. Piermarocchi, A. Quattropani, and P. Schwendimann, Physical Review B **58**, 7926 (1998).
[18] G. Göger, M. Betz, A. Leitenstorfer, M. Bichler, W. Wegscheider, and G. Abstreiter, Physical Review Letters **84**, 5812 (2000).
[19] M. Betz, G. Göger, A. Leitenstorfer, M. Bichler, G. Abstreiter, and W. Wegscheider, Physical Review B **65**, 085314 (2002).
[20] T. Yajima and Y. Taira, Journal of the physical society of Japan **47**, 1620 (1979).
[21] L. Schultheis, A. Honold, J. Kuhl, K. Köhler, and C. Tu, Physical Review B **34**, 9027 (1986).
[22] M. Fey, M. Stein, C. Fuchs, W. Stolz, K. Volz, and S. Chatterjee, Phys. Rev. B **106**, 165303 (2022).
[23] M. Koch, R. Hellmann, G. Bastian, J. Feldmann, E. Göbel, and P. Dawson, Physical Review B **51**, 13887 (1995).
[24] R. Leite, J. Shah, and J. Gordon, Physical Review Letters **23**, 1332 (1969).
[25] W. Liu, D. Jiang, K. Luo, Y. Zhang, and X. Yang, Applied physics letters **67**, 679 (1995).
[26] A. Manassen, E. Cohen, A. Ron, E. Linder, and L. Pfeiffer, Physical Review B **54**, 10609 (1996).
[27] H. Wang, K. Ferrio, D. G. Steel, Y. Hu, R. Binder, and S. Koch, Physical review letters **71**, 1261 (1993).
[28] D. Wake, H. Yoon, J. Wolfe, and H. Morkoc, Physical Review B **46**, 13452 (1992).
[29] D. Huang, H. Chu, Y. Chang, R. Houdré, and H. Morkoc, Physical Review B **38**, 1246 (1988).

[30] S. Chatterjee, C. Ell, S. Mosor, G. Khitrova, H. Gibbs, W. Hoyer, M. Kira, S. Koch, J. Prineas, and H. Stolz, Physical review letters **92**, 067402 (2004).
[31] R. A. Kaindl, M. A. Carnahan, D. Hägele, R. Lövenich, and D. S. Chemla, Nature **423**, 734 (2003).
[32] S. Koch, M. Kira, G. Khitrova, and H. Gibbs, Nature materials **5**, 523 (2006).
[33] M. Stein, F. Schäfer, and L. Gomell, Physical Review B **99**, 144310 (2019).
[34] See Supplemental Material at [url], which includes Refs. [36, 45, 46], for details of the sample, the calculation of the charge carrier densities as well as the Drude-Lorentz analysis and the experimental setup.
[35] P. Steinleitner, P. Merkl, P. Nagler, J. Mornhinweg, C. Schüller, T. Korn, A. Chernikov, and R. Huber, Nano Letters **17**, 1455 (2017).
[36] R. Ulbricht, E. Hendry, J. Shan, T. F. Heinz, and M. Bonn, Reviews of Modern Physics **83**, 543 (2011).
[37] G. Ramon, A. Mann, and E. Cohen, Physical Review B **67**, 045323 (2003).
[38] M. Koch, R. Hellmann, G. Bastian, J. Feldmann, E. O. Göbel, and P. Dawson, Physical Review B **51**, 13887 (1995).
[39] A. Manassen, E. Cohen, A. Ron, E. Linder, and L. N. Pfeiffer, Physical Review B **54**, 10609 (1996).
[40] R. C. C. Leite, J. Shah, and J. P. Gordon, Physical Review Letters **23**, 1332 (1969).
[41] G. Manzke, K. Henneberger, and V. May, physica status solidi (b) **139**, 233 (1987).
[42] K.-T. Tsen, ed., *Ultrafast Phenomena in Semiconductors* (Springer New York, New York, NY, 2001).
[43] A. Efremov, V. Litovchenko, and A. Sarikov, Materials Science and Engineering: C **23**, 165 (2003).
[44] M. Stein, C. Lammers, P.-H. Richter, C. Fuchs, W. Stolz, M. Koch, O. Vänskä, M. J. Weseloh, M. Kira, and S. W. Koch, Phys. Rev. B **97**, 125306 (2018).
[45] Q. Wu and X. Zhang, Applied Physics Letters **67**, 3523 (1995).
[46] A. Nahata, A. S. Weling, and T. F. Heinz, Applied Physics Letters **69**, 2321 (1996).

Supplemental material

Supplemental Material: Inhibited inelastic scattering for near-band edge excitations in two-dimensional charge-carrier systems

D. Anders, F. Dobener, F. Schäfer, S. Chatterjee, and M. Stein*
Institute of Experimental Physics I and Center for Materials Research (LaMa), Justus-Liebig-University Giessen, Heinrich-Buff-Ring 16, D-35392 Giessen, Germany
(Dated: October 5, 2023)

This supplementary material provides comprehensive background information on the sample studied and a detailed description of the procedure used to calculate the photon and charge carrier densities. Additionally, it outlines the application of the Drude-Lorentz model for data analysis and provides specific details of the experimental setup utilized in this study.

SAMPLE INFORMATION

The sample investigated is grown by molecular beam epitaxy on semi-insulating, undoped, [100]-oriented GaAs substrate. The sample structure comprises 30 periods of $In_{0.04}Ga_{0.96}As$ quantum wells, each with a thickness of 8.5 nm interleaved between GaAs layers. The exceptional quality of the GaAs substrate, characterized by its minimal Urbach absorption tail, facilitates experiments in transmission geometry, eliminating the need for substrate etching. This ensures ultra homogeneous (Ga,In)As quantum wells of remarkable quality, evident from their distinctively narrow intraexcitonic $1s$-$2p$ transition linewidth, measuring less than 1 meV for low excitation densities. During experiments, the sample is held at a constant temperature of 6 K within a continuous flow liquid-He cryostat.

PHOTON AND CHARGE CARRIER DENSITIES

To calculate the photon densities and consequently the injected charge carrier densities, we apply the knife-edge method to measure the spot size of the optical as well as the THz pulses. This yields two circular spots with diameters of 2 mm and 440 µm for the optical pulse and the THz pulse, respectively. The power of the laser pulse is measured with a silicon power meter so that we can calculate the photon density per pulse ρ for the FWHM of the THz pulse. We weigh the absorption for each frequency of the sample's absorption $\alpha(\omega)$ with the spectrum of the optical pulse $I_0(\omega)$ to obtain the average absorption $\mathrm{A_{avg}}$ of the optical pulse:

$$A_{\mathrm{avg}} = \frac{\sum_\omega (I_0(\omega) - I_0(\omega) \cdot e^{-\alpha(\omega)L})}{\sum_\omega I_0(\omega)} \tag{1}$$

Subsequently, we can then determine the charge carrier density injected by each optical pulse.

$$n = \frac{(\rho - \rho R) \cdot A_{avg}}{i} \tag{2}$$

Here, R denotes the reflectance and i the number of quantum wells of the sample. For this sample we used a value of R = 0.33 and i = 30.

DRUDE-LORENTZ MODEL

The model consist of two components and can be described by the following equation:

$$\begin{aligned}\Delta\epsilon(\omega) = &\frac{f_{1s-2p}e^2}{L\epsilon_0\mu}\frac{n_x}{\omega_{res}^2 - \omega^2 - i\omega\Delta_{\mathrm{hom}}} \\ &- \frac{e^2}{L\epsilon_0\mu}\frac{n_{fc}}{\omega^2 + i\omega\Gamma}\end{aligned} \tag{3}$$

The first term describes the intraexcitonic $1s$-$2p$ transition as a Lorentzian resonance with the oscillator strength f_{1s-2p}, the resonance frequency ω_{res}, the excitonic sheet density n_x, and the homogeneous linewidth Δ_{hom}. The second part defines the Drude response of unbound charge-carriers. It consists of the charge-carrier sheet density

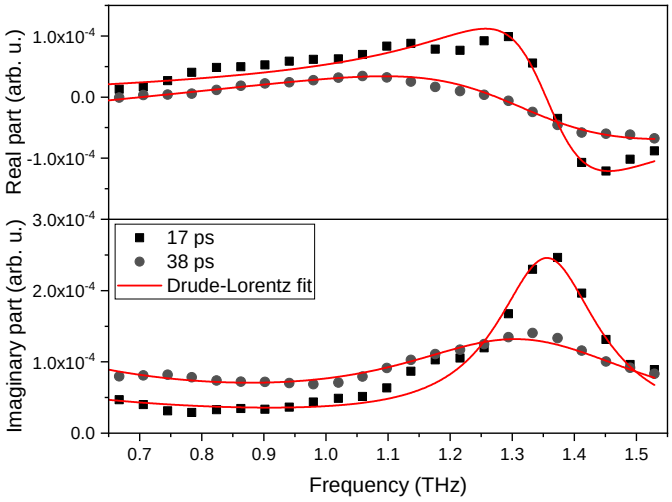

FIG. 1: The provided illustration showcases exemplary fits of the Drude-Lorentz model to the experimental data, delineated in the upper portion for the real part and the lower portion for the imaginary part of the dielectric function. In the figure, squares represent the dielectric response 17 ps subsequent to resonant excitation of the $1s$ exciton resonance. Correspondingly, the circles depict the dielectric response 16 ps after the second optical pulse introduces additional charge carriers, i.e. 38 ps after resonant excitation of $1s$ excitons.

n_{fc} and the carrier scattering rate Γ. Constants appearing in both terms and kept fixed for all fits are the sample thickness L, the effective mass μ, the electron charge e and the vacuum permeability ϵ_0. Exemplary fits of the model to experimental data before and after the non-resonant optical pulse hits the sample are shown in Figure 1. The homogeneous linewidths Δ_{hom} and excitonic sheet densities n_x obtained from the fitted Drude-Lorentz model can then be used to derive the respective scattering parameters, as shown in the manuscript.

EXPERIMENTAL SETUP

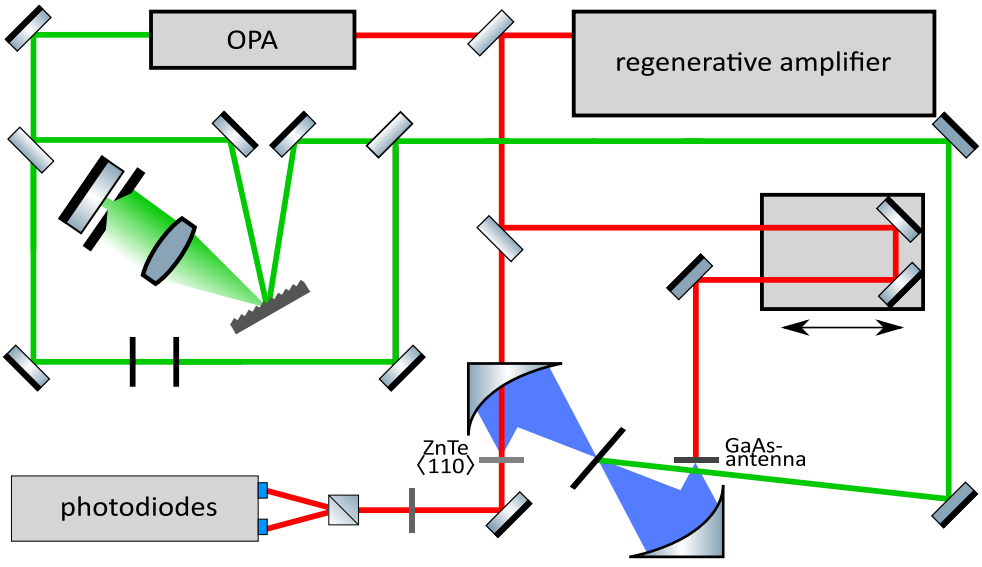

FIG. 2: Schematic of the multiple optical pump-terahertz probe setup

We use a 5 kHz regenerative amplifier (Spectra Physics Solstice Ace) which provides 50 fs pulses spectrally centered around 800 nm. The output is split into three parts. The first part is used to excite a large-aperture LT-grown GaAs antenna which emits ∼1 ps long terahertz (THz) pulses. These pulses are then used to probe the intraexcitonic 1s-2p transition, proving the existence of an incoherent exciton population. The second part is used as a gate pulse for the electro-optic sampling. Here, we use a 500 µm thick ZnTe crystal cut in ⟨110⟩ geometry [1, 2]. We purge the THz part of the setup with dry nitrogen gas to get rid of THz absorption by water vapor. The third part of the 800 nm output is fed into an optical parametric oscillator (OPA, Spectra Physics TOPAS) and converted to a spectrally broad pulse with a central energy of 1.493 eV (830.5 nm). Afterwards, we use a beam splitter divide the pump pulses into two. One part passes through a pulse shaper to obtain a full width at half maximum (FWHM) of 2.5 meV. It is then chopped and used to resonantly excite excitons in the sample at 1.493 eV. The other part is delayed via a linear translation stage by around 22 ps and spectrally tuned by a pair of short- and longpass filters, thus enabling the excitation of an electron-hole plasma with selectable excess energy (see Figure 1 in the main manuscript). A schematic representation of the experimental setup is illustrated in Figure 2.
The setup allows for the detection of THz pulses covering a bandwidth of 0.8-12.5 meV (0.2-3.0 THz). The THz pulses are resolved in the time domain using electro-optical sampling. Therefore, we sample a time window of 12 ps to which we apply a Blackman-Nutall window with a slope of 2 ps before Fourier-transforming the time domain traces into the frequency domain. This enables the analysis of the reference pulse $E(\omega)$ as well as the pump-induced change $\Delta E(\omega)$ due to the chopped first excitation pulse. The excitation-induced dielectric function change can then be calculated via [3]:

$$\Delta\epsilon(\omega) = \frac{2ic_0\sqrt{\epsilon_r}}{\omega L}\left(\frac{\Delta E(\omega)}{E(\omega)}\right), \tag{4}$$

where c_0 is the speed of light in vacuum, and ϵ_r the dielectric constant of the material.

* Electronic address: markus.stein@exp1.physik.uni-giessen.de

[1] Q. Wu and X. Zhang, Applied Physics Letters **67**, 3523 (1995).
[2] A. Nahata, A. S. Weling, and T. F. Heinz, Applied Physics Letters **69**, 2321 (1996).
[3] R. Ulbricht, E. Hendry, J. Shan, T. F. Heinz, and M. Bonn, Reviews of Modern Physics **83**, 543 (2011).

II - Coherent Control of Photocurrents in Germanium for Gapless and Broadband Terahertz Emission, Ref. [192]

D. Anders, M. Zengel, R. Rondriguez, K. Bräumer, S. Chatterjee, M. Stein

Abstract

Readily implemented broadband THz sources extend the reach of THz in diagnostic and sensing applications. Coherently controlled photocurrents in pure, cost-effective bulk Germanium and Germanium quantum wells render such broadband and gapless terahertz emission, overcoming the bandwidth limitations of traditional III-V and II-VI semiconductor-based THz emitters. Precise phase control between the fundamental and its second harmonic governs the THz field dynamics. The presented scheme, which utilizes low-energy 100 fs optical pulses centered around 1550 nm, is readily accessible through affordable ultrafast fiber laser technology and frequency doubling.

Conclusion

In conclusion, we demonstrate gapless, broadband THz emission up to 8 THz from pure bulk Ge as well as Ge QWs by generating coherently controlled quantum interference currents using 100 fs optical pulses around 1590 nm and their second harmonic. This all-optical approach utilizes the telecom wavelength and paves the way for generating broadband and gapless THz pulses even with comparatively inexpensive fiber lasers.

Contribution

The experimental setup was designed by me in collaboration with S.C. and M.S., and subsequently constructed together with M.S. and M.Z. All measurements were performed by me assisted by M.S., M.Z., R.R., and K.B. I analyzed the experimental data and prepared the first draft of the manuscript together with M.S. The final versions of all figures were designed by me. The final manuscript was revised in close collaboration with M.S. and S.C.

Journal of Infrared, Millimeter, and Terahertz Waves (2025) 46:57
https://doi.org/10.1007/s10762-025-01078-0

RESEARCH

Coherent Control of Photocurrents in Germanium for Gapless and Broadband Terahertz Emission

Daniel Anders[1] · Michael R. Zengel[1,2] · Rodrigo Sandoval Rodriguez[1] · Kalle Bräumer[1] · Sangam Chatterjee[1] · Markus Stein[1]

Received: 9 September 2024 / Accepted: 8 August 2025

Abstract
Readily implemented broadband THz sources extend the reach of THz in diagnostic and sensing applications. Coherently controlled photocurrents in pure, cost-effective bulk Germanium and Germanium quantum wells render such broadband and gapless terahertz emission, overcoming the bandwidth limitations of traditional III-V and II-VI semiconductor-based THz emitters. Precise phase control between the fundamental and its second harmonic governs the THz field dynamics. The presented scheme, which utilizes low-energy 100 fs optical pulses centered around 1550 nm, is readily accessible through affordable ultrafast fiber laser technology and frequency doubling.

Keywords Terahertz generation · Two-color excitation · Coherent control · Germanium

1 Introduction

Phase-stable electromagnetic pulses in the terahertz (THz) frequency range have revolutionized time-resolved spectroscopy, expanding its applications across a wide array of fields including molecular physics, medical diagnostics, and semiconductor research [1, 2]. Photoconductive antennas have emerged from the myriad of THz emitters as essential tools for table-top THz time-domain spectroscopy, especially in the frequency range up to 3–4 THz and using low pulse energies [3–5]. Alternatively, optical rectification is commonly the method of choice for THz generation in combination with high-intensity laser pulses [6–8]. However, those THz emitters mostly rely on III-V or II-VI semiconductor materials, which pose inherent limitations. The polar character of their crystal bond renders their optical phonons infrared active.

Markus Stein
markus.stein@exp1.physik.uni-giessen.de

1 Institute of Experimental Physics I and Center for Materials Research (ZfM/LaMa), Justus-Liebig-University Giessen, Heinrich-Buff-Ring 16, Giessen 35392, Hesse, Germany

2 Department of Physics and Astronomy, University of Alabama, 514 University Blvd, Tuscaloosa, AL 35401, USA

Published online: 15 August 2025

This leads to strong absorption at these phonon modes and to high reflectivity at their reststrahlen band, thereby constraining their spectral bandwidth to frequencies either below 4–7 THz or above 12–15 THz [2, 9, 10]. Various techniques have been introduced to overcome these limitations, such as two-color air plasma [11–14], which requires complex and costly laser amplifiers, or spintronic THz emitters [15, 16]. An alternative approach involves non-polar semiconductor materials like Silicon (Si) or Germanium (Ge) to potentially achieve a gapless broadband THz spectrum spanning beyond the low frequency-band limit of about 7 THz. For example, Ge-based photoconductive dipole antennas show promising capabilities in emitting broadband THz pulses [17, 18]. Ge's direct interband absorption above 0.8 eV and its small effective electron mass in the center of the Brillouin zone lead to the robust acceleration of photogenerated electrons and thus to efficient THz emission. However, active THz devices like photoconductive antennas still rely on complex material processing and electric contacting [19, 20]. In contrast to this electronic control, the motion of charge carriers in semiconductors can also be controlled all-optically by quantum interference currents [21, 22]. Here, the coherent excitation of a one-photon and a two-photon transition in a semiconductor using the fundamental and its second harmonic of a below-gap fs laser beam may couple the transitions between the valence band and conduction band. The phase relation between the two colors controls the interference of the interband transition amplitudes, resulting in a polar asymmetry in the momentum space distribution of the charge carriers. This creates an optically injected quantum interference current density that can be directly observed via its emitted THz radiation [23–28].

In this work, we harness the advantages of Ge while circumventing the intricacies of material processing and electric connections: coherently controlled quantum interference currents in readily available, cost-effective pure Ge as well as Ge quantum well structures yield gapless and broadband THz emission up to 8 THz. We employ ∼100 fs short optical pulses around 1590 nm—within the Telecom wavelength accessible through comparatively affordable fiber laser technology—together with a Beta Barium Borate (BBO) crystal for frequency doubling. The relative phase between the fundamental and its second harmonic is precisely controlled using a delay line before focusing both pulses on the Ge samples. The emitted THz radiation is collected with parabolic mirrors and analyzed using electro-optic sampling.

2 Materials and Methods

The optical setup utilized in this experiment is schematically shown in Fig. 1. A Ti:Sapphire laser-based amplifier (Solstice Ace) with a pulse length of 50 fs, a central wavelength of 800 nm, and a repetition rate of 5 kHz is split into two paths: one small fraction acts as a gate pulse for electro-optical sampling (EOS) and rest feeds an optical parametric amplifier (OPA, TOPAS:Twins). The OPA converts the light from the amplifier laser into the desired wavelength around 1590 nm (0.78 eV).

The OPA output is guided over a delay line and focused onto a BBO crystal to generate a second harmonic beam at 795 nm (1.56 eV). We utilized pulse energies of 480 nJ and 280 nJ of the fundamental and second harmonic, respectively. Both beams are incident on a dichroic mirror, which reflects wavelengths below 900 nm, i.e., the second

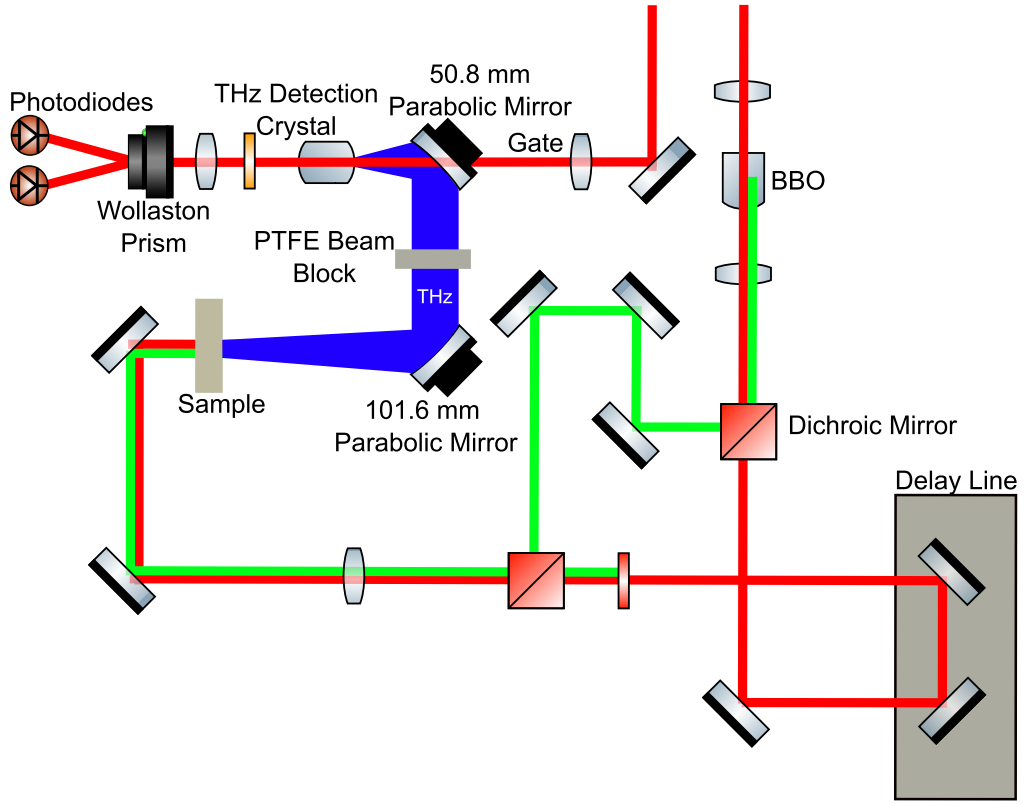

Fig. 1 Schematics of the experimental setup for the two-color excitation scheme together with the electro-optical sampling of the emitted THz beam

harmonic beam, while transmitting the fundamental beam. To precisely control the relative phase between the fundamental and its second harmonic, we employ a second delay stage. While the manufacturer's bidirectional positioning accuracy is specified as 1 µm (corresponding to a temporal resolution of approximately 6.7 fs), in our experiment, the stage is operated unidirectionally during phase scans. This significantly improves effective precision. Based on the manufacturer's resolution specifications and our own interferometric calibration, we estimate the practical unidirectional timing accuracy to be about 0.2 fs. A half-wave plate controls the polarization of the fundamental beam and, together with a polarization filter, ensures collinear polarization in relation to its second harmonic. Both beams are recombined using another dichroic mirror. The superimposed beams are focused on the Ge samples using a 20 cm focal length lens. The generated THz pulse is collimated by a parabolic mirror with a focal length of 101.6 mm and focused on a 500 µm-thick ZnTe or a 100 µm-thick GaP detection crystal by another parabolic mirror with a focal length of 50.8 mm. At the detection crystal, the THz pulse overlaps in space and time with the gate pulse for electro-optical sampling. After a quarter-wave plate, a Wollaston prism splits the gate pulse into its linear components, the power of which is recorded by two photodiodes. By delaying the OPA output and thus the THz pulse against the gate pulse, the entire THz pulse can be sampled in the time domain.

The sample employed for THz generation is either undoped n-type bulk Ge oriented along <111> direction with a thickness of 500 µm and a room-temperature resistivity

exceeding 30 Ωcm, or it comprises 50 Ge QWs each 15 nm thick, embedded in 19.8 nm $Si_{0.15}Ge_{0.85}$ barriers. Details of the latter are found in Ref. [29]. In both samples, the fundamental optical excitation is energy-wise at least above their indirect band gap while the second harmonic is far above their direct band gap.

3 Results and Discussion

First, we set the second delay line so that the fundamental and its second harmonic follow the same optical path and impinge on the bulk Ge sample at the same time. The time delay between the OPA output and the gate pulse is varied by the first delay line, with the voltage difference between the photodiodes being recorded for each time step. The result is shown in deep purple in Fig. 2. The Ge sample, excited by the fundamental beam and its second harmonic, emits a strong THz pulse on a picosecond time scale. Although the field strength from Ge is lower, its performance is noteworthy given the unbiased, compact setup and its broadband, gapless emission characteristics. Moreover, the Ge emitter is compatible with high-repetition-rate sources (e.g., MHz fiber lasers), which can enhance the signal-to-noise ratio significantly—especially relevant for spectroscopic applications. By carefully moving the second delay line, i.e., the phase delay between the fundamental and its second harmonic, the emitted THz

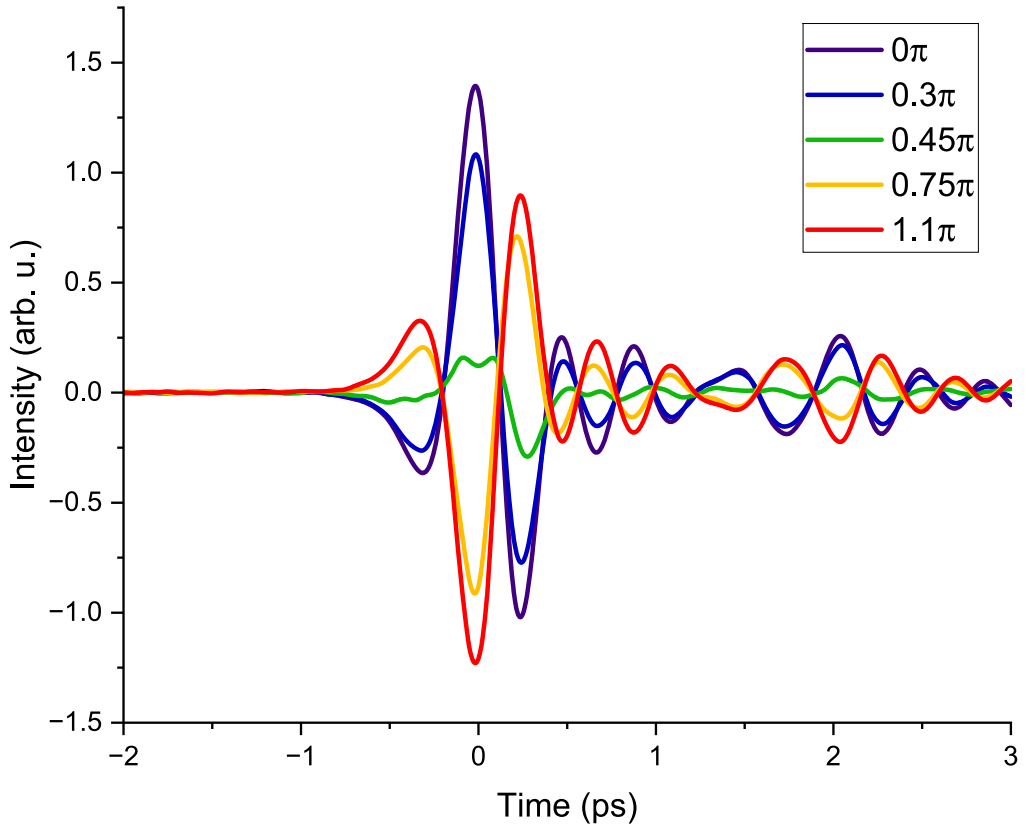

Fig. 2 Time domain of the detected THz pulses emitted from bulk Ge for different relative phase delays between the fundamental optical pulse and its second harmonic

pulses are controlled. The polarity of the emitted THz radiation can be inverted by moving the second delay path by half a wavelength of the second harmonic, i.e., by changing its phase by π. The relative phase between the fundamental beam and the second harmonic thus controls the polar asymmetry in the momentum space distribution of the excited charge carriers. The control of the current direction in the Ge sample is directly reflected in the emitted THz radiation shown in Fig. 2. Relative phase delays of 0 or π render the maximum amplitudes at opposite polarities, Almost no THz emission can be observed for relative phase delays of around $\frac{\pi}{2}$ due to symmetric k-space injection conditions.

We further investigate the dependence of the THz emission on the relative phase between the fundamental beam and its second harmonic by setting the first delay line to the maximum of the THz pulse (fixed time of 0 ps in Fig. 2) and then traversing the second delay line, i.e., the time or phase delay between fundamental and second harmonic. At large delays, i.e., when the fundamental beam and its second harmonic do not overlap in time, there is no THz emission from the Ge sample as evident in Fig. 3 for delays around 200 fs. THz is only emitted if there is a temporal overlap between the two optical beams. The maximum THz emission is reached with perfect temporal overlap, whereby the polarity changes with phase shifts of half a wavelength

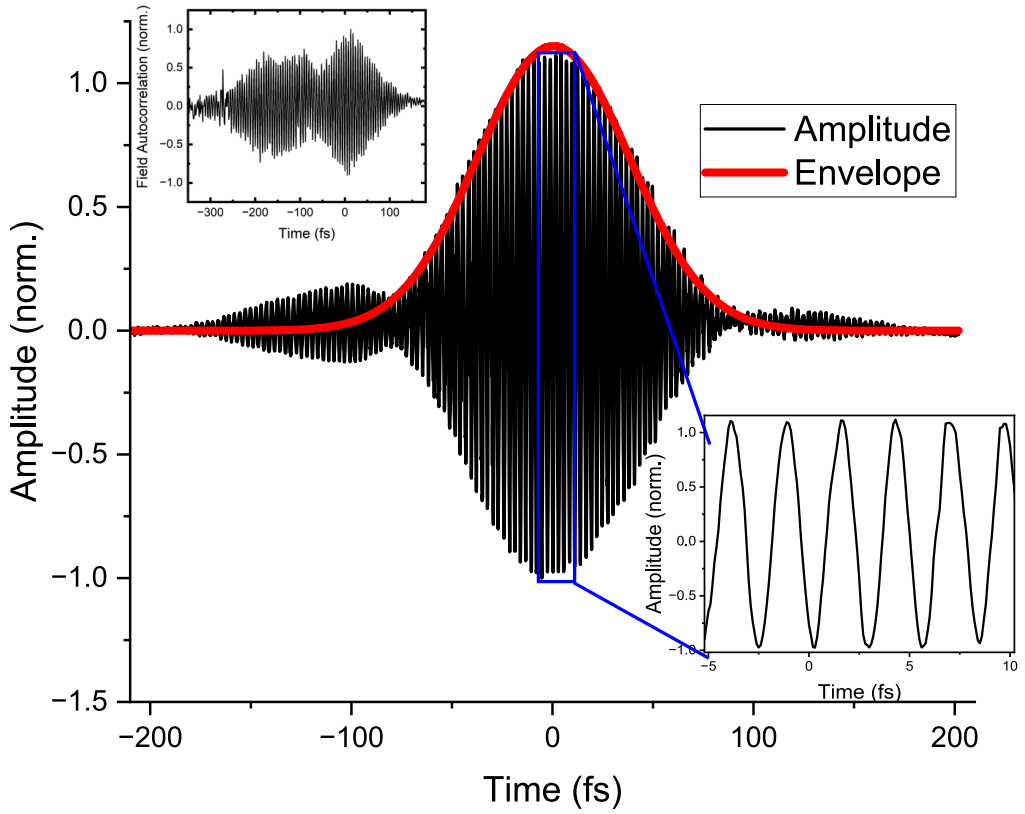

Fig. 3 Maximum amplitude of the THz time-domain signal as a function of the time delay between the fundamental and its second harmonic, i.e., their relative phase delay. The inset at the bottom right is a zoom into the THz signal, resolving its oscillations depending on the phase delay. The top left inset displays the corresponding optical field autocorrelation between the fundamental and its second harmonic

of the second harmonic beam. The changes of polarity are evident as oscillations of the THz amplitude as illustrated in the inset of Fig. 2. Consequently, the delay-dependent THz signal shown in Fig. 3 closely resembles an optical field autocorrelation. For comparison, the inset of Fig. 3 shows the corresponding optical field autocorrelation of the fundamental and its second harmonic, measured with a GaInAs photodiode. This similarity highlights the underlying mechanism of THz emission: an interference effect between the fundamental beam and its second harmonic, resulting in an asymmetric carrier distribution in momentum space. Therefore, fitting an envelope to the measurement data in Fig. 3 provides a good estimate for the pulse length of the second harmonic. We find a full width at half maximum (FWHM) of the envelope of 89 fs corresponding to a Gaussian pulse length of 63 fs.

To evaluate the emission strength of the two-color excited Ge emitter, we compare it to several established THz sources under identical excitation and electro-optic detection conditions. For the two-color excitation, the fundamental pulse at 1590 nm with a pulse energy of 1 µJ is combined with its second harmonic at 795 nm with a pulse energy of 300 nJ. For optical rectification in the 350 µm-thick GaP crystal, only the fundamental pulse (1590 nm, 1 µJ) is used, with the second harmonic blocked. In contrast, for optical rectification in the 500 µm-thick ZnTe crystal and excitation of the commercially available biased GaAs photoconductive antenna (TeraSED3), only the second harmonic (795 nm, 300 nJ) is used, with the fundamental blocked.

As shown in Fig. 4, the peak electric field emitted from the Ge emitter reaches approximately 33 V/cm. The field strengths are estimated based on the differential signal of the photodiodes, considering the electro-optic coefficient and the thickness of the ZnTe detection crystal, following the method described in Ref. [30]. Although the field from the Ge emitter is lower than that achieved via optical rectification in ZnTe (280 V/cm) and GaP (125 V/cm), as well as the biased GaAs photoconductive antenna (240 V/cm), it is generated entirely without external bias or phase-matching constraints. In contrast to the aforementioned emitters, the Ge-based source should offer intrinsically broadband, gapless THz emission, which is an important advantage for applications demanding wide and gapless spectral coverage.

To evaluate the full bandwidth of our THz emission, a 100 µm-thick GaP crystal is used for electro-optical sampling instead of a 500 µm-thick ZnTe crystal, which limits the bandwidth of the THz emission to about 3.5 THz. The GaP crystal should be able to detect THz emission up to its reststrahlen band at around 8 THz [31–33]. Using the thinner GaP crystal significantly alters the detected THz signal in the time domain as shown in Fig. 5a. Notably, the main peak of the detected THz waveform becomes narrower, reaching a FWHM of just 110 fs. Simultaneously, the THz transient becomes more asymmetric. The asymmetry ratio between the amplitudes of the two largest opposite-sign half-cycles is 3.34:1, a feature desirable in many applications, including sub-cycle THz scanning tunneling microscopy [10, 34–36]. Fourier transformation provides us with the frequency range that reveals a very broadband THz emission up to the reststrahlen band of the GaP crystal at about 8 THz with a maximum at about 2 THz. This highlights the excellence of Ge as a THz emitter, as the bandwidth is not limited by material absorption. In addition, a different group velocity of THz and optical pulses in the Ge crystal is not of particular relevance, as the penetration depth of the second

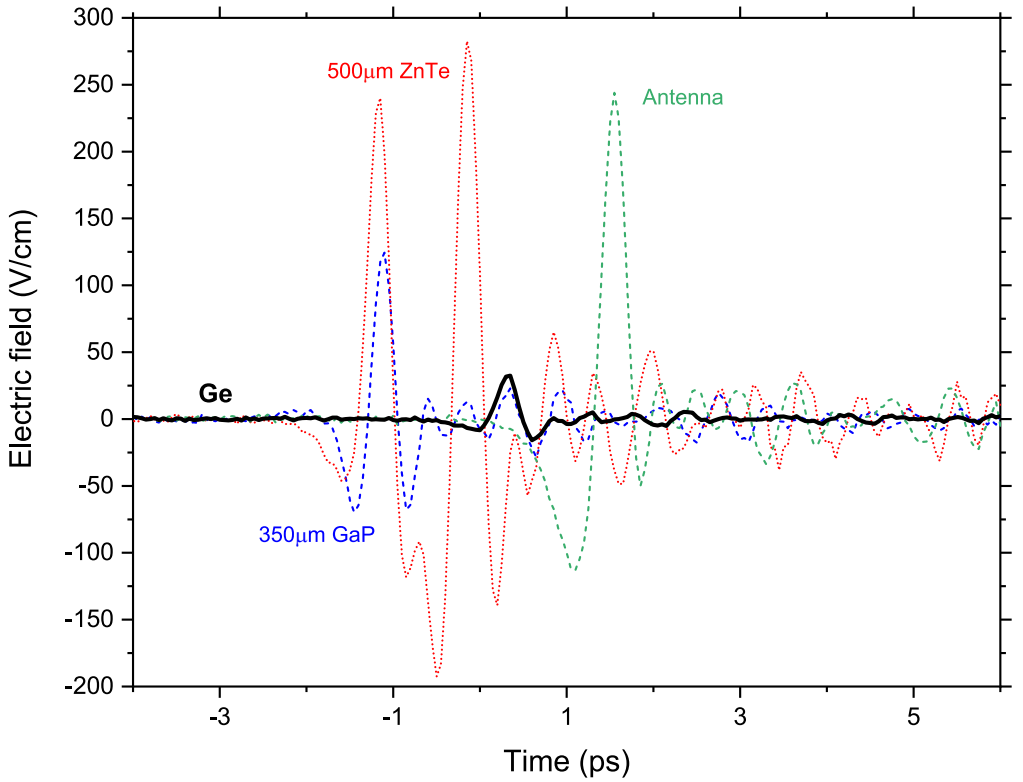

Fig. 4 THz pulses emitted from various sources under identical excitation and electro-optic detection. Compared are the bulk Ge emitter after two-color excitation (black), optical rectification in ZnTe (red) and GaP (blue), and a biased GaAs photoconductive antenna (green)

harmonic is very shallow with only about one micrometer [25]. As depicted in Fig. 5b, the detected THz spectrum abruptly cuts off near 8 THz, indicating that the emitted pulse likely extends beyond the detection range of the GaP crystal [32, 33]. Because Ge is centrosymmetric and lacks polar optical phonon modes in the THz range, it imposes no intrinsic spectral gaps. In contrast, optical rectification in non-centrosymmetric

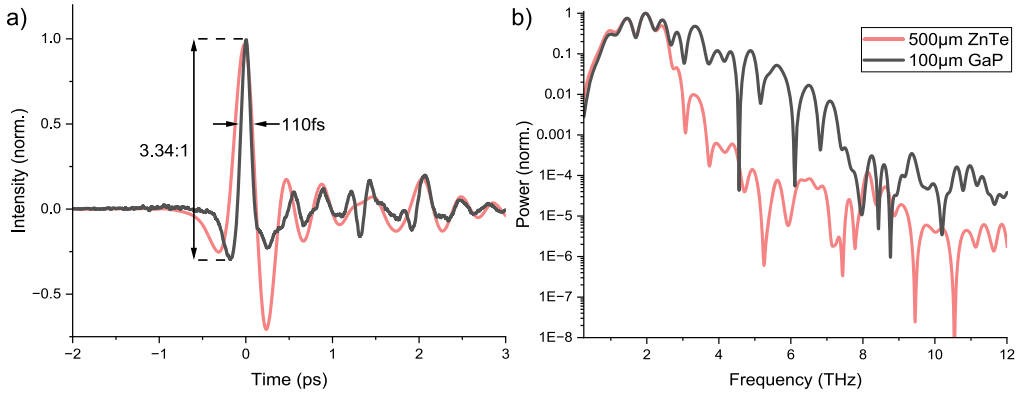

Fig. 5 Time domain (**a**) and frequency spectrum (**b**) of the detected THz pulse, utilizing a 100 μm-thick GaP (black) crystal as well as a 500 μm-thick ZnTe crystal (red). Detection with the thinner GaP crystal reveals a highly asymmetric THz transient and a broadband THz emission up to the GaP crystal's detection limit at about 8 THz

materials like ZnTe and GaP is inherently limited by their phonon absorption (at around 4 THz for ZnTe and 8 THz for GaP). Therefore, Ge enables truly gapless THz emission, even though the bandwidth we detect is currently constrained by the electro-optic response of the sampling crystal. Future integration of more advanced broadband detection techniques, such as air-biased coherent detection [37, 38] or the use of a THz Michelson interferometer [39, 40] could reveal spectral components beyond the 8 THz detection limit of GaP. This implies that even broader THz emission is possible, especially when combined with shorter laser pulses and improved detection. The resulting spectra could approach those generated via air plasma using high-energy amplified laser systems [13, 41, 42]. Our approach, however, operates with much lower pulse energies, making it feasible to use oscillators or fiber lasers without the need for cost-intensive amplifier systems. Notably, there is no minimum pulse energy threshold for THz generation, with the lower limit being the energy needed to produce the second harmonic. At reduced optical pulse energies, the THz field amplitude scales linearly with the fundamental excitation power and follows the square root of the second harmonic excitation power [25]. However, in contrast to that earlier study on two-color excitation in Ge, our work achieves a substantially broader detectable THz bandwidth, extending up to 8 THz. This enhancement is primarily enabled by the use of a thinner electro-optic sampling crystal (100 μm GaP instead of a thicker ZnTe crystal) and significantly shorter excitation and detection pulses ($<$100 fs compared to 150 fs in Ref. [25]). As a result, we demonstrate genuinely gapless and broadband THz emission from Ge, with the observed cutoff near 8 THz limited only by the detection crystal's response. This not only extends the spectral range reported in prior work but also reveals the highly asymmetric temporal field profile of the emitted THz pulses—a characteristic that is particularly beneficial for sub-cycle applications.

The potential limitations in repetition rate for Ge due to its inherently long carrier lifetimes is readily overcome by intentionally introducing recombination centers through impurity implantation [18]. This should enable using common commercially available repetition rates around 80 MHz or even beyond in the GHz range.

Switching to an epitaxially grown Ge/SiGe quantum well (QW) heterostructure under the same two-color excitation scheme demonstrates that the THz emission mechanism is not confined to bulk Ge but is also effective in engineered low-dimensional systems. This underlines the robustness and generality of the emission process and supports its potential for integration into heterostructure-based optoelectronic platforms. The THz pulses emitted from the sample, consisting of 50 repetitions of Ge QWs separated by Si0.15Ge0.85 barriers, are shown in Fig. 6. Remarkably, the time-domain waveform closely resembles those obtained from bulk Ge (cf. Figure 2). As in the bulk case, the polarity and amplitude of the emitted THz field are coherently controlled by adjusting the relative phase between the fundamental and its second harmonic, indicating that the same underlying nonlinear photoexcitation mechanism governs the emission. However, the emitted THz amplitude from the QW sample is reduced by a factor of approximately 4 to 5 compared to bulk Ge. This reduction is primarily attributed to the absorption of the second harmonic within the SiGe barriers, which decreases the effective excitation intensity reaching the Ge wells. Additionally, THz

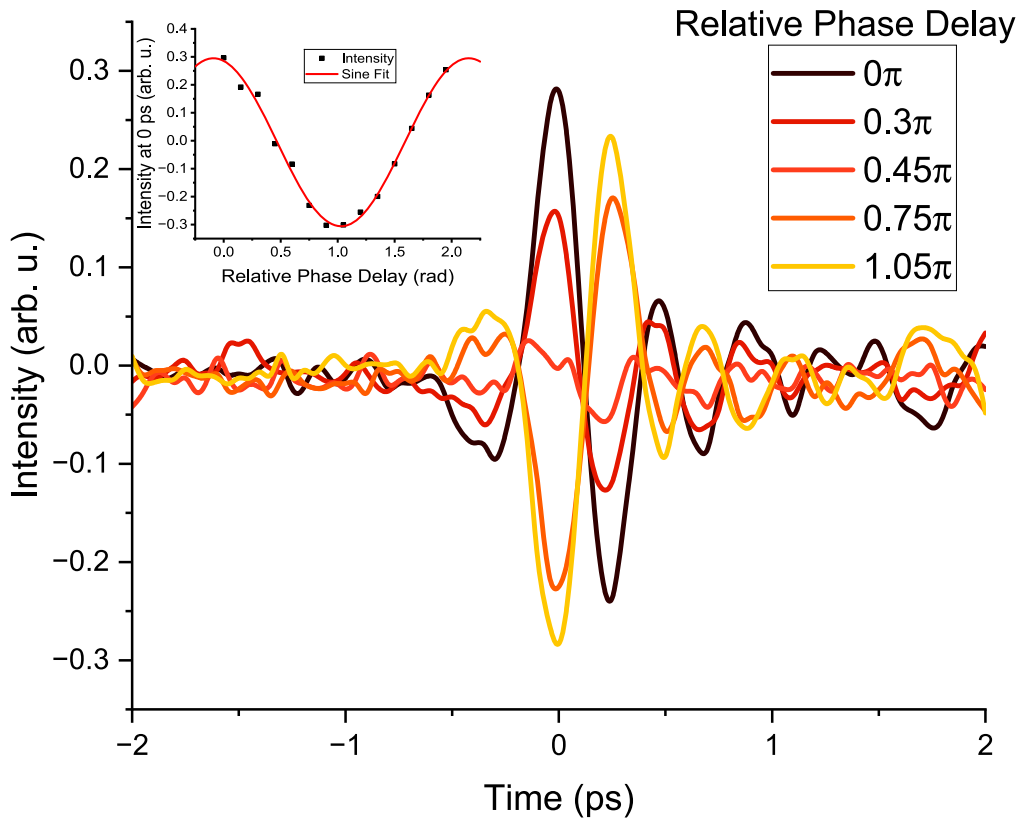

Fig. 6 Time evolution of the detected THz pulse's electric field amplitude for various phase shifts (relative path delays) between the fundamental optical pulse and its second harmonic in the Ge QW sample

re-absorption by photoexcited carriers in the barrier regions may further attenuate the signal. Overall, the ability to generate phase-controllable THz pulses from a Ge/SiGe heterostructure without relying on structural inversion asymmetry further reinforces the general applicability of the two-color excitation scheme. It also opens up avenues for future integration into quantum-engineered materials and device architectures.

4 Conclusion

In conclusion, we demonstrate gapless, broadband THz emission up to 8 THz from pure bulk Ge as well as Ge QWs by generating coherently controlled quantum interference currents using 100 fs optical pulses around 1590 nm and their second harmonic. This all-optical approach utilizes the telecom wavelength and paves the way for generating broadband and gapless THz pulses even with comparatively inexpensive fiber lasers.

Acknowledgements Michael R. Zengel acknowledges financial support from the German Academic Exchange Service (DAAD) under the RISE program. The work was supported by the European Regional Development Fund (ERDF) within the innovation laboratory process diagnostics under contract 21031934. Sangam Chatterjee acknowledges funding through the State of Hesse Landes-Offensive zur Entwicklung Wissenschaftlich-ökonomischer Exzellenz (LOEWE) by the Transfer-Professur "Hochtechnologiematerialien".

Author Contributions S.C. conceived the experiment. M.R.Z. built the experimental setup together with D.A., M.S., R.S.R., and K.B.. D.A., M.R.Z., R.S.R., and K.B. prepared the figures of the manuscript and analyzed the data. M.S. wrote the main manuscript text. All authors reviewed the manuscript.

Funding Open Access funding enabled and organized by Projekt DEAL.

Data Availability Data sets generated during the current study are available from the corresponding author on reasonable request.

Declarations

Competing Interests The authors declare no competing interests.

References

1. Jepsen, P.U., Cooke, D.G., Koch, M.: Terahertz spectroscopy and imaging–modern techniques and applications. Laser & Photonics Reviews. **5**(1), 124–166 (2011)
2. Ulbricht, R., Hendry, E., Shan, J., Heinz, T.F., Bonn, M.: Carrier dynamics in semiconductors studied with time-resolved terahertz spectroscopy. Reviews of Modern Physics. **83**(2), 543 (2011)
3. Dietz, R.J., Vieweg, N., Puppe, T., Zach, A., Globisch, B., Göbel, T., Leisching, P., Schell, M.: All fiber-coupled thz-tds system with khz measurement rate based on electronically controlled optical sampling. Optics letters. **39**(22), 6482–6485 (2014)
4. Kohlhaas, R.B., Breuer, S., Mutschall, S., Kehrt, M., Nellen, S., Liebermeister, L., Schell, M., Globisch, B.: Ultrabroadband terahertz time-domain spectroscopy using iii-v photoconductive membranes on silicon. Optics Express. **30**(13), 23896–23908 (2022)
5. Koch, M., Mittleman, D.M., Ornik, J., Castro-Camus, E.: Terahertz time-domain spectroscopy. Nature Reviews Methods Primers. **3**(1), 48 (2023)
6. Hoffmann, M.C., Yeh, K.-L., Hebling, J., Nelson, K.A.: Efficient terahertz generation by optical rectification at 1035 nm. Optics Express. **15**(18), 11706–11713 (2007)
7. Fülöp, J., Pálfalvi, L., Almási, G., Hebling, J.: Design of high-energy terahertz sources based on optical rectification. Optics express. **18**(12), 12311–12327 (2010)
8. Fülöp, J., Pálfalvi, L., Klingebiel, S., Almási, G., Krausz, F., Karsch, S., Hebling, J.: Generation of sub-mj terahertz pulses by optical rectification. Optics letters. **37**(4), 557–559 (2012)
9. Feng, K., Streyer, W., Zhong, Y., Hoffman, A., Wasserman, D.: Photonic materials, structures and devices for reststrahlen optics. Optics express. **23**(24), 1418–1433 (2015)
10. Meineke, C., Prager, M., Hayes, J., Wen, Q., Kastner, L.Z., Schuh, D., Fritsch, K., Pronin, O., Stein, M., Schäfer, F., *et al.*: Scalable high-repetition-rate sub-half-cycle terahertz pulses from spatially indirect interband transitions. Light: Science & Applications. **11**(1), 151 (2022)
11. Cook, D., Hochstrasser, R.: Intense terahertz pulses by four-wave rectification in air. Optics letters. **25**(16), 1210–1212 (2000)
12. Kress, M., Löffler, T., Eden, S., Thomson, M., Roskos, H.G.: Terahertz-pulse generation by photoionization of air with laser pulses composed of both fundamental and second-harmonic waves. Optics letters. **29**(10), 1120–1122 (2004)

13. Thomson, M.D., Blank, V., Roskos, H.G.: Terahertz white-light pulses from an air plasma photo-induced by incommensurate two-color optical fields. Optics Express. **18**(22), 23173–23182 (2010)
14. Clough, B., Dai, J., Zhang, X.-C.: Laser air photonics: beyond the terahertz gap. Materials Today. **15**(1-2), 50–58 (2012)
15. Seifert, T., Jaiswal, S., Martens, U., Hannegan, J., Braun, L., Maldonado, P., Freimuth, F., Kronenberg, A., Henrizi, J., Radu, I., *et al.*: Efficient metallic spintronic emitters of ultrabroadband terahertz radiation. Nature photonics. **10**(7), 483–488 (2016)
16. Papaioannou, E.T., Beigang, R.: Thz spintronic emitters: a review on achievements and future challenges. Nanophotonics. **10**(4), 1243–1257 (2021)
17. Singh, A., Pashkin, A., Winnerl, S., Helm, M., Schneider, H.: Gapless broadband terahertz emission from a germanium photoconductive emitter. Acs Photonics. **5**(7), 2718–2723 (2018)
18. Singh, A., Pashkin, A., Winnerl, S., Welsch, M., Beckh, C., Sulzer, P., Leitenstorfer, A., Helm, M., Schneider, H.: Up to 70 thz bandwidth from an implanted ge photoconductive antenna excited by a femtosecond er: fibre laser. Light: Science & Applications. **9**(1), 30 (2020)
19. Park, S.-G., Choi, Y., Oh, Y.-J., Jeong, K.-H.: Terahertz photoconductive antenna with metal nanoislands. Optics express. **20**(23), 25530–25535 (2012)
20. Burford, N.M., El-Shenawee, M.O.: Review of terahertz photoconductive antenna technology. Optical Engineering. **56**(1), 010901–010901 (2017)
21. Atanasov, R., Haché, A., Hughes, J., Van Driel, H., Sipe, J.: Coherent control of photocurrent generation in bulk semiconductors. Physical review letters. **76**(10), 1703 (1996)
22. Haché, A., Kostoulas, Y., Atanasov, R., Hughes, J., Sipe, J., Van Driel, H.: Observation of coherently controlled photocurrent in unbiased, bulk gaas. Physical Review Letters. **78**(2), 306 (1997)
23. Côté, D., Fraser, J., DeCamp, M., Bucksbaum, P.H., Van Driel, H.: Thz emission from coherently controlled photocurrents in gaas. Applied Physics Letters. **75**(25), 3959–3961 (1999)
24. Costa, L., Betz, M., Spasenović, M., Bristow, A.D., Van Driel, H.M.: All-optical injection of ballistic electrical currents in unbiased silicon. Nature Physics. **3**(9), 632–635 (2007)
25. Spasenović, M., Betz, M., Costa, L., Driel, H.M.: All-optical coherent control of electrical currents in centrosymmetric semiconductors. Physical Review B. **77**(8), 085201 (2008)
26. Sames, C., Ménard, J.-M., Betz, M., Smirl, A.L., Driel, H.M.: All-optical coherently controlled terahertz ac charge currents from excitons in semiconductors. Physical Review B. **79**(4), 045208 (2009)
27. Lü, Z., Zhang, D., Zhou, Z., Sun, L., Zhao, Z., Yuan, J.: Coherently controlled terahertz source for a time domain spectroscopy system via injection current in bulk znse. Applied Optics. **51**(5), 676–679 (2012)
28. Gongora, J.T., Peters, L., Tunesi, J., Cecconi, V., Clerici, M., Pasquazi, A., Peccianti, M.: All-optical two-color terahertz emission from quasi-2d nonlinear surfaces. Physical Review Letters. **125**(26), 263901 (2020)
29. Lange, C., Isella, G., Chrastina, D., Pezzoli, F., Köster, N.S., Woscholski, R., Chatterjee, S.: Spin band-gap renormalization and hole spin dynamics in ge/sige quantum wells. Phys. Rev. B. **85**, 241303 (2012) https://doi.org/10.1103/PhysRevB.85.241303
30. Sitnikov, D., Romashevskiy, S., Ovchinnikov, A., Chefonov, O., Savel'ev, A., Agranat, M.: Estimation of thz field strength by an electro-optic sampling technique using arbitrary long gating pulses. Laser Physics Letters. **16**(11), 115302 (2019)
31. Leitenstorfer, A., Moskalenko, A.S., Kampfrath, T., Kono, J., Castro-Camus, E., Peng, K., Qureshi, N., Turchinovich, D., Tanaka, K., Markelz, A.G., Havenith, M., Hough, C., Joyce, H.J., Padilla, W.J., Zhou, B., Kim, K.-Y., Zhang, X.-C., Jepsen, P.U., Dhillon, S., Vitiello, M., Linfield, E., Davies, A.G., Hoffmann, M.C., Lewis, R., Tonouchi, M., Klarskov, P., Seifert, T.S., Gerasimenko, Y.A., Mihailovic, D., Huber, R., Boland, J.L., Mitrofanov, O., Dean, P., Ellison, B.N., Huggard, P.G., Rea, S.P., Walker, C., Leisawitz, D.T., Gao, J.R., Li, C., Chen, Q., Valušis, G., Wallace, V.P., Pickwell-MacPherson, E., Shang, X., Hesler, J., Ridler, N., Renaud, C.C., Kallfass, I., Nagatsuma, T., Zeitler, J.A., Arnone, D., Johnston, M.B., Cunningham, J.: The 2023 terahertz science and technology roadmap. Journal of Physics D: Applied Physics. **56**(22), 223001 (2023) https://doi.org/10.1088/1361-6463/acbe4c
32. Aoki, K., Savolainen, J., Havenith, M.: Broadband terahertz pulse generation by optical rectification in GaP crystals. Applied Physics Letters. **110**(20), 201103 (2017) https://doi.org/10.1063/1.4983371
33. Vugmeyster, I., Whitaker, J., Merlin, R.: Gap based terahertz time-domain spectrometer optimized for the 5-8 thz range. Applied Physics Letters. **101**(18) (2012)

34. Cocker, T.L., Jelic, V., Gupta, M., Molesky, S.J., Burgess, J.A., Reyes, G.D.L., Titova, L.V., Tsui, Y.Y., Freeman, M.R., Hegmann, F.A.: An ultrafast terahertz scanning tunnelling microscope. Nature Photonics. **7**(8), 620–625 (2013)
35. Cocker, T.L., Peller, D., Yu, P., Repp, J., Huber, R.: Tracking the ultrafast motion of a single molecule by femtosecond orbital imaging. Nature. **539**(7628), 263–267 (2016)
36. Yoshioka, K., Katayama, I., Minami, Y., Kitajima, M., Yoshida, S., Shigekawa, H., Takeda, J.: Real-space coherent manipulation of electrons in a single tunnel junction by single-cycle terahertz electric fields. Nature photonics. **10**(12), 762–765 (2016)
37. Ho, I.-C., Guo, X., Zhang, X.-C.: Design and performance of reflective terahertz air-biased-coherent-detection for time-domain spectroscopy. Optics express. **18**(3), 2872–2883 (2010)
38. Wang, T., Iwaszczuk, K., Wrisberg, E.A., Denning, E.V., Jepsen, P.U.: Linearity of air-biased coherent detection for terahertz time-domain spectroscopy. Journal of Infrared, Millimeter, and Terahertz Waves. **37**(6), 592–604 (2016)
39. Eisele, H., Naftaly, M., Fletcher, J.R.: A simple interferometer for the characterization of sources at terahertz frequencies. Measurement Science and Technology. **18**(8), 2623 (2007)
40. Wichmann, M., Stein, M., Rahimi-Iman, A., Koch, S.W., Koch, M.: Interferometric characterization of a semiconductor disk laser driven terahertz source. Journal of Infrared, Millimeter, and Terahertz Waves. **35**(6), 503–508 (2014)
41. Fan, Z., Lu, C., Liu, Y.: Tunable broadband thz emission from air plasma pumped by femtosecond pulses composed of a fundamental frequency with its detuned second harmonic. Optics Communications. **505**, 127532 (2022)
42. Matsubara, E., Nagai, M., Ashida, M.: Ultrabroadband coherent electric field from far infrared to 200 thz using air plasma induced by 10 fs pulses. Applied Physics Letters. **101**(1) (2012)

III - Exciton Formation dynamics in (Ga,In)As multi quantum wells, Ref. [190]

D. Anders, F. Dobener, C. Fuchs, K. Volz, S. Chatterjee, M. Stein

Abstract

We investigate the ultrafast dynamics of exciton formation in (Ga,In)As quantum wells using optical pump-terahertz probe spectroscopy, complemented by time-resolved photoluminescence. Terahertz spectroscopy directly probes intraexcitonic transitions and thus, in principle, distinguishes between unbound electron-hole plasma and bound exciton populations. At low excitation densities, this separation is effective: the Drude response of the electron-hole plasma remains spectrally distinct from narrow intraexcitonic resonances. However, at higher excitation densities, spectral broadening and overlap obscure this distinction.
Following low-density nonresonant excitation, we initially observe a pure Drude-like plasma response that gradually transitions into an intraexcitonic resonance. In contrast, at higher excitation densities, conventional analysis based on the Drude-Lorentz model suggests questionably high exciton fractions up to 32% immediately after excitation. It remains uncertain whether these fractions represent genuine instantaneous exciton formation or arise from spectral overlap and analytical ambiguity. To resolve this, we introduce a differential probing technique utilizing exciton ionization induced by strong THz fields. By comparing responses obtained at high and low THz field strengths, we isolate the exciton contribution from the pure plasma contributions. This approach reveals intrinsic exciton formation dynamics governed by two characteristic timescales: a fast component in the vicinity of 10 ps and a slower process around 250 ps. Notably, these timescales remain largely independent of excitation density, contrasting sharply with the strong density dependence suggested by conventional methods.
Our results establish a robust method to disentangle exciton and plasma dynamics, providing clearer insight into exciton formation under nonresonant excitation in semiconductor quantum wells.

Conclusion

We investigated the THz response of (Ga,In)As/GaAs multiple quantum wells following nonresonant optical excitation. Immediately after excitation, the system exhibits a characteristic Drude-like response from an unbound electron–hole plasma, which gradually evolves into a finite $1s$ exciton population. Exciton formation proceeds on two distinct timescales: a fast component within the first few tens of picoseconds and a slower formation phase extending over several hundred picoseconds. Interestingly, while conventional analyses suggest a strong dependence of these timescales on excitation density, our refined methodology reveals that exciton formation dynamics are rather independent of both the excitation density and excess energy within the investigated range. This conclusion is enabled by our new approach that systematically compares THz responses at weak and strong probe field strengths. By exploiting field-induced exciton ionization, we isolate the pure excitonic signal from the overlapping plasma background, even at higher excitation densities where traditional analysis struggles. Our results resolve longstanding ambiguities in the interpretation of time-resolved THz spectroscopy and demonstrate a robust, generalizable framework for disentangling exciton and plasma dynamics. This methodology offers clear insight into the intrinsic exciton formation process and is broadly

applicable to the study of ultrafast many-body phenomena in semiconductor quantum structures.

Contribution

The experimental setup was designed by me in collaboration with M.S. and S.C., with the measurement software provided by F.D. The MQW samples were provided by C.F. and K.V. I performed the experiments in collaboration with M.S., and analyzed the experimental data. The initial manuscript was written by me and the final version was revised together with S.C. and M.S. All figures included in the final manuscript were prepared by me.

Exciton formation dynamics in (Ga,In)As quantum wells

D. Anders,[1] F. Dobener,[1] C. Fuchs,[2] K. Volz,[2] S. Chatterjee,[1] and M. Stein[1,*]

[1] *Institute of Experimental Physics I and Center for Materials Research (LaMa), Justus-Liebig-University Giessen, Heinrich-Buff-Ring 16, D-35392 Giessen, Germany*

[2] *Structure & Technology Research Laboratory (WZMW), Philipps-University Marburg, Hans-Meerwein-Straße 6, D-35032 Marburg, Germany*

(Dated: October 28, 2025)

We investigate the ultrafast dynamics of exciton formation in (Ga,In)As quantum wells using optical pump-terahertz probe spectroscopy, complemented by time-resolved photoluminescence. Terahertz spectroscopy directly probes intraexcitonic transitions and thus, in principle, distinguishes between unbound electron-hole plasma and Coulomb-bound exciton populations. At low excitation densities, this separation is effective: the Drude response of the electron-hole plasma remains spectrally distinct from narrow intraexcitonic resonances. However, at higher excitation densities, spectral broadening and overlap obscure this distinction.

Following low-density nonresonant excitation, we initially observe a pure Drude-like plasma response that gradually transitions into an intraexcitonic resonance. In contrast, at higher excitation densities, conventional analysis based on the Drude-Lorentz model suggests questionably high exciton fractions up to 32% immediately after excitation. It remains uncertain whether these fractions represent genuine instantaneous exciton formation or arise from spectral overlap and analytical ambiguity. To resolve this, we introduce a differential probing technique utilizing exciton ionization induced by strong THz fields. By comparing responses obtained at high and low THz field strengths, we isolate the exciton contribution from the pure plasma contributions. This approach reveals intrinsic exciton formation dynamics governed by two characteristic timescales: a fast component in the vicinity of 10 ps and a slower process around 250 ps. Notably, these timescales remain largely independent of excitation density, contrasting sharply with the strong density dependence suggested by conventional methods.

Our results establish a robust method to disentangle exciton and plasma dynamics, providing clearer insight into exciton formation under nonresonant excitation in semiconductor quantum wells.

I. INTRODUCTION

The widespread availability of pulsed and ultrafast laser systems has spurred vast research efforts to identify quasiparticle dynamics in condensed matter systems, such as studying charge carriers in semiconductors and their heterostructures [1–3]. Among these, the formation dynamics of excitons, i.e., a quasiparticle many-body state consisting of an electron and a hole stabilized by Coulomb attraction, has often been controversially discussed [4, 5]. The prominent spectral features in the vicinity of the band gap energy associated with excitons dominate the linear optical response in many high-quality semiconductors ranging from bulk inorganic compound materials or organic semiconductors to quantum structures and novel materials including 2D materials and layered van der Waals heterostructures. Traditionally, excitons and their dynamics have been investigated primarily by time-resolved photoluminescence (TRPL) spectroscopy [6–12]. However, photoluminescence spectroscopy inherently accesses only bright excitons, i.e., those with a center-of-mass momentum close to zero. This limits its ability to capture the entire exciton population and complicates the interpretation of formation dynamics[5, 13]. Consequently, the reported exciton formation times extracted from TRPL spectroscopy on GaAs-based quantum well structures vary by more than one order of magnitude from less than 20 ps [6, 7, 9–11] to more than 200 ps [4, 14]. Later, stringent theoretical analysis has revealed that the sources of emission at the 1s exciton energy are not limited to exciton population decay [15]. Subsequently, these theoretical findings have been substantiated experimentally [16, 17]. Optical pump-terahertz probe (OPTP) spectroscopy has since been proposed as a more direct and unambiguous method to investigate exciton formation[5, 18, 19]. THz pulses directly probe intraexcitonic transitions and provide distinct signatures of Coulomb-bound excitons, such as the 1s-2p absorption resonance, which are absent in the Drude-like response of unbound electron-hole plasmas. Moreover, terahertz spectroscopy is sensitive to excitons of any center-of-mass momentum, making it a versatile tool for tracking exciton populations[5, 19–21]. However, despite these methodological advantages, OPTP spectroscopy has not provided a consistent picture of the exciton formation dynamics in GaAs-based quantum wells after nonresonant excitation either. Reported results span a broad range: some studies observe relatively slow exciton formation over several hundred picoseconds [17, 22], while others report ultrafast formation, with up to 40% of the exciton population emerging within just a few picoseconds [20, 23], and yet others report intermediate timescales [24].

In this work, we introduce a new approach to disentan-

* markus.stein@exp1.physik.uni-giessen.de

gle Coulomb-bound exciton and unbound electron-hole plasma contributions in time-resolved THz spectroscopy of high-quality (Ga,In)As/GaAs multiple quantum wells after nonresonant excitation. By systematically varying the field strength of the probing THz pulse, we exploit field-induced exciton ionization at high THz fields to selectively switch off the excitonic response and compare these measurements with low-field conditions that preserve the exciton population. This differential probing technique isolates the exciton response from the plasma background, even at high excitation densities, where, in conventional analysis, spectral overlap typically obscures the distinction between excitons and free carriers.
Using this method, we uncover intrinsic exciton formation dynamics governed by two distinct timescales: a fast component of approximately 10 ps and a slower process of about ~ 250 ps, both largely independent of excitation density. Our results resolve long-standing ambiguities related to apparently instantaneous exciton formation reported in earlier OPTP studies and establish a robust framework for probing ultrafast exciton formation dynamics in semiconductor quantum structures.

II. EXPERIMENTAL DETAILS

The samples under investigation are (Ga,In)As MQW structures grown by metal organic vapor phase epitaxy on a GaAs substrate. The primary MQW structure (**1**) consists of 50 periods of 1.35 nm GaAs, 8.65 nm (Ga,In)As, 1.35 nm GaAs and 8.65 nm Ga(As,P); In and P concentrations are 9.5% and 22%, respectively; details of the sample structure are given elsewhere [25]. The second sample (**2**) also consists of 50 periods of different layer widths: 4.6 nm GaAs, 7.6 nm (Ga,In)As, 4.6 nm GaAs, and 19.4 nm Ga(As,P); the In and P concentrations are 5.8% and 5.3%, respectively [22]. All experiments are performed under cryogenic conditions at a lattice temperature of 6 K to minimize broadening and phonon scattering. The OPTP setup utilizes a 5 kHz repetition rate regenerative amplifier that generates 50 fs pulses centered at 800 nm. These pulses are split into two paths using a beam splitter. One part drives an optical parametric amplifier that generates the optical pump at a central wavelength of about 850 nm. After the light has passed a delay line, a grating pulse shaper finely adjusts the pulse to the desired wavelength and spectral width before exciting the sample. The second part of the regenerative-amplifier output is divided by another beam splitter. The largest part of the pulse is directed through a second delay line to a large-aperture GaAs antenna which delivers single-cycle THz pulses. An ellipsoidal mirror focuses the THz pulses onto the sample where they spatially overlap with the optical pump beam. Another ellipsoid relays the transmitted THz pulse onto a 500 µm-thick ZnTe crystal. The THz beam path is continuously purged with dry nitrogen gas to prevent spurious spectral signatures related to absorption by water

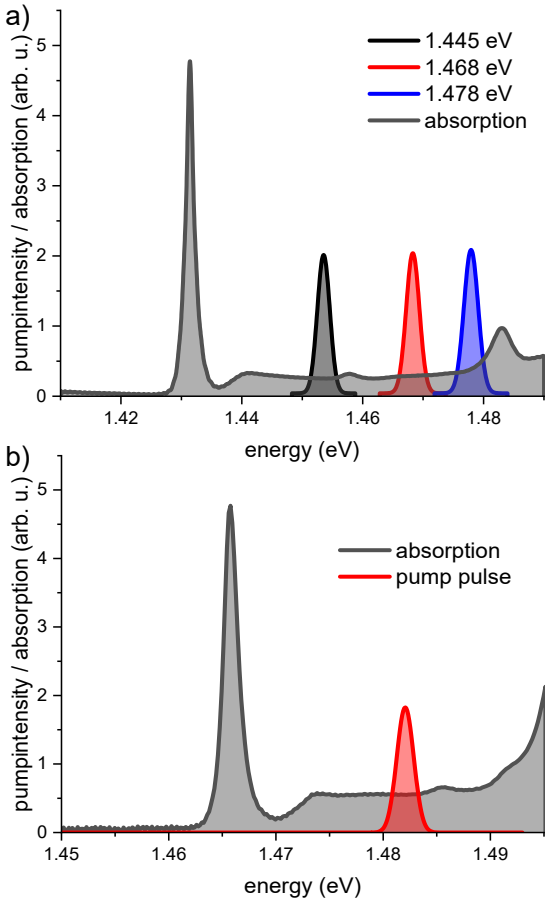

FIG. 1. a) Linear absorption spectrum of sample **1**, overlaid with the excitation pulses used for different excess energies. b) Absorption spectrum of sample **2** along with the corresponding excitation pulse.

vapor in the ambient atmosphere. The transient THz electric field is measured via electro-optic sampling using a third optical pulse. This configuration probes the sample's response in the energy range of 0.8 to 12.5 meV (0.2-3.0 THz). We sample 12 ps-long THz time traces and apply a Blackman-Nutall window function with a 2 ps slope before Fourier transforming the data into the frequency domain. By measuring the THz waveform of the unexcited sample, $E(t)$, and its excitation-induced change, $\Delta E(t)$, we calculate the complex dielectric function of the sample [26]:

$$\Delta\epsilon(\omega) = \frac{2ic_0\sqrt{\epsilon_r}}{\omega L}\left(\frac{\Delta E(\omega)}{E(\omega)}\right), \qquad (1)$$

where c_0 is the speed of light in vacuum, and ϵ_r the dielectric constant of the material.
TRPL measurements are performed using a typical streak camera setup in reflection geometry. Excitation

is provided by a Ti:sapphire laser oscillator that emits 100 fs pulses at a repetition rate of 78 MHz and a center wavelength of 850 nm. The excitation light is focused on a 40 µm diameter spot using a confocal beam path for both excitation and detection. The emitted PL signal is spectrally dispersed by a spectrograph equipped with a 122 $^{\text{lines}}/_{\text{mm}}$ grating, while temporal resolution is provided by a streak camera with an S20 cathode featuring an instrument response < 1 ps.

III. RESULTS

We excite the sample non-resonantly, i.e., at energies greater than the $1s$ exciton resonance to investigate the exciton formation dynamics. All photon densities are kept comparable around $4 \cdot 10^{12}\,\text{cm}^{-2}$, corresponding to $2 \cdot \text{I}_0$. The linear absorption spectra of the primary and secondary samples are shown in Figure 1 a) and b) together with the corresponding pulses for nonresonant excitation. The sample's response is probed by ∼1 ps-long THz pulses for different time delays Δt between the optical pump and the THz probe pulse. The delay is scanned from -5 ps, i.e., the probe impinges on the sample before the pump to 1 800 ps after the pump pulse maximum. The absorption and the change of the dielectric function show exclusively a Drude-like response during the first 3 ps. This clearly indicates the presence of a purely uncorrelated electron hole plasma (cf. Figure 2 a) and b) top row). Subsequently, the absorption in the energy range around 7 meV increases within the next few picoseconds. This is accompanied by an increase in the change of the dielectric function below 7 meV. Both are indicative for the incipient formation of an incoherent exciton population. Finally, a characteristic peak at 7.4 meV develops in the absorption spectrum on a time scale of several hundred picoseconds. This resonance is directly related to the typical zero crossing of a Lorentzian response in the real part of the dielectric function change (Figure 2 a) and b) bottom row). Both are unambiguous signatures for the presence of a $1s$ exciton population. The $1s$ exciton population coexists with the remanent electron-hole plasma that has not yet been converted into an exciton population as shown by the superimposed Drude response. We quantify the exciton formation dynamics by a phenomenological Drude-Lorentz model reproducing the experimental data. Fitting the change of the real part of the dielectric function $\Delta\epsilon(\omega)$ and the change in absorption $\Delta\alpha(\omega)$ simultaneously yields robust results. This model accounts for the two components and describes the excitation-induced changes of the complex dielectric function by the following equation[27, 28]:

$$\Delta\epsilon(\omega) = \frac{e^2}{L\epsilon_0\mu}\Bigg(\underbrace{\frac{f_{1s-2p}n_x}{\omega_{\text{res}}^2 - \omega^2 - i\omega\Delta_{\text{hom}}}}_{\textbf{I}\text{: Intraexcitonic absorption}} - \underbrace{\frac{n_{fc}}{\omega^2 + i\omega\Gamma}}_{\textbf{II}\text{: Drude response}} \Bigg) \tag{2}$$

The first part **I** corresponds to the Lorentzian lineshape of the intraexcitonic $1s$-$2p$ transition. Its oscillator strength is f_{1s-2p}, the resonance frequency ω_{res}, the exciton sheet density n_x, and the homogeneous linewidth Δ_{hom}. The second part **II** describes the Drude response characteristic for unbound carriers. It includes both the carrier sheet density n_{fc} and the carrier scattering rate Γ. Parameters that remain constant across all fits include the thickness of the sample L, the effective mass μ, the electron charge e, the vacuum permeability ϵ_0, and the intraexcitonic oscillator strength f_{1s-2p}. Thus, the Drude-Lorentz model provides direct access to the density of Coulomb-bound $1s$ excitons n_{x} as well as the density of free charge carriers n_{fc}, i.e., the electron-hole plasma, in the sample. Shortly after optical excitation, the exciton density rises rapidly from a pure electron-hole plasma, reaching approximately 30% to 50% of its maximum value within 40 ps. Around 600 ps after excitation, the exciton density peaks before gradually decreasing on a nanosecond timescale due to radiative and nonradiative recombination processes. A tri-exponential fit to the exciton density extracted at each time step using the Drude-Lorentz model function quantitatively describes the exciton formation and decay dynamics. The decay is well described by a single exponential term. However, the rise of exciton density requires two distinct exponential components to achieve an accurate representation, indicating the presence of multiple formation timescales. The extracted exciton densities are shown in Figure 2c) along with the tri-exponential fit. For comparison, a bi-exponential fit is also included, highlighting the necessity of incorporating both fast and slow rise components to fully capture the formation dynamics. The time constants reveal three characteristic regimes:

- a rapid exciton formation process with a time constant in the vicinity of 20 ps,
- a significantly slower formation process with a time constant around 300 ps,
- and a subsequent population decay with a time constant of about 1.5 ns.

A comparison of the results for the three different optical excitation energies of 1.445 eV (black), 1.468 eV (red), and 1.478 eV (blue) reveals a strikingly similar response. This suggests that the observed exciton formation dynamics are characteristic of nonresonant excitation conditions that are not too high in energy above the exciton resonance. The corresponding excess energies relative to the $1s$ exciton state are 14 meV, 37 meV, and 47 meV, respectively. Notably, the excess energy of 37 meV (1.468 eV excitation energy) is close to the optical phonon energy in (Ga,In)As of approximately 36 meV. Several theoretical works have proposed that exciton formation could be particularly efficient when the carrier excess energy matches the longitudinal optical (LO) phonon energy, as LO-phonon emission may provide an efficient

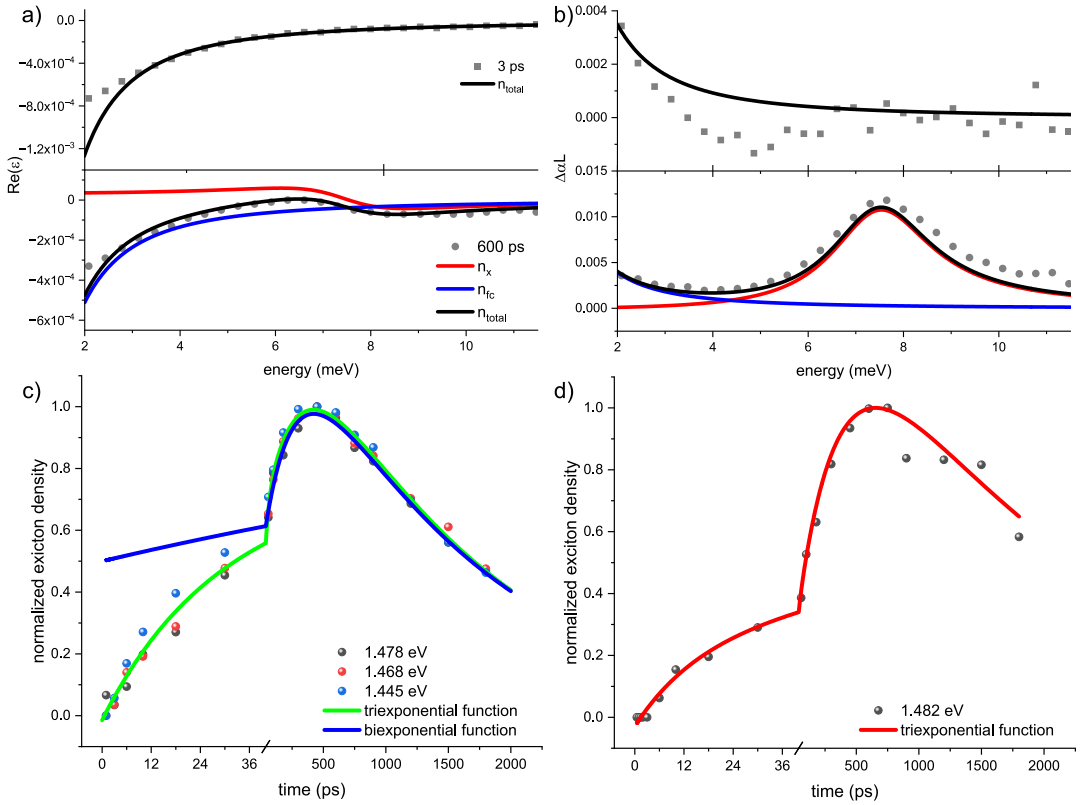

FIG. 2. Pump-induced change of the absorption $\Delta\alpha$L a) and real part of the dielectric function b) for delays of 3 ps (top) and 600 ps (bottom). The corresponding fits are shown as colored lines. The different contributions of free and bound electron-hole pairs are indicated for a delay of 600 ps. c) shows the normalized exciton densities with bi-exponential and tri-exponential fits for the different excitation energies for the first sample while d) shows the normalized exciton density for the control sample.

channel for energy relaxation and exciton binding [29–32]. However, in our experiments we do not find any clear evidence of enhanced exciton formation efficiency when the excitation excess energy coincides with the optical phonon energy. This observation is consistent with other experimental reports that found no correlation between exciton formation dynamics and an excess energy resonant with the LO-phonon energy [7].

The timescales of exciton formation in GaAs-based quantum structures have been extensively debated, with reported values ranging from less than 20 ps [6, 7, 9–11] to several hundred picoseconds [4, 14]. Our results indicate that both timescales coexist: an initial rapid exciton formation, followed by a slower secondary process. This dual-process behavior aligns qualitatively with previous observations by Kaindl et al. in GaAs quantum wells using OPTP spectroscopy [20, 23]. To assess the robustness of this behavior, we repeated the measurements on a second (Ga,In)As MQW sample (sample **2**), with different indium content and well width. In Figure 2d), we present data from the second sample excited at an energy of 1.482 eV (corresponding to an excess energy of 16 meV) at a comparable photon density. The exciton formation dynamics in this sample are similar to those observed in sample **1**, indicating that the dual-component formation process is largely independent of specific structural parameters, provided the exciton binding energy remains similar.

Since TRPL remains a common tool to assess exciton formation dynamics, we compared TRPL and OPTP measurements directly in Figure 3[4, 13, 33–35]. Under identical excitation conditions (1.458 eV, $2.75 \cdot I_0$), the PL signal reaches its maximum at the exciton resonance ($\sim$ 1.428 eV) within the experimental resolution ($\sim$39 ps), consistent with previous reports[16]. In contrast, the THz response reveals no evidence of a significant exciton population immediately after excitation. Instead, the intraexcitonic absorption at 7.4 meV peaks only after several hundred picoseconds. This discrepancy arises as PL emitted at an exciton resonance energy does not necessarily require a pre-existing population of excitons. As established in prior theoretical and experimental studies [15–17], PL at the exciton resonance can also originate from a pure electron–hole plasma without

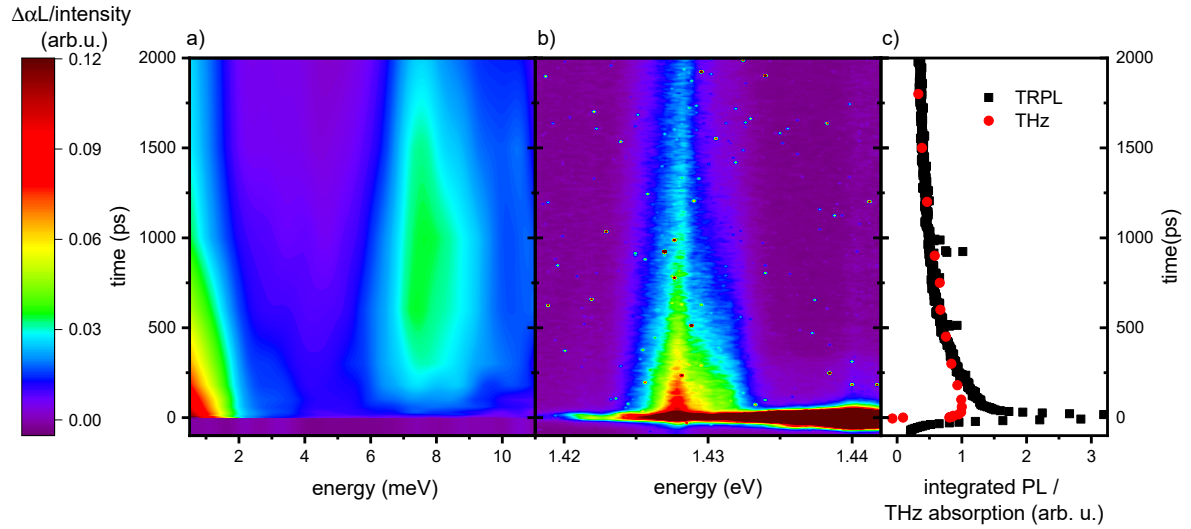

FIG. 3. a) Optical pump-terahertz probe absorption and b) time-resolved photoluminescence. An optical pulse with a central energy of 1.458 eV and a density of $2.75 \cdot \mathrm{I}_0$ is applied in both experiments. c) shows the integral of the plasma from a) and the corresponding integrated PL from b). THz data was integrated from 0.5 meV to 2 meV and PL data was integrated from 1.426 eV to 1.429 eV.

the formation of Coulomb-bound excitons. In contrast, THz absorption near 7 meV directly probes intraexcitonic transitions and thus provides a more definitive measure of the exciton population. Consequently, PL dynamics mainly reflect recombination of the entire carrier ensemble, while THz spectroscopy captures the actual build-up of Coulomb-bound excitons. As a result, the photoluminescence dynamics exhibit a much stronger correlation with the plasma dynamics of the OPTP spectroscopy than with its exciton formation process. This is illustrated in Figure 3c), where the temporal evolution of the electron–hole plasma extracted from the OPTP data is directly compared to the PL from the excitonic resonance. Apart from an initial PL overshoot caused by scattered excitation light, both signals exhibit nearly identical temporal dynamics.

We further explore exciton formation for systematically varied excitation densities using OPTP spectroscopy, since charge-carrier dynamics are highly density-dependent [21, 36, 37]. Figure 4 presents the pump-induced change in absorption, $\Delta\alpha L$, and the real part of the dielectric function for a pump energy of 1.468 eV at three different photon densities. While the overall spectral features of the THz response remain qualitatively similar across excitation densities, increasing the carrier density leads to markedly broader intraexcitonic absorption peaks and flatter dielectric function profiles [c.f. Figure 4 a)]. These trends are consistent with enhanced carrier–carrier scattering in a denser environment [27, 38]. The Drude-like plasma response increasingly overlaps with the spectral range of intraexcitonic transitions for the highest excitation density investigated ($1.08 \cdot 10^{13}$ photons/cm^2). This renders a clear separation of excitonic and plasma contributions challenging - even considering the sensitivity of OPTP spectroscopy. Consequently, the interpretation of the data is less unambiguous than for lower excitation densities. Explicitly, the analysis reveals higher exciton fractions almost instantaneously after excitation, even after carefully restricting the fitting parameters in the Drude-Lorentz model. For our data, we chose maximum width $\Delta_{\mathrm{hom,max}}$ of 6 meV and a minimum resonance energy $\omega_{\mathrm{res,min}}$ of 4.2 meV. The typical homogeneous line width $\Delta_{\mathrm{hom,max}}$ for low excitation densities are 2.5 meV and a broadening by a factor of about 2.4 is considerable. For the resonance energy $\omega_{\mathrm{res,min}}$ implies a decrease in exciton binding energy by 53%. We find these barriers to be a sound choice, since they still allow the fits to be in good agreement with the data while inhibiting any pathological values. Similarly to our results at higher excitation densities, evidence for an almost instantaneous emergence of a significant exciton population embedded within the broad Drude response has also been reported in the literature using OPTP spectroscopy in GaAs-based quantum structures[20, 23]. However, while they report a quasi-instantaneous formation of a 40% exciton population directly after nonresonant excitation, we only observe such a quasi-instantaneous formation for higher excitation densities of $5.3 \cdot \mathrm{I}_0$. For lower excitation densities, our data reveal a finite formation time of tens of picoseconds before reaching comparable exciton fractions. Consequently, at lower excitation densities, it takes approximately 30 ps for the exciton population to build up to levels similar to the “quasi-instantaneous”

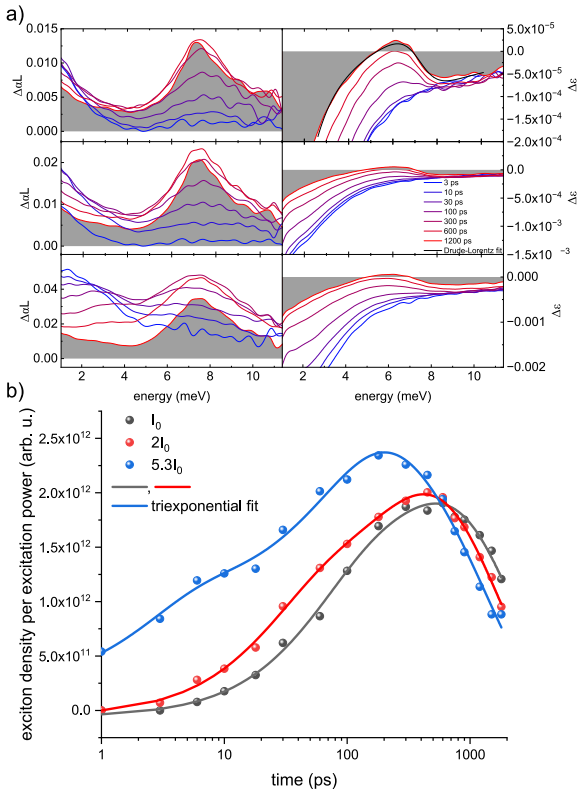

FIG. 4. a) Experimental THz-probe response after optical excitation at 1.468 eV for photon densities of I_0, $2 \cdot I_0$, and $5.3 \cdot I_0$. The left column depicts the change in absorption $\Delta\alpha L$ and the right column shows the change of the real part of the dielectric function $\Delta\epsilon$. b) Comparison of the normalized exciton density for three different excitation densities with an excitation energy of 1.468 eV. The colored circles represent the exciton density from the Drude-Lorentz fits while the solid lines correspond to triexponential fits.

exciton population observed at higher excitation densities. This abrupt transition from a fast exciton formation to a quasi-instantaneous exciton formation at a specific excitation density prompts several inquiries. First, what physical mechanism emerging above a certain carrier density could enable such an apparently instantaneous exciton formation that is absent at lower densities? Second, does this behavior represent a genuine physical process, or is it an artifact arising from the increasingly complex separation of excitonic and electron–hole plasma responses at high excitation densities? To validate the latter, a new method is required to disentangle the contributions of the Drude-like plasma response and the lorentzian intraexcitonic transition. One way to ensure a pure electron-hole plasma is to ionize the excitons by sufficiently strong THz fields [39–41].

Tuning the pump pulse resonantly to the $1s$ exciton absorption line allows for the direct generation of a pure exciton population. This bypasses the Drude-like response of an electron-hole plasma, provided that the pump density is sufficiently below the Mott density [37]. In Figure 5 we monitor the pump-induced change of absorption of sample **2** for various THz field strengths. At low THz probe field strengths, we observe a clean Lorentzian response characteristic of a Coulomb-bound exciton population. As the THz field increases, the spectrum broadens and develops a Drude-like component below 4 meV, indicating the coexistence of unbound carriers. At the highest applied field of 3577 V/cm, the response is purely Drude-like, signaling complete ionization of the exciton population. These observations demonstrate that by tuning the THz probe field strength, we can effectively switch between a predominantly excitonic system and a pure electron–hole plasma.

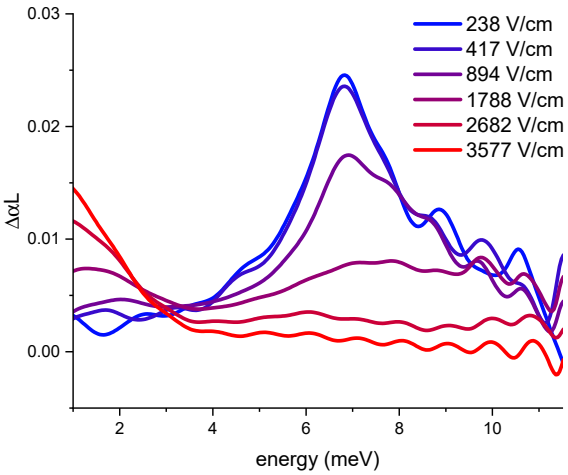

FIG. 5. $\Delta\alpha L$ of sample **2** after resonant excitation for different field strengths of the probing THz pulse.

Using this approach, we investigate exciton formation dynamics under nonresonant excitation by comparing the sample response under weak and strong THz probe fields. In Figure 6a), a weak THz field of ∼238 V/cm yields an initial Drude-like response at 3 ps, which evolves into a Lorentzian profile at later times—indicative of exciton formation out of the electron-hole plasma. In contrast, Figure 6b) shows the response under identical excitation conditions but for a strong THz field of ∼3577, V/cm. Here, although the early-time response is again Drude-like, no Lorentzian feature emerges at later delays because of efficient exciton ionization by the strong THz field. However, a gradual reduction in the Drude response reflects ongoing radiative and non-radiative carrier recombination. To isolate the excitonic contribution, we subtract the strong-field response from the weak-field response. This procedure removes the response of a pure electron–hole plasma from the total response of the sample, which may contain both exciton and plasma contributions. This effectively separates out the exciton

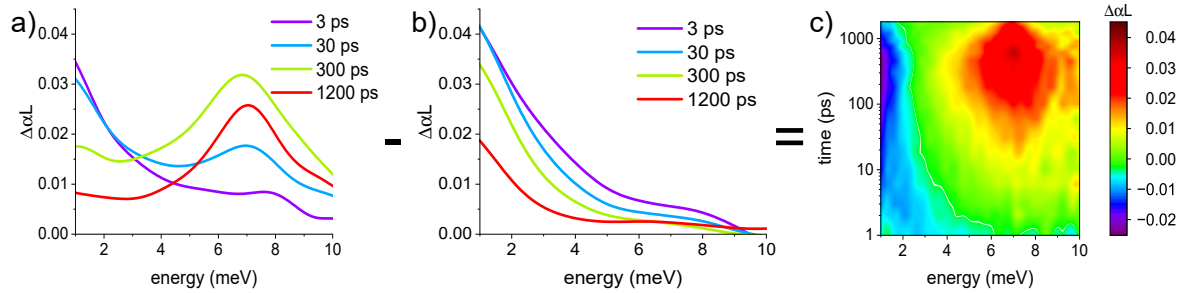

FIG. 6. Pump-induced change of the absorption $\Delta\alpha L$ for a photon density of $5.4 \cdot I_0$ and a probing field strength of a) 238 V/cm and b) 3577 V/cm. c) Temporal evolution of the differential response between the two probing field strengths.

dynamics. In the absence of excitons, this subtraction would ideally yield a flat zero line, as the two plasma responses cancel each other. However, in practice, the strong THz field slightly perturbs the carrier distribution, leading to modifications of the carriers' effective mass. This results in a slightly stronger THz absorption especially at lower energies, arising from an enhanced plasma response when probing with strong THz pulses. In contrast, when excitons are present, subtracting the strong-field spectrum removes the Drude-like plasma background and unveils a more distinct intraexcitonic resonance. In addition, a negative differential absorption emerges at low energies. This negative signal occurs because the strong THz field ionizes excitons, thereby increasing the density of unbound carriers which amplifies the plasma response. Subtracting this stronger plasma contribution from the weak-field spectrum results in a net negative differential signal in the corresponding spectral region. This behavior is illustrated across all time delays in Figure 6 c). Immediately after excitation, the differential absorption signal between 4.1 and 9.3 meV is essentially zero, indicating the absence of a Coulomb-bound exciton population. This directly rules out any instantaneous exciton formation. At lower energies, a weak negative signal is already present at early delays. This is attributed to the strong THz field slightly perturbing the carrier momentum distribution, thereby modifying the slope of the Drude response and leading to small deviations from perfect cancellation in the subtraction. With increasing time delay, a Lorentzian-shaped absorption feature emerges in the 5–9 meV range which is characteristic of the intraexcitonic $1s$–$2p$ transition. Simultaneously, the plasma response below ∼2.5 meV becomes increasingly negative. This trend is expected: the strong THz field ionizes the growing exciton population, thereby increasing the density of unbound carriers and enhancing the Drude-like plasma response. The resulting negative differential signal reflects this excess plasma contribution. To quantitatively assess exciton formation using this method, we integrate the differential THz absorption in the spectral window from 4.1 to 9.3 meV, where intraexcitonic transitions dominate. Since the Drude background has been effectively removed, this integration yields a direct measure of the exciton oscillator strength at each time delay. Figure 7 shows the normalized exciton oscillator strength as a function of time for various excitation densities. Interestingly, the data cannot be well-described by a simple biexponential model, similar to our earlier observations. Instead, we apply a triexponential fit to extract formation and decay timescales. In stark contrast to the apparent density dependence observed in conventional OPTP data (cf. Figure 4), the formation dynamics revealed by this differential method are largely independent of excitation density. Across all conditions, we identify three robust timescales: a fast component around ∼10 ps, a slower build up around ∼250 ps, and a density-dependent decay between 1 and 2 ns. These timescales are consistent with those extracted at lower densities with conventional OPTP and provide no evidence for a quasi-instantaneous formation process. Our high-temporal-resolution data thus challenge previous claims of ultrafast or quasi-instantaneous exciton formation. Instead, our results support a continuous, multi-timescale formation process that remains largely density-independent across the order of magnitude variation in excitation density explored here. It is well established that at very low excitation densities, exciton formation proceeds more slowly, consistent with reduced carrier–carrier and carrier–phonon scattering rates [21]. Conversely, as the excitation density approaches the Mott transition, exciton formation is suppressed. These observations indicate the existence of an intermediate density regime—such as the one investigated here—where exciton formation occurs on comparable, largely density-independent timescales. Within this intermediate regime, the slow exciton formation process on timescales around ∼250,ps, as observed in numerous experimental OPTP studies for different semiconductor systems [19–23], can be consistently attributed to the well-established phonon-assisted exciton formation mechanism. In this process, incoherent electron–hole pairs relax into $1s$ excitons through acoustic-phonon scattering, as described in various microscopic and kinetic models [18, 30, 32, 36, 42, 43]. The resulting

formation times of hundreds of picoseconds reflect the weak coupling strength of acoustic phonons and the requirement of energy dissipation for a high conversion of correlations into exciton populations.

The existence of an additional, much faster formation component on ∼10 ps timescales raises questions about its microscopic origin. While interactions with LO phonons have often been invoked as a rapid and efficient exciton formation mechanism [29–32, 44], this explanation appears inconsistent with our observations. The fast component shows no dependence on excitation excess energy, and LO-phonon emission is energetically forbidden for excitation close to the band edge, yet rapid exciton formation persists even under these conditions. We therefore attribute the observed ∼10 ps formation dynamics to a geminate-like exciton formation channel [30, 45], in which part of the initial Coulomb correlation between electrons and holes is preserved immediately after photoexcitation. Following initial carrier thermalization, a mixed ensemble of uncorrelated carriers and correlated electron–hole pairs coexists. The correlated pairs can evolve into an incoherent exciton population on picosecond timescales through Coulomb-mediated scattering, while the majority of carriers must first build up correlations and subsequently form excitons via the slower phonon-assisted pathway. This picture is consistent with the microscopic theory of exciton formation, in which exciton populations emerge from the decay of coherent interband polarizations through Coulomb and carrier–phonon interactions [18, 32, 43]. Although pure Coulomb coupling conserves the total energy of the plasma, higher-order Coulomb scattering processes enable energy redistribution among charge carriers. In such events, the binding energy of one correlated pair can be transferred to other electrons or holes, allowing a limited fraction of pairs to relax into Coulomb-bound excitonic states without lattice coupling. Moreover, excitons with large center-of-mass momenta can form even without significant energy loss, since their kinetic energy largely compensates the exciton binding energy. These considerations make a correlation-preserving, Coulomb-driven formation channel on a 10 ps timescale physically plausible. Further support for this interpretation comes from the absence of the rapid formation component in indirect-gap semiconductors such as Si [19], Ge [21], and Ge quantum wells [46]. In these materials, strong intervalley phonon scattering transfers charge carriers from the Γ-valley to side valleys during or shortly after excitation [47–49]. This intervalley transfer destroys the initial electron–hole Coulomb correlations that would otherwise support the geminate-like channel. As a result, only the slow, phonon-assisted exciton formation on the hundreds-of-picoseconds timescale remains observable.

The key insight provided by our method is that conventional OPTP spectroscopy alone, particularly at higher carrier densities, struggles to distinguish reliably between exciton and plasma contributions. In our case, this always leads to an overestimation of the exciton components, especially at early times. We assume that this overestimation of the exciton fraction with conventional OPTP spectroscopy has led to misinterpretation of the underlying dynamics [20, 28]. By eliminating the ambiguity between plasma and exciton responses, our approach provides a consistent and accurate framework for studying exciton formation. It reconciles previously conflicting results in the literature and offers a unified picture of many-body dynamics in GaAs-based quantum well structures across a broad range of excitation conditions.

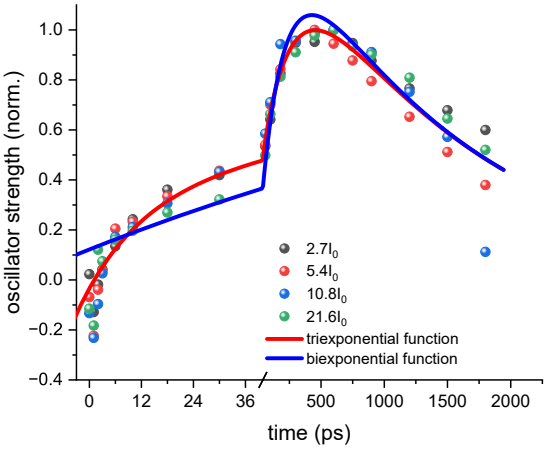

FIG. 7. Normalized oscillator strength for the intraexcitonic transition integrated from 4.1-9.3 meV for four excitation densities.

IV. CONCLUSION

We investigated the THz response of (Ga,In)As/GaAs multiple quantum wells following nonresonant optical excitation. Immediately after excitation, the system exhibits a characteristic Drude-like response from an unbound electron–hole plasma, which gradually evolves into a finite 1s exciton population. Exciton formation proceeds on two distinct timescales: a fast component within the first few tens of picoseconds and a slower phase extending over several hundred picoseconds. Interestingly, while conventional analyses suggest a strong dependence of these timescales on excitation density, our refined methodology reveals that exciton formation dynamics are rather independent of both the excitation density and excess energy within the investigated range. This conclusion is enabled by our new approach that systematically compares THz responses at weak and strong probe field strengths. By exploiting field-induced exciton ionization, we isolate the pure excitonic signal from the overlapping plasma background, even at higher excitation densities where traditional analysis struggles. Our results resolve longstanding ambiguities in the interpre-

tation of time-resolved THz spectroscopy and establish a robust, broadly applicable framework for disentangling exciton and plasma dynamics. This methodology offers clear insight into the intrinsic exciton formation process and is broadly applicable to the study of ultrafast many-body phenomena in semiconductor quantum structures.

V. DATA AVAILABILITY

The data that support the findings of this article are openly available `https://doi.org/10.22029/jlupub-20089.2`.

VI. ACKNOWLEDGEMENT

Financial support from the Deutsche Forschungsgemeinschaft via the Collaborative Research Center SFB 1083 under project No. 223848855 is gratefully acknowledged.

[1] C. V. Shank, Investigation of ultrafast phenomena in the femtosecond time domain, Science **233**, 1276 (1986).
[2] A. Othonos, Probing ultrafast carrier and phonon dynamics in semiconductors, Journal of applied physics **83**, 1789 (1998).
[3] J. Shah, *Ultrafast spectroscopy of semiconductors and semiconductor nanostructures*, Vol. 115 (Springer Science & Business Media, 2013).
[4] J. Szczytko, L. Kappei, J. Berney, F. Morier-Genoud, M. Portella-Oberli, and B. Deveaud, Determination of the exciton formation in quantum wells from time-resolved interband luminescence, Physical review letters **93**, 137401 (2004).
[5] S. W. Koch, M. Kira, G. Khitrova, and H. Gibbs, Semiconductor excitons in new light, Nature materials **5**, 523 (2006).
[6] J.-i. Kusano, Y. Segawa, Y. Aoyagi, S. Namba, and H. Okamoto, Extremely slow energy relaxation of a two-dimensional exciton in a GaAs superlattice structure, Physical Review B **40**, 1685 (1989).
[7] T. Damen, J. Shah, D. Oberli, D. Chemla, J. Cunningham, and J. Kuo, Dynamics of exciton formation and relaxation in GaAs quantum wells, Physical Review B **42**, 7434 (1990).
[8] R. Eccleston, R. Strobel, W. W. Rühle, J. Kuhl, B. F. Feuerbacher, and K. Ploog, Exciton dynamics in a GaAs quantum well, Phys. Rev. B **44**, 1395 (1991).
[9] P. W. M. Blom, P. J. van Hall, C. Smit, J. P. Cuypers, and J. H. Wolter, Selective exciton formation in thin GaAs/Al_xGa_{1-x}As quantum wells, Phys. Rev. Lett. **71**, 3878 (1993).
[10] D. Robart, X. Marie, B. Baylac, T. Amand, M. Brousseau, G. Bacquet, G. Debart, R. Planel, and J. Gerard, Dynamical equilibrium between excitons and free carriers in quantum wells, Solid state communications **95**, 287 (1995).
[11] R. Kumar, A. Vengurlekar, S. Prabhu, J. Shah, and L. Pfeiffer, Picosecond time evolution of free electron-hole pairs into excitons in GaAs quantum wells, Physical Review B **54**, 4891 (1996).
[12] M. Gurioli, P. Borri, M. Colocci, M. Gulia, F. Rossi, E. Molinari, P. E. Selbmann, and P. Lugli, Exciton formation and relaxation in GaAs epilayers, Phys. Rev. B **58**, R13403 (1998).
[13] W. Hoyer, C. Ell, M. Kira, S. Koch, S. Chatterjee, S. Mosor, G. Khitrova, H. Gibbs, and H. Stolz, Many-body dynamics and exciton formation studied by time-resolved photoluminescence, Physical Review B—Condensed Matter and Materials Physics **72**, 075324 (2005).
[14] B. Deveaud, B. Sermage, and D. Katzer, Free exciton versus free carrier luminescence in a quantum well, Le Journal de Physique IV **3**, C5 (1993).
[15] M. Kira, F. Jahnke, and S. Koch, Microscopic theory of excitonic signatures in semiconductor photoluminescence, Physical review letters **81**, 3263 (1998).
[16] S. Chatterjee, C. Ell, S. Mosor, G. Khitrova, H. Gibbs, W. Hoyer, M. Kira, S. W. Koch, J. Prineas, and H. Stolz, Excitonic photoluminescence in semiconductor quantum wells: Plasma versus excitons, Physical review letters **92**, 067402 (2004).
[17] I. Galbraith, R. Chari, S. Pellegrini, P. J. Phillips, C. J. Dent, A. F. G. van der Meer, D. G. Clarke, A. K. Kar, G. S. Buller, C. R. Pidgeon, B. N. Murdin, J. Allam, and G. Strasser, Excitonic signatures in the photoluminescence and terahertz absorption of a GaAs/Al_xGa_{1-x}As multiple quantum well, Phys. Rev. B **71**, 073302 (2005).
[18] M. Kira, W. Hoyer, T. Stroucken, and S. W. Koch, Exciton formation in semiconductors and the influence of a photonic environment, Physical review letters **87**, 176401 (2001).
[19] T. Suzuki and R. Shimano, Time-Resolved Formation of Excitons and Electron-Hole Droplets in Si Studied Using Terahertz Spectroscopy, Phys. Rev. Lett. **103**, 057401 (2009).
[20] R. A. Kaindl, M. A. Carnahan, D. Hägele, R. Lövenich, and D. S. Chemla, Ultrafast terahertz probes of transient conducting and insulating phases in an electron–hole gas, Nature **423**, 734 (2003).
[21] M. Stein, C. Lammers, P. Springer, P.-H. Richter, S. W. Koch, M. Koch, and M. Kira, Density-dependent exciton dynamics and L-valley anisotropy in germanium, Physical Review B **95**, 155207 (2017).
[22] M. Stein, C. Lammers, P.-H. Richter, C. Fuchs, W. Stolz, M. Koch, O. Vänskä, M. Weseloh, M. Kira, and S. Koch, Dynamics of charge-transfer excitons in type-II semiconductor heterostructures, Physical Review B **97**, 125306 (2018).
[23] R. A. Kaindl, D. Hägele, M. Carnahan, and D. Chemla, Transient terahertz spectroscopy of excitons and unbound carriers in quasi-two-dimensional electron-hole gases, Physical Review B **79**, 045320 (2009).

[24] R. Groeneveld and D. Grischkowskyt, Picosecond time-resolved far-infrared experiments on carriers and excitons in GaAs–AlGaAs multiple quantum wells, Journal of the Optical Society of America B **11**, 2502 (1994).

[25] S. Lutgen, T. Albrecht, T. Marschner, W. Stolz, and E. Göbel, Optical properties of symmetrically strained (GaIn) As/Ga (Pas) superlattices grown by metalorganic vapour phase epitaxy, Solid-state electronics **37**, 905 (1994).

[26] R. Ulbricht, E. Hendry, J. Shan, T. F. Heinz, and M. Bonn, Carrier dynamics in semiconductors studied with time-resolved terahertz spectroscopy, Reviews of Modern Physics **83**, 543 (2011).

[27] D. Anders, F. Dobener, F. Schäfer, S. Chatterjee, and M. Stein, Inhibited Inelastic Scattering of Incoherent Excitons for Near-Band Edge Excitations, Physical Review Letters **132**, 106901 (2024).

[28] P. Steinleitner, P. Merkl, P. Nagler, J. Mornhinweg, C. Schuller, T. Korn, A. Chernikov, and R. Huber, Direct observation of ultrafast exciton formation in a monolayer of WSe2, Nano Letters **17**, 1455 (2017).

[29] P. E. Selbmann, M. Gulia, F. Rossi, E. Molinari, and P. Lugli, Coupled free-carrier and exciton relaxation in optically excited semiconductors, Physical Review B **54**, 4660 (1996).

[30] C. Piermarocchi, F. Tassone, V. Savona, A. Quattropani, and P. Schwendimann, Exciton formation rates in $GaAs/Al_xGa_{1-x}As$ quantum wells, Phys. Rev. B **55**, 1333 (1997).

[31] I.-K. Oh, J. Singh, A. Thilagam, and A. Vengurlekar, Exciton formation assisted by LO phonons in quantum wells, Physical Review B **62**, 2045 (2000).

[32] K. Siantidis, V. M. Axt, and T. Kuhn, Dynamics of exciton formation for near band-gap excitations, Physical Review B **65**, 035303 (2001).

[33] L. Kappei, J. Szczytko, F. Morier-Genoud, and B. Deveaud, Direct observation of the Mott transition in an optically excited semiconductor quantum well, Physical review letters **94**, 147403 (2005).

[34] B. Deveaud, L. Kappei, J. Berney, F. Morier-Genoud, M. Portella-Oberli, J. Szczytko, and C. Piermarocchi, Excitonic effects in the luminescence of quantum wells, Chemical physics **318**, 104 (2005).

[35] A. Hangleiter, Z. Jin, M. Gerhard, D. Kalincev, T. Langer, H. Bremers, U. Rossow, M. Koch, M. Bonn, and D. Turchinovich, Efficient formation of excitons in a dense electron-hole plasma at room temperature, Physical Review B **92**, 241305 (2015).

[36] W. Hoyer, M. Kira, and S. W. Koch, Influence of Coulomb and phonon interaction on the exciton formation dynamics in semiconductor heterostructures, Physical Review B **67**, 155113 (2003).

[37] R. Huber, R. A. Kaindl, B. A. Schmid, and D. S. Chemla, Broadband terahertz study of excitonic resonances in the high-density regime in $GaAs/Al_xGa_{1-x}As$ quantum wells, Phys. Rev. B **72**, 161314 (2005).

[38] M. Stein, F. Schäfer, and L. Gomell, Inelastic electron-exciton scattering in bulk germanium, Physical Review B **99**, 144310 (2019).

[39] B. Ewers, N. Köster, R. Woscholski, M. Koch, S. Chatterjee, G. Khitrova, H. Gibbs, A. Klettke, M. Kira, and S. Koch, Ionization of coherent excitons by strong terahertz fields, Physical Review B—Condensed Matter and Materials Physics **85**, 075307 (2012).

[40] F. Sekiguchi, T. Mochizuki, C. Kim, H. Akiyama, L. N. Pfeiffer, K. W. West, and R. Shimano, Anomalous metal phase emergent on the verge of an exciton Mott transition, Physical review letters **118**, 067401 (2017).

[41] M. Stein, C. Lammers, J. Steiner, P. Richter, S. Koch, M. Koch, and M. Kira, Exciton ionization by THz pulses in germanium, Journal of Physics B: Atomic, Molecular and Optical Physics **51**, 154001 (2018).

[42] M. Gulia, F. Rossi, E. Molinari, P. E. Selbmann, and P. Lugli, Phonon-assisted exciton formation and relaxation in $GaAs/Al_xGa_{1-x}As$ quantum wells, Phys. Rev. B **55**, R16049 (1997).

[43] M. Kira and S. W. Koch, Many-body correlations and excitonic effects in semiconductor spectroscopy, Progress in quantum electronics **30**, 155 (2006).

[44] M. Umlauff, J. Hoffmann, H. Kalt, W. Langbein, J. M. Hvam, M. Scholl, J. Söllner, M. Heuken, B. Jobst, and D. Hommel, Direct observation of free-exciton thermalization in quantum-well structures, Physical Review B **57**, 1390 (1998).

[45] K. Mourzidis, V. Jindal, M. Glazov, A. Balocchi, C. Robert, D. Lagarde, P. Renucci, L. Lombez, T. Taniguchi, K. Watanabe, *et al.*, Exciton Formation in Two-Dimensional Semiconductors, Physical Review X **15**, 031078 (2025).

[46] D. Anders, Data for "exciton formation dynamics in (ga,in,)as quantum wells", (2025).

[47] S. A. Claussen, E. Tasyurek, J. E. Roth, and D. A. Miller, Measurement and modeling of ultrafast carrier dynamics and transport in germanium/silicon-germanium quantum wells, Optics Express **18**, 25596 (2010).

[48] C. Lange, N. S. Köster, S. Chatterjee, H. Sigg, D. Chrastina, G. Isella, H. von Känel, B. Kunert, and W. Stolz, Comparison of ultrafast carrier thermalization in $Ga_xIn_{1-x}As$ and Ge quantum wells, Phys. Rev. B **81**, 045320 (2010).

[49] E. J. Loren, J. Rioux, C. Lange, J. Sipe, H. van Driel, and A. L. Smirl, Hole spin relaxation and intervalley electron scattering in germanium, Physical Review B—Condensed Matter and Materials Physics **84**, 214307 (2011).

Other publications

- "Experimental studies of the excitonic nonlinear response of GaAs-based type-I and type-II quantum well structures interacting with optical and terahertz fields"
  Markus Stein, Felix Schäfer, **Daniel Anders**, Jan H. Littmann, Melanie Fey, Alexander Trautmann, Cong Ngo, Johannes T. Steiner, Matthias Reichelt, Christian Fuchs, Kerstin Volz, Torsten Meier and Sangam Chatterjee
  in *Proceedings Volume 12419, Ultrafast Phenomena and Nanophotonics XXVII*; 1241909 (2023)

- "Analysis of the nonlinear optical response of excitons in type-I and type-II quantum wells including many-body correlations"
  Alexander Trautmann, Markus Stein, Felix Schäfer, **Daniel Anders**, Cong Ngo, Johannes T. Steiner, Matthias Reichelt, Sangam Chatterjee and Torsten Meier
  in *Proceedings Volume 12419, Ultrafast Phenomena and Nanophotonics XXVII*; 1241909 (2023)

- "Distinct Rabi splitting in confined systems of $MoSe_2$ monolayes and (Ga,In)As quantum wells"
  Felix Schäfer, Henry Mittenzwey, Markus Stein, Oliver Voigt, Lara Greten, **Daniel Anders**, Isabel Müller, Florian Dobener, Marzia Cuccu, Christian Fuchs, Kenji Watanabe, Takashi Taniguchi, Alexey Chernikov, Kerstin Volz, Andreas Knorr, Sangam Chatterjee
  Nature Communications 16.1 (2025): 8109

- "Low Temperature MOCVD Synthesis of High-Mobility 2D InSe"
  Robin Günkel, Oliver Maßmeyer, Markus Stein, Kalle Bräumer, Rodrigo Sandoval Rodriguez, **Daniel Anders**, Jan-Heinrich Littmann, Sebastian Anhäuser, Badrosadat Ojaghi Dogahe, Max Bergmann, Milan Solanki, Nils Fritjof Langlotz, Johannes Glowatzki, Jürgen Belz, Andreas Beyer, Gregor Witte, Sangam Chatterjee, Kerstin Volz
  Small (2025): e10911

- "Terahertz Gain Induced by Light-Field-Driven Exciton States"
  Daniel Anders, Markus Stein, A Hambarde, Matthias Florian, Mackillo Kira, Sangam Chatterjee
  2025 50th International Conference on Infrared, Millimeter, and Terahertz Waves (IRMMW-THz)

- "Surface diffusion control enables tailored-aspect-ratio nanostructures in area-selective atomic layer deposition"
  Philip Klement, **Daniel Anders**, Lukas Gümbel, Michele Bastianello, Fabian Michel, Jörg Schörmann, Matthias T Elm, Christian Heiliger, Sangam Chatterjee
  ACS applied materials & interfaces 13.16 (2021): 19398-19405

- "Analysis of the nonlinear optical response of excitons in type-I and type-II quantum wells including many-body correlations"
  Alexander Trautmann, Markus Stein, Felix Schäfer, **Daniel Anders**, Cong Ngo, Johannes Tilman Steiner, Matthias Reichelt, Sangam Chatterjee, Torsten Meier
  in *Ultrafast Phenomena and Nanophotonics XXVII*. Vol. 12419. SPIE, 2023

- "Photon-Dressed Exciton States and Terahertz Gain unveiled by THz Spectroscopy"
  Daniel Anders, Markus Stein, Sangam Chatterjee
  in *CLEO: Fundamental Science (pp. FW3I-2)*. Optica Publishing Group

- "Coherent optical nonlinearities in model type-II heterostructures"
  Markus Stein, Felix Schäfer, **Daniel Anders**, Jan H Littmnann, Michael Zengel, Kerstin Volz, Sangam Chatterjee
  in *Ultrafast Phenomena and Nanophotonics XXVIII*, 2024

- "Experimental studies of the excitonic nonlinear response of GaAs-based type-I and type-II quantum well structures interacting with optical and terahertz fields"
  Markus Stein, Felix Schäfer, **Daniel Anders**, Jan H Littmann, Melanie Fey, Alexander Trautmann, Cong Ngo, Johannes T Steiner, Matthias Reichelt, Christian Fuchs, Kerstin Volz, Torsten Meier, Sangam Chatterjee
  in *Ultrafast Phenomena and Nanophotonics XXVII*, 2023

- "In-depth Characterization of the Electron System in a RIT-10 Plasma using THz–TDS: Results and Challenges"
  Rodrigo Ignazio Sandoval Rodriguez, Kalle Julius Bräumer, Konstantin Keil, Jana Zorn, **Daniel Anders**, Kristof Holste, Markus Stein, Sangam Chatterjee, Peter Jens Klar
  39th International Electric Propulsion Conference

Bibliography

[1] Rico Gutzler et al. “Light–matter interaction at atomic scales”. In: *Nature Reviews Physics* 3.6 (2021), pp. 441–453.

[2] AA Abrikosov and IM Khalatnikov. “The theory of a fermi liquid (the properties of liquid 3He at low temperatures)”. In: *Reports on Progress in Physics* 22.1 (1959), pp. 329–367.

[3] Hartmut Haug and Stephan W Koch. *Quantum theory of the optical and electronic properties of semiconductors*. world scientific, 2009.

[4] John Bardeen, Leon N Cooper, and John Robert Schrieffer. “Theory of superconductivity”. In: *Physical review* 108.5 (1957), p. 1175.

[5] Robert B Laughlin. “Anomalous quantum Hall effect: An incompressible quantum fluid with fractionally charged excitations”. In: *Physical Review Letters* 50.18 (1983), p. 1395.

[6] Daniel Arovas, John R Schrieffer, and Frank Wilczek. “Fractional statistics and the quantum Hall effect”. In: *Physical review letters* 53.7 (1984), p. 722.

[7] Gregory H Wannier. “The structure of electronic excitation levels in insulating crystals”. In: *Physical Review* 52.3 (1937), p. 191.

[8] Giuseppe Carlo La Rocca. “Wannier–Mott excitons in semiconductors”. In: *Thin films and nanostructures* 31 (2003), pp. 97–128.

[9] Daniel S. Chemla and Jagdeep Shah. “Many-body and correlation effects in semiconductors”. In: *Nature* 411.6837 (2001), pp. 549–557.

[10] Thomas Mueller and Ermin Malic. “Exciton physics and device application of two-dimensional transition metal dichalcogenide semiconductors”. In: *npj 2D Materials and Applications* 2.1 (2018), p. 29.

[11] Robert A. Kaindl et al. “Ultrafast terahertz probes of transient conducting and insulating phases in an electron–hole gas”. In: *Nature* 423.6941 (2003), pp. 734–738.

[12] J. Černe et al. “Terahertz Dynamics of Excitons in GaAs/AlGaAs Quantum Wells”. In: *Physical Review Letters* 77.6 (Aug. 1996), pp. 1131–1134. ISSN: 0031-9007. DOI: 10.1103/PhysRevLett.77.1131.

[13] RHM Groeneveld and D Grischkowskyt. “Picosecond time-resolved far-infrared experiments on carriers and excitons in GaAs–AlGaAs multiple quantum wells”. In: *Journal of the Optical Society of America B* 11.12 (1994), pp. 2502–2507.

[14] Robert A Kaindl et al. “Transient terahertz spectroscopy of excitons and unbound carriers in quasi-two-dimensional electron-hole gases”. In: *Physical Review B—Condensed Matter and Materials Physics* 79.4 (2009), p. 045320.

[15] M Kira, F Jahnke, and SW Koch. “Microscopic theory of excitonic signatures in semiconductor photoluminescence”. In: *Physical review letters* 81.15 (1998), p. 3263.

[16] Mackillo Kira and Stephan W Koch. “Many-body correlations and excitonic effects in semiconductor spectroscopy”. In: *Progress in quantum electronics* 30.5 (2006), pp. 155–296.

[17] Rajesh Kumar et al. “Picosecond time evolution of free electron-hole pairs into excitons in GaAs quantum wells”. In: *Physical Review B* 54.7 (1996), p. 4891.

[18] B Deveaud et al. “Excitonic effects in the luminescence of quantum wells”. In: *Chemical physics* 318.1-2 (2005), pp. 104–117.

[19] Bradley Ferguson and Xi-Cheng Zhang. “Materials for terahertz science and technology”. In: *Nature materials* 1.1 (2002), pp. 26–33.

[20] P Uhd Jepsen, David G Cooke, and Martin Koch. “Terahertz spectroscopy and imaging–Modern techniques and applications”. In: *Laser & Photonics Reviews* 5.1 (2011), pp. 124–166.

[21] F Sizov. “Terahertz radiation detectors: the state-of-the-art”. In: *Semiconductor science and technology* 33.12 (2018), p. 123001.

[22] Tom Seifert et al. “Efficient metallic spintronic emitters of ultrabroadband terahertz radiation”. In: *Nature photonics* 10.7 (2016), pp. 483–488.

[23] Zheng Feng et al. “Spintronic terahertz emitter”. In: *Journal of Applied Physics* 129.1 (2021).

[24] Nathan M Burford and Magda O El-Shenawee. “Review of terahertz photoconductive antenna technology”. In: *Optical Engineering* 56.1 (2017), pp. 010901–010901.

[25] Luke Peters et al. “Resonant fully dielectric metasurfaces for ultrafast terahertz pulse generation”. In: *Advanced Optical Materials* 12.16 (2024), p. 2303148.

[26] Neeta Amitkumar Ukirade. “A review on advancement of materials for terahertz applications”. In: *Next Materials* 6 (2025), p. 100479.

[27] SS Dhillon et al. “The 2017 terahertz science and technology roadmap”. In: *Journal of Physics D: Applied Physics* 50.4 (2017), p. 043001.

[28] R Atanasov et al. “Coherent control of photocurrent generation in bulk semiconductors”. In: *Physical review letters* 76.10 (1996), p. 1703.

[29] A Haché et al. “Observation of coherently controlled photocurrent in unbiased, bulk GaAs”. In: *Physical Review Letters* 78.2 (1997), p. 306.

[30] A Singh et al. “Gapless broadband terahertz emission from a germanium photoconductive emitter”. In: *Acs Photonics* 5.7 (2018), pp. 2718–2723.

[31] Tyler L Cocker et al. “An ultrafast terahertz scanning tunnelling microscope”. In: *Nature Photonics* 7.8 (2013), pp. 620–625.

[32] Jagdeep Shah. *Ultrafast spectroscopy of semiconductors and semiconductor nanostructures*. Vol. 115. Springer Science & Business Media, 2013.

[33] Han-Kwang Nienhuys and Villy Sundström. “Intrinsic complications in the analysis of optical-pump, terahertz probe experiments”. In: *Physical Review B—Condensed Matter and Materials Physics* 71.23 (2005), p. 235110.

[34] C Ciuti et al. “Role of the exchange of carriers in elastic exciton-exciton scattering in quantum wells”. In: *Physical Review B* 58.12 (1998), p. 7926.

[35] Rupert Huber et al. "Broadband terahertz study of excitonic resonances in the high-density regime in GaAs/$Al_xGa_{1-x}As$ quantum wells". In: *Physical Review B—Condensed Matter and Materials Physics* 72.16 (2005), p. 161314.

[36] Enrico Fermi. *Nuclear physics: a course given by Enrico Fermi at the University of Chicago*. University of Chicago press, 1950.

[37] M Lindberg and Stephan W Koch. "Effective Bloch equations for semiconductors". In: *Physical Review B* 38.5 (1988), p. 3342.

[38] Mackillo Kira and Stephan W Koch. *Semiconductor quantum optics*. Cambridge University Press, 2011.

[39] Claus Klingshirn. *Semiconductor optics*. Springer, 2007.

[40] Torsten Meier, Peter Thomas, and Stephan W Koch. *Coherent semiconductor optics: from basic concepts to nanostructure applications*. Springer, 2007.

[41] Jens Fricke. "Transport equations including many-particle correlations for an arbitrary quantum system: A general formalism". In: *Annals of physics* 252.2 (1996), pp. 479–498.

[42] M Kira and SW Koch. "Cluster-expansion representation in quantum optics". In: *Physical Review A—Atomic, Molecular, and Optical Physics* 78.2 (2008), p. 022102.

[43] Jacov Frenkel. "On the transformation of light into heat in solids. I". In: *Physical Review* 37.1 (1931), p. 17.

[44] YU Peter and Manuel Cardona. *Fundamentals of semiconductors: physics and materials properties*. Springer Science & Business Media, 2010.

[45] Nevill F Mott. "Metal-insulator transition". In: *Reviews of Modern Physics* 40.4 (1968), p. 677.

[46] Xinwei Li et al. "Observation of photoinduced terahertz gain in GaAs quantum wells: evidence for radiative two-exciton-to-biexciton scattering". In: *Physical Review Letters* 125.16 (2020), p. 167401.

[47] FJ Teran et al. "Trion formation in narrow GaAs quantum well structures". In: *Physical Review B—Condensed Matter and Materials Physics* 71.16 (2005), p. 161309.

[48] AE Almand-Hunter et al. "Quantum droplets of electrons and holes". In: *Nature* 506.7489 (2014), pp. 471–475.

[49] Carson D Jeffries. "Electron-hole condensation in semiconductors: Electrons and holes condense into freely moving liquid metallic droplets, a plasma phase with novel properties". In: *Science* 189.4207 (1975), pp. 955–964.

[50] SW Koch et al. "Semiconductor excitons in new light". In: *Nature materials* 5.7 (2006), pp. 523–531.

[51] M Kira, W Hoyer, and SW Koch. "Terahertz signatures of the exciton formation dynamics in non-resonantly excited semiconductors". In: *Solid state communications* 129.11 (2004), pp. 733–736.

[52] RA Kaindl et al. "Ultrafast THz Spectroscopy of Excitons in Multi-Component Carrier Gases". In: *Advances in Solid State Physics*. Springer, 2008, pp. 191–202.

[53] Marc M Dignam et al. "An excitonic approach to the intraband THz response of semiconductor nanostructures". In: *AIP Conference Proceedings*. Vol. 1590. 1. American Institute of Physics. 2014, pp. 20–25.

[54] AB Dzyubenko. “Intraexcitonic transitions in two-dimensional systems in a high magnetic field”. In: *Journal of Experimental and Theoretical Physics Letters* 66.9 (1997), pp. 617–623.

[55] Kalle Bräumer et al. “Validating THz time-domain spectroscopy as a tool for characterizing low pressure inductively coupled plasmas of ion thrusters”. In: *Journal of Electric Propulsion* 4.1 (2025), p. 9.

[56] MF Kimmitt et al. “Where optics meets electronics: recent progress in decreasing the terahertz gap-Discussion”. In: *Philosophical Transactions of the Royal Society. A, Mathematical, Physical and Engineering Sciences* 362 (2004), pp. 212–213.

[57] Masayoshi Tonouchi. “Cutting-edge terahertz technology”. In: *Nature photonics* 1.2 (2007), pp. 97–105.

[58] Roger A Lewis. “A review of terahertz sources”. In: *Journal of Physics D: Applied Physics* 47.37 (2014), p. 374001.

[59] R Lawrence Ives et al. “Development of backward-wave oscillators for terahertz applications”. In: *Terahertz for Military and Security Applications*. Vol. 5070. SPIE. 2003, pp. 71–82.

[60] John H Booske et al. “Vacuum electronic high power terahertz sources”. In: *IEEE Transactions on Terahertz Science and Technology* 1.1 (2011), pp. 54–75.

[61] Martin Philipp. “Entwicklung und Aufbau eines BWO-basierten 1, 9 THz Lokaloszillatoren für den Heterodynempfänger GREAT”. PhD thesis. Universität zu Köln, 2008.

[62] A Rice et al. “Terahertz optical rectification from< 110> zinc-blende crystals”. In: *Applied physics letters* 64.11 (1994), pp. 1324–1326.

[63] K-L Yeh et al. “Generation of 10μJ ultrashort terahertz pulses by optical rectification”. In: *Applied Physics Letters* 90.17 (2007).

[64] DJ Cook and RM Hochstrasser. “Intense terahertz pulses by four-wave rectification in air”. In: *Optics letters* 25.16 (2000), pp. 1210–1212.

[65] Abebe T Tarekegne et al. “Terahertz time-domain spectroscopy of zone-folded acoustic phonons in 4H and 6H silicon carbide”. In: *Optics Express* 27.3 (2019), pp. 3618–3628.

[66] E Saitoh et al. “Conversion of spin current into charge current at room temperature: Inverse spin-Hall effect”. In: *Applied physics letters* 88.18 (2006).

[67] David H Auston. “Picosecond optoelectronic switching and gating in silicon”. In: *Applied Physics Letters* 26.3 (1975), pp. 101–103.

[68] A Haché, JE Sipe, and HM Van Driel. “Quantum interference control of electrical currents in GaAs”. In: *IEEE Journal of Quantum Electronics* 34.7 (2002), pp. 1144–1154.

[69] San-Huang Ke, Weitao Yang, and Harold U Baranger. “Quantum-interference-controlled molecular electronics”. In: *Nano letters* 8.10 (2008), pp. 3257–3261.

[70] Dong Sun et al. “Coherent control of ballistic photocurrents in multilayer epitaxial graphene using quantum interference”. In: *Nano letters* 10.4 (2010), pp. 1293–1296.

[71] Martin J Stevens et al. “Quantum interference control of ballistic pure spin currents in semiconductors”. In: *Physical review letters* 90.13 (2003), p. 136603.

[72] E Sternemann et al. “Femtosecond quantum interference control of electrical currents in GaAs: signatures beyond the perturbative χ (3) limit”. In: *Physical Review B—Condensed Matter and Materials Physics* 88.16 (2013), p. 165204.

[73] Lammers Christian. “Über die Dynamik des Charge-Transfer-Exzitons”. In: ().

[74] Sang-Gil Park et al. “Terahertz photoconductive antenna with metal nanoislands”. In: *Optics express* 20.23 (2012), pp. 25530–25535.

[75] Heribert Eisele, Mira Naftaly, and John R Fletcher. “A simple interferometer for the characterization of sources at terahertz frequencies”. In: *Measurement Science and Technology* 18.8 (2007), pp. 2623–2628.

[76] Sergey Cherednichenko et al. “Hot-electron bolometer terahertz mixers for the Herschel Space Observatory”. In: *Review of scientific instruments* 79.3 (2008).

[77] Ralf Müller et al. “Characterization of a large-area pyroelectric detector from 300 GHz to 30 THz”. In: *Journal of Infrared, Millimeter, and Terahertz Waves* 36.7 (2015), pp. 654–661.

[78] Marcel JE Golay. “Theoretical consideration in heat and infra-red detection, with particular reference to the pneumatic detector”. In: *Review of Scientific Instruments* 18.5 (1947), pp. 347–356.

[79] Hua Qin et al. “Detection of incoherent terahertz light using antenna-coupled high-electron-mobility field-effect transistors”. In: *Applied Physics Letters* 110.17 (2017).

[80] Yun-Shik Lee. *Principles of terahertz science and technology*. Vol. 170. Springer Science & Business Media, 2009.

[81] C Kübler et al. “Ultrabroadband detection of multi-terahertz field transients with GaSe electro-optic sensors: Approaching the near infrared”. In: *Applied physics letters* 85.16 (2004), pp. 3360–3362.

[82] Qi Wu and X-C Zhang. “Free-space electro-optic sampling of terahertz beams”. In: *Applied Physics Letters* 67.24 (1995), pp. 3523–3525.

[83] Q Wu and X-C Zhang. “7 terahertz broadband GaP electro-optic sensor”. In: *Applied Physics Letters* 70.14 (1997), pp. 1784–1786.

[84] Peter E Powers and Joseph W Haus. *Fundamentals of nonlinear optics*. CRC press, 2017.

[85] Kai-Erik Peiponen, Axel Zeitler, and Makoto Kuwata-Gonokami. *Terahertz spectroscopy and imaging*. Vol. 171. Springer, 2012.

[86] A Leitenstorfer et al. “Detectors and sources for ultrabroadband electro-optic sampling: Experiment and theory”. In: *Applied physics letters* 74.11 (1999), pp. 1516–1518.

[87] Guilhem Gallot and D Grischkowsky. “Electro-optic detection of terahertz radiation”. In: *Journal of the Optical Society of America B* 16.8 (1999), pp. 1204–1212.

[88] HJ Bakker et al. “Distortion of terahertz pulses in electro-optic sampling”. In: *Journal of the Optical Society of America B* 15.6 (1998), pp. 1795–1801.

[89] Ronald Ulbricht et al. “Carrier dynamics in semiconductors studied with time-resolved terahertz spectroscopy”. In: *Reviews of Modern Physics* 83.2 (2011), p. 543.

[90] G. W. Fehrenbach et al. “Transient Optical Spectra of a Dense Exciton Gas in a Direct-Gap Semiconductor”. In: *Physical Review Letters* 49.17 (1982), pp. 1281–1284. ISSN: 0031-9007. DOI: 10.1103/PhysRevLett.49.1281.

[91] N. Peyghambarian et al. “Blue Shift of the Exciton Resonance due to Exciton-Exciton Interactions in a Multiple-Quantum-Well Structure”. In: *Physical Review Letters* 53.25 (1984), pp. 2433–2436. ISSN: 0031-9007. DOI: 10.1103/PhysRevLett.53.2433.

[92] Matthew C Beard, Gordon M Turner, and Charles A Schmuttenmaer. “Transient photoconductivity in GaAs as measured by time-resolved terahertz spectroscopy”. In: *Physical Review B* 62.23 (2000), p. 15764.

[93] Matthew C Beard, Gordon M Turner, and Charles A Schmuttenmaer. “Subpicosecond carrier dynamics in low-temperature grown GaAs as measured by time-resolved terahertz spectroscopy”. In: *Journal of Applied Physics* 90.12 (2001), pp. 5915–5923.

[94] Paul CM Planken et al. “Measurement and calculation of the orientation dependence of terahertz pulse detection in ZnTe”. In: *Journal of the Optical Society of America B* 18.3 (2001), pp. 313–317.

[95] DS Sitnikov et al. “Estimation of THz field strength by an electro-optic sampling technique using arbitrary long gating pulses”. In: *Laser Physics Letters* 16.11 (2019), p. 115302.

[96] Roman JB Dietz et al. “All fiber-coupled THz-TDS system with kHz measurement rate based on electronically controlled optical sampling”. In: *Optics letters* 39.22 (2014), pp. 6482–6485.

[97] Robert B Kohlhaas et al. “Ultrabroadband terahertz time-domain spectroscopy using III-V photoconductive membranes on silicon”. In: *Optics Express* 30.13 (2022), pp. 23896–23908.

[98] Martin Koch et al. “Terahertz time-domain spectroscopy”. In: *Nature Reviews Methods Primers* 3.1 (2023), p. 48.

[99] *Tera-Sed datasheet*. Laserquantum.

[100] Matthias C Hoffmann et al. “Efficient terahertz generation by optical rectification at 1035 nm”. In: *Optics Express* 15.18 (2007), pp. 11706–11713.

[101] JA Fülöp et al. “Design of high-energy terahertz sources based on optical rectification”. In: *Optics express* 18.12 (2010), pp. 12311–12327.

[102] JA Fülöp et al. “Generation of sub-mJ terahertz pulses by optical rectification”. In: *Optics letters* 37.4 (2012), pp. 557–559.

[103] Evangelos Th Papaioannou and René Beigang. “THz spintronic emitters: a review on achievements and future challenges”. In: *Nanophotonics* 10.4 (2021), pp. 1243–1257.

[104] Markus Kress et al. “Terahertz-pulse generation by photoionization of air with laser pulses composed of both fundamental and second-harmonic waves”. In: *Optics letters* 29.10 (2004), pp. 1120–1122.

[105] Mark D Thomson, Volker Blank, and Hartmut G Roskos. “Terahertz white-light pulses from an air plasma photo-induced by incommensurate two-color optical fields”. In: *Optics Express* 18.22 (2010), pp. 23173–23182.

[106] Benjamin Clough, Jianming Dai, and Xi-Cheng Zhang. "Laser air photonics: beyond the terahertz gap". In: *Materials Today* 15.1-2 (2012), pp. 50–58.

[107] Abhishek Singh et al. "Up to 70 THz bandwidth from an implanted Ge photoconductive antenna excited by a femtosecond Er: fibre laser". In: *Light: Science & Applications* 9.1 (2020), p. 30.

[108] D Côté et al. "THz emission from coherently controlled photocurrents in GaAs". In: *Applied Physics Letters* 75.25 (1999), pp. 3959–3961.

[109] Louis Costa et al. "All-optical injection of ballistic electrical currents in unbiased silicon". In: *Nature Physics* 3.9 (2007), pp. 632–635.

[110] Marko Spasenović et al. "All-optical coherent control of electrical currents in centrosymmetric semiconductors". In: *Physical Review B* 77.8 (2008), p. 085201.

[111] Zhihui Lü et al. "Coherently controlled terahertz source for a time domain spectroscopy system via injection current in bulk ZnSe". In: *Applied Optics* 51.5 (2012), pp. 676–679.

[112] JS Totero Gongora et al. "All-optical two-color terahertz emission from quasi-2D nonlinear surfaces". In: *Physical Review Letters* 125.26 (2020), p. 263901.

[113] Christian Sames et al. "All-optical coherently controlled terahertz ac charge currents from excitons in semiconductors". In: *Physical Review B* 79.4 (2009), p. 045208.

[114] Christian Meineke et al. "Scalable high-repetition-rate sub-half-cycle terahertz pulses from spatially indirect interband transitions". In: *Light: Science & Applications* 11.1 (2022), p. 151.

[115] Tyler L Cocker et al. "Tracking the ultrafast motion of a single molecule by femtosecond orbital imaging". In: *Nature* 539.7628 (2016), pp. 263–267.

[116] Katsumasa Yoshioka et al. "Real-space coherent manipulation of electrons in a single tunnel junction by single-cycle terahertz electric fields". In: *Nature photonics* 10.12 (2016), pp. 762–765.

[117] Charles V Shank. "Investigation of ultrafast phenomena in the femtosecond time domain". In: *Science* 233.4770 (1986), pp. 1276–1280.

[118] Ernst O Göbel. "Ultrafast spectroscopy of semiconductors". In: *Optics and Photonics News* 3.5 (1992), pp. 33–39.

[119] Margherita Maiuri, Marco Garavelli, and Giulio Cerullo. "Ultrafast spectroscopy: State of the art and open challenges". In: *Journal of the American Chemical Society* 142.1 (2019), pp. 3–15.

[120] John TM Kennis and Marie-Louise Groot. "Ultrafast spectroscopy of biological photoreceptors". In: *Current opinion in structural biology* 17.5 (2007), pp. 623–630.

[121] Erik TJ Nibbering, Henk Fidder, and Ehud Pines. "Ultrafast chemistry: using time-resolved vibrational spectroscopy for interrogation of structural dynamics". In: *Annu. Rev. Phys. Chem.* 56.1 (2005), pp. 337–367.

[122] Graham Fleming. "Chemical applications of ultrafast spectroscopy". In: (1986).

[123] Jun-ichi Kusano et al. "Extremely slow energy relaxation of a two-dimensional exciton in a GaAs superlattice structure". In: *Physical Review B* 40.3 (1989), p. 1685.

[124] TC Damen et al. “Dynamics of exciton formation and relaxation in GaAs quantum wells”. In: *Physical Review B* 42.12 (1990), p. 7434.

[125] R. Eccleston et al. “Exciton dynamics in a GaAs quantum well”. In: *Phys. Rev. B* 44 (3 1991), pp. 1395–1398. DOI: 10.1103/PhysRevB.44.1395.

[126] PWM Blom et al. “Selective exciton formation in thin GaAs/Al x Ga 1- x As quantum wells”. In: *Physical review letters* 71.23 (1993), p. 3878.

[127] D Robart et al. “Dynamical equilibrium between excitons and free carriers in quantum wells”. In: *Solid state communications* 95.5 (1995), pp. 287–293.

[128] M. Gurioli et al. “Exciton formation and relaxation in GaAs epilayers”. In: *Phys. Rev. B* 58 (20 1998), R13403–R13406. DOI: 10.1103/PhysRevB.58.R13403.

[129] W Hoyer et al. “Many-body dynamics and exciton formation studied by time-resolved photoluminescence”. In: *Physical Review B—Condensed Matter and Materials Physics* 72.7 (2005), p. 075324.

[130] J Szczytko et al. “Determination of the exciton formation in quantum wells from time-resolved interband luminescence”. In: *Physical review letters* 93.13 (2004), p. 137401.

[131] S Chatterjee et al. “Excitonic photoluminescence in semiconductor quantum wells: Plasma versus excitons”. In: *Physical review letters* 92.6 (2004), p. 067402.

[132] I Galbraith et al. “Excitonic signatures in the photoluminescence and terahertz absorption of a Ga As/ Al x Ga 1- x As multiple quantum well”. In: *Physical Review B* 71.7 (2005), p. 073302.

[133] M Kira et al. “Exciton formation in semiconductors and the influence of a photonic environment”. In: *Physical Review Letters* 87.17 (2001), p. 176401.

[134] Takeshi Suzuki and Ryo Shimano. “Time-Resolved Formation of Excitons and Electron-Hole Droplets in Si Studied Using Terahertz Spectroscopy”. In: *Physical review letters* 103.5 (2009), p. 057401.

[135] Markus Stein et al. “Density-dependent exciton dynamics and L-valley anisotropy in germanium”. In: *Physical Review B* 95.15 (2017), p. 155207.

[136] M Stein et al. “Dynamics of charge-transfer excitons in type-II semiconductor heterostructures”. In: *Physical Review B* 97.12 (2018), p. 125306.

[137] L Kappei et al. “Direct observation of the Mott transition in an optically excited semiconductor quantum well”. In: *Physical review letters* 94.14 (2005), p. 147403.

[138] Chaw Keong Yong et al. “Direct observation of charge-carrier heating at WZ–ZB InP nanowire heterojunctions”. In: *Nano letters* 13.9 (2013), pp. 4280–4287.

[139] Andreas Hangleiter et al. “Efficient formation of excitons in a dense electron-hole plasma at room temperature”. In: *Physical Review B* 92.24 (2015), p. 241305.

[140] M Stein et al. “Exciton ionization by THz pulses in germanium”. In: *Journal of Physics B: Atomic, Molecular and Optical Physics* 51.15 (2018), p. 154001.

[141] B Ewers et al. “Ionization of coherent excitons by strong terahertz fields”. In: *Physical Review B—Condensed Matter and Materials Physics* 85.7 (2012), p. 075307.

[142] Fumiya Sekiguchi et al. “Anomalous metal phase emergent on the verge of an exciton Mott transition”. In: *Physical review letters* 118.6 (2017), p. 067401.

[143] Jagdeep Shah, M Combescot, and AH Dayem. “Investigation of exciton-plasma Mott transition in Si”. In: *Physical Review Letters* 38.25 (1977), p. 1497.

[144] C. Piermarocchi et al. “Exciton formation rates in GaAs/$Al_xGa_{1-x}As$ quantum wells”. In: *Phys. Rev. B* 55 (3 Jan. 1997), pp. 1333–1336. DOI: 10.1103/PhysRevB.55.1333.

[145] K Siantidis, Vollrath Martin Axt, and Tilmann Kuhn. “Dynamics of exciton formation for near band-gap excitations”. In: *Physical Review B* 65.3 (2001), p. 035303.

[146] Walter Hoyer, Mackillo Kira, and Stephan W Koch. “Influence of Coulomb and phonon interaction on the exciton formation dynamics in semiconductor heterostructures”. In: *Physical Review B* 67.15 (2003), p. 155113.

[147] Mario Gulia et al. “Phonon-assisted exciton formation and relaxation in GaAs/$Al_xGa_{1-x}As$ quantum wells”. In: *Phys. Rev. B* 55 (24 June 1997), R16049–R16052. DOI: 10.1103/PhysRevB.55.R16049.

[148] Peter E Selbmann et al. “Coupled free-carrier and exciton relaxation in optically excited semiconductors”. In: *Physical Review B* 54.7 (1996), p. 4660.

[149] M Umlauff et al. “Direct observation of free-exciton thermalization in quantum-well structures”. In: *Physical Review B* 57.3 (1998), p. 1390.

[150] I-K Oh et al. “Exciton formation assisted by LO phonons in quantum wells”. In: *Physical Review B* 62.3 (2000), p. 2045.

[151] Konstantinos Mourzidis et al. “Exciton Formation in Two-Dimensional Semiconductors”. In: *Physical Review X* 15.3 (2025), p. 031078.

[152] SG Elkomoss and G Munschy. “Electron-exciton elastic scattering cross sections in the central field and the exchange approximations”. In: *Journal of Physics and Chemistry of Solids* 38.6 (1977), pp. 557–563.

[153] SG Elkomoss and G Munschy. “Electron-exciton inelastic collision cross sections for different semiconductors”. In: *Journal of Physics and Chemistry of Solids* 40.6 (1979), pp. 431–438.

[154] Wei Liu et al. “Broadening of the excitonic linewidth due to scattering of two-dimensional free carriers”. In: *Applied physics letters* 67.5 (1995), pp. 679–681.

[155] A Honold et al. “Collision broadening of two-dimensional excitons in a GaAs single quantum well”. In: *Physical Review B* 40.9 (1989), p. 6442.

[156] M Koch et al. “Enhanced energy and phase relaxation of excitons in the presence of bare electrons”. In: *Physical Review B* 51.19 (1995), p. 13887.

[157] M. Fey et al. “Phase relaxation control in heterostructures featuring charge-transfer excitons”. In: *Phys. Rev. B* 106 (16 Oct. 2022), p. 165303. DOI: 10.1103/PhysRevB.106.165303.

[158] M Stein, F Schäfer, and L Gomell. “Inelastic electron-exciton scattering in bulk germanium”. In: *Physical Review B* 99.14 (2019), p. 144310.

[159] G Ramon, A Mann, and E Cohen. “Theory of neutral and charged exciton scattering with electrons in semiconductor quantum wells”. In: *Physical Review B* 67.4 (2003), p. 045323.

[160] A Manassen et al. “Exciton and trion spectral line shape in the presence of an electron gas in GaAs/AlAs quantum wells”. In: *Physical Review B* 54.15 (1996), p. 10609.

[161] R. C. C. Leite, Jagdeep Shah, and J. P. Gordon. "Effect of Electron-Exciton Collisions on the Free-Exciton Linewidth in Epitaxial GaAs". In: *Physical Review Letters* 23.23 (Dec. 1969), pp. 1332–1335. ISSN: 0031-9007. DOI: 10.1103/PhysRevLett.23.1332.

[162] G Manzke, K Henneberger, and V May. "Many-Exciton Theory for Multiple Quantum-Well Structures". In: *physica status solidi (b)* 139.1 (1987), pp. 233–239.

[163] Kong-Thon Tsen, ed. *Ultrafast Phenomena in Semiconductors*. New York, NY: Springer New York, 2001. ISBN: 978-1-4612-6562-7. DOI: 10.1007/978-1-4613-0203-2.

[164] AA Efremov, VG Litovchenko, and AV Sarikov. "The formation of the low-dimensional porous silicon-based structures with extremely high exciton binding energy". In: *Materials Science and Engineering: C* 23.1-2 (2003), pp. 165–170.

[165] F Schäfer et al. "Optical Stark effect in type-II semiconductor heterostructures". In: *Physical Review B* 109.7 (2024), p. 075301.

[166] Alexey Chernikov et al. "Population inversion and giant bandgap renormalization in atomically thin WS2 layers". In: *Nature Photonics* 9.7 (July 2015), pp. 466–470. ISSN: 1749-4885. DOI: 10.1038/nphoton.2015.104.

[167] R. Huber et al. "How many-particle interactions develop after ultrafast excitation of an electron–hole plasma". In: *Nature* 414.6861 (Nov. 2001), pp. 286–289. ISSN: 0028-0836. DOI: 10.1038/35104522.

[168] Alexander Steinhoff et al. "Exciton-exciton interactions in van der Waals heterobilayers". In: *Physical Review X* 14.3 (2024), p. 031025.

[169] Niko S Köster et al. "Giant dynamical Stark shift in germanium quantum wells". In: *Applied Physics Letters* 98.16 (2011).

[170] A Von Lehmen et al. "Optical Stark effect on excitons in GaAs quantum wells". In: *Optics letters* 11.10 (1986), pp. 609–611.

[171] S Schmitt-Rink, DS Chemla, and H Haug. "Nonequilibrium theory of the optical Stark effect and spectral hole burning in semiconductors". In: *Physical Review B* 37.2 (1988), p. 941.

[172] Edbert Jarvis Sie. "Valley-selective optical Stark effect in monolayer WS 2". In: *Coherent Light-Matter Interactions in Monolayer Transition-Metal Dichalcogenides* (2018), pp. 37–57.

[173] Paul D Cunningham et al. "Resonant optical Stark effect in monolayer WS2". In: *Nature communications* 10.1 (2019), p. 5539.

[174] C Sieh et al. "Coulomb memory signatures in the excitonic optical Stark effect". In: *Physical review letters* 82.15 (1999), p. 3112.

[175] Yu-Hsuan Kuo et al. "Strong quantum-confined Stark effect in germanium quantum-well structures on silicon". In: *Nature* 437.7063 (2005), pp. 1334–1336.

[176] Doyeol Ahn. "Enhancement of the Stark effect in coupled quantum wells for optical switching devices". In: *IEEE journal of quantum electronics* 25.11 (1989), pp. 2260–2265.

[177] Emiliano Cancellieri et al. "Ultrafast Stark-induced polaritonic switches". In: *Physical Review Letters* 112.5 (2014), p. 053601.

[178] Adriano Barenco et al. “Conditional quantum dynamics and logic gates”. In: *Phys. Rev. Lett* 74.20 (1995), p. 4083.

[179] Daniele Nicoletti and Andrea Cavalleri. “Nonlinear light–matter interaction at terahertz frequencies”. In: *Advances in Optics and Photonics* 8.3 (2016), pp. 401–464.

[180] Markus Borsch et al. “Lightwave electronics in condensed matter”. In: *Nature Reviews Materials* 8.10 (2023), pp. 668–687.

[181] Soonwon Choi et al. “Observation of discrete time-crystalline order in a disordered dipolar many-body system”. In: *Nature* 543.7644 (2017), pp. 221–225.

[182] SR Barone, MA Narcowich, and FJ Narcowich. “Floquet theory and applications”. In: *Physical Review A* 15.3 (1977), p. 1109.

[183] YH Wang et al. “Observation of Floquet-Bloch states on the surface of a topological insulator”. In: *Science* 342.6157 (2013), pp. 453–457.

[184] CJ Fujiwara et al. “Transport in floquet-bloch bands”. In: *Physical review letters* 122.1 (2019), p. 010402.

[185] M Nuske et al. “Floquet dynamics in light-driven solids”. In: *Physical Review Research* 2.4 (2020), p. 043408.

[186] Suguru Ito et al. “Build-up and dephasing of Floquet–Bloch bands on subcycle timescales”. In: *Nature* (2023), pp. 1–6.

[187] Fahad Mahmood et al. “Selective scattering between Floquet–Bloch and Volkov states in a topological insulator”. In: *Nature Physics* 12.4 (2016), pp. 306–310.

[188] Alberto De La Torre et al. “Colloquium: Nonthermal pathways to ultrafast control in quantum materials”. In: *Reviews of Modern Physics* 93.4 (2021), p. 041002.

[189] Felix Schäfer. “Ultrafast Nonlinear Optical Response of Low-dimensional Semiconductors”. PhD thesis. Justus-Liebig-Universität Gießen, 2024.

[190] D Anders et al. “Exciton formation dynamics in (Ga, In) As quantum wells”. In: *Physical Review B* 112.23 (2025), p. 235301.

[191] D Anders et al. “Inhibited inelastic scattering of incoherent excitons for near-band edge excitations”. In: *Physical Review Letters* 132.10 (2024), p. 106901.

[192] Daniel Anders et al. “Coherent Control of Photocurrents in Germanium for Gapless and Broadband Terahertz Emission”. In: *Journal of Infrared, Millimeter, and Terahertz Waves* 46.8 (2025), p. 57.

„Ich erkläre: Ich habe die vorgelegte Dissertation selbstständig und ohne unerlaubte fremde Hilfe und nur mit den Hilfen angefertigt, die ich in der Dissertation angegeben habe. Alle Textstellen, die wörtlich oder sinngemäß aus veröffentlichten Schriften entnommen sind, und alle Angaben, die auf mündlichen Auskünften beruhen, sind als solche kenntlich gemacht. Ich stimme einer evtl. Überprüfung meiner Dissertation durch eine Antiplagiat-Software zu. Bei den von mir durchgeführten und in der Dissertation erwähnten Untersuchungen habe ich die Grundsätze guter wissenschaftlicher Praxis, wie sie in der „Satzung der Justus-Liebig-Universität Gießen zur Sicherung guter wissenschaftlicher Praxis“ niedergelegt sind, eingehalten.“

Angaben zu auf künstlicher Intelligenz (KI) basierender Hilfen wie ChatGPT oder SchulKI von OpenAI oder Gemini von Google zur Erstellung meiner Dissertation (Zutreffendes angekreuzt):

☐ Ich habe bei der Erstellung dieses Textes kein KI-Tool verwendet.

☐ Ich habe ein KI-Tool in den folgenden Bereichen eingesetzt (Mehrfachnennungen möglich):

- ☐ Ideen finden, meine Kreativität anregen
- ☐ Verstehen von Konzepten, Recherche von Fakten und Definitionen
- ☐ Optimierung eines von mir verfassten Textes
- ☐ Erstellen ganzer Textpassagen nach meinen Vorgaben

Folgende KI-Tools habe ich verwendet, damit aufgeführte Teile meines Textes von dem Tool wie folgt profitiert haben:

Datum: _____ Unterschrift: _____

Danksagung

An dieser Stelle möchte ich mich bei den Menschen bedanken, die direkt oder indirekt zum Gelingen dieser Promotion beigetragen haben.
Zuallererst gilt mein Dank Prof. Dr. Sangam Chatterjee, der mir seit meiner Bachelorarbeit die Welt der Spektroskopie gezeigt hat. Die Möglichkeit, eigene Ideen und Experimente zu verwirklichen sowie Ergebnisse auf nationalen und internationalen Konferenzen zu präsentieren, hat meine Begeisterung für die Wissenschaft aufblühen lassen. Weiterhin danke ich Prof. Dr. Andreas Knorr für die Übernahme des Zweitgutachtens. Außerdem danke ich Prof. Dr. Matthias Elm und Prof. Dr. Simone Sanna für die Mitwirkung in meiner Prüfungskommission.
Aufrichtiger Dank gilt Dr. Markus Stein, der mir die Faszination von THz nähergebracht hat. Unzählige Messnächte, Skitrips und Kartrennen lassen mich stets positiv an unsere gemeinsame Zeit zurückdenken. *You can be my THz wingman anytime.*
Außerdem möchte ich meinen derzeitigen und ehemaligen Kollegen in der AG Optik und Spektroskopie danken. Insbesondere danke ich Dr. Julian Veletas, Dr. Felix Schäfer, Lukas Gümbel, Marius Müller, Jan Littmann und Dr. Mario Zscherp. Die gemeinsame Zeit mit euch möchte ich nicht missen. Seien es unsere täglichen Rituale, unzählige Heiß- und Kaltgetränke oder gemeinsames Experimentieren im Labor —- ich denke gerne an jeden dieser Momente zurück. Außerdem danke ich Dr. Florian Dobener, der mir während meiner Bachelorarbeit die Grundlagen der Spektroskopie beigebracht hat und ohne dessen Geduld und Finesse mit LabVIEW keins meiner Mess- und Auswerteprogramme laufen würde.
Einen großen Dank möchte ich auch Anja Denhardt und Daniela Museaus aussprechen. Ihre Fähigkeiten, im bürokratischen Dschungel den Überblick zu behalten, haben viele Abläufe deutlich beschleunigt. Ihre Unterstützung ist mehr als Gold wert. Außerdem danke ich Andreas Katzer und Björn Weil, ohne deren Bereitstellung zahlreicher 100 L Heliumkannen die langen Messkampagnen nicht möglich gewesen wären. Mein größter Dank gilt abschließend meiner Familie. Ohne die bedingungslose Unterstützung meiner Eltern, die mir das Studium und die anschließende Promotion ermöglicht haben, wäre diese Arbeit wohl nie entstanden. Meiner Schwester danke ich dafür, dass sie immer wieder meine Ansichten herausgefordert hat, wenn ich mich mal wieder in einem Thema verrannt habe. Ein besonderer Dank gilt natürlich auch Jenny. Ich weiß, dass es nicht selbstverständlich ist, meine langen Abende im Labor oder auch das Weckerklingeln um 4 Uhr morgens zu tolerieren.